IMPLEMENTATION OF LOW COST, HIGH-THROUGHPUT AND HIGH SENSITIVE BIOMARKER DETECTION TECHNIQUE IN SERUM/PLASMA SAMPLES BY INTEGRATING DIELECTROPHORESIS AND FLUORESCENCE BASED PLATFORM

A Dissertation
Submitted to the Graduate Faculty
of the
North Dakota State University
of Agriculture and Applied Science

By

Velmanickam Logeeshan

In Partial Fulfillment of the Requirements
for the Degree of
DOCTOR OF PHILOSOPHY

Major Department:
Electrical and Computer Engineering

May 2019

Fargo, North Dakota

North Dakota State University
Graduate School

Title

IMPLEMENTATION OF LOW COST, HIGH-THROUGHPUT AND HIGH SENSITIVE BIOMARKER DETECTION TECHNIQUE IN SERUM/PLASMA SAMPLES BY INTEGRATING DIELECTROPHORESIS AND FLUORESCENCE BASED PLATFORM

By

Velmanickam Logeeshan

The Supervisory Committee certifies that this ***disquisition*** complies with North Dakota State University's regulations and meets the accepted standards for the degree of

DOCTOR OF PHILOSOPHY

SUPERVISORY COMMITTEE:

Dr. Dharmakeerthi Nawarathna
Chair

Dr. Ivan T. Lima

Dr. Benjamin Braaten

Dr. Glenn Dorsam

Approved:

May 08, 2019
Date

Dr. Benjamin Braaten
Department Chair

ABSTRACT

Low-cost, highly-sensitivity, and minimally invasive tests for the detection and monitoring of life-threatening cancers can reduce the worldwide disease burden. The disease diagnosis community is constantly working to improve the detection capabilities of the deadly cancers (e.g.: pancreatic and lung) at their early stages. Still there were many cancers cannot be detected at their early stages due to lack of early diagnosis techniques. One of the reason being, many cancers that occur in the body release minute amounts of biomarker molecules during the initial stages (e.g.: DNA, RNA, miRNA and antigens) in the body fluids such as blood and serum. Since the traditional bio-sensing techniques have reached their maximum capacity in terms of critical performance parameters (sensitivity, detection time, reproducibility and limit of detection) there is an urgent need for innovative approaches that can fill this gap.

To address this unmet need, here we report on developing a novel bio-sensing technique for detecting and quantifying biomolecules from the patients' plasma/serum samples at point-of-care settings. Here we have investigated the novel interactions between biomolecules and externally applied fields to effectively manipulate and specifically concentrate them at a certain detection spots near electrodes on the detection device. Then the near-field interactions between the fluorophores and the free electrons on metal surfaces were successfully integrated with the externally applied low frequency (<10MHz) electric field, to achieve maximum florescence enhancement, that produces the detection limit of target-biomolecules in the rage of femto molars (fM). Moreover, the externally applied electric potential produces dielectrophoretic and thermophoretic force on the biomolecules, together with these forces we were able to separate the fluorophore-labelled rare target-biomolecules from the others in a sample.

The novel integrated technique is tested and proved to be superior to the current gold standards (qRT-PCR and ELISA) for target-biomolecules detection in critical performance parameters. Finally the technique was used to analyze healthy and pancreatic cancer patients' samples and further it has been proved that we can differentiate the healthy individuals and cancer patients. In addition, this technique is being applied to the other diseases such as obesity, opioid addiction and other types of cancers.

ACKNOWLEDGEMENTS

At the outset, I would like to thank my advisor Dr. Dharmakeerthi Nawarathna for his constant support and excellent guidance, without whom this work would not have been possible. I am also grateful for the exemplary mentorship that he has provided. He has a very positive influence on my life and career. My deep appreciation is extended to my co-adviser Dr. Ivan T. Lima for his valuable inputs and encouragement throughout my PhD studies. I would also like to acknowledge my committee member Dr. Glenn Dorsam for taking time to guide and provide me enough support in the experiments related to biology. I profusely thank my committee member Dr. Benjamin Braaten for being integral parts of my committee and providing me with valuable suggestions, support, guidance, and good will.

I am proud to acknowledge NDSU Graduate School Doctoral Dissertation Fellowship for providing financial support to carry out my research.

I would also like to thank the Department of Electrical and Computer Engineering for providing me with a platform to showcase my skills and also for providing financial support, Laura D. Dallmann for taking care of all the little things and all the paper work, and all my friends and fellow graduate students who made my journey with lots of pleasant memories.

I would like to extend my thanks to Jeffrey Erickson for his continuous technical support and ideas that he provided throughout my PhD studies. I would also like to acknowledge Gregory Strommen for fabricating the micro electrodes for my PhD studies.

My special appreciations go out to my mother, father, brother and family members for their love and unconditional support. Last but not least, I would like to thank the Almighty Lord for providing me with the physical and mental strength to emerge successful despite all odds.

TABLE OF CONTENTS

LIST OF TABLES

LIST OF FIGURES

CHAPTER 1. INTRODUCTION

According to the world health organization, there were about 1.9 million new cancer cases and 0.63 million cancer related deaths are projected to occur in the United States in 2020 [1]–[3]. Early stage cancers can be treated with traditional treatment methods and attain the remission for prolong period [4],[5]. One way to detect the cancer in early stage is detecting the circulating cancer related biomarkers from the whole blood, saliva and serum [4],[6]. These quantified cancer related biomarkers can be used to improve the understanding of the cancer type, stage of the cancer and develop new therapeutic strategies for control or cure the disease [4],[6]. Therefore, accurate quantification of cancer related biomarkers in body fluids provide a reliable way to diagnosis of cancers [4],[7].

The term biomarker generally refers to a broad subcategory of measurable pointers of some biological condition, pharmacological responses or pathogenic process [7]–[9]. Medical signs stand in contrast to medical symptoms, which are limited to those indications of health or illness perceived by patients themselves. There are several more precise definitions of biomarkers in the literature, and they fortunately overlap considerably[7],[10]. In 1998, the National Institutes of Health Biomarkers Definitions Working Group defined a biomarker as "a characteristic that is objectively measured and evaluated as an indicator of normal biological processes, pathogenic processes, or pharmacologic responses to a therapeutic intervention." World Health Organization (WHO) and the United Nations and the International Labor organization, defined the term biomarker as "any substance, structure, or process that can be measured in the body or its products and influence or predict the incidence of outcome or disease" [7]. An even broader definition takes into account not just incidence and outcome of disease, but also the effects of treatments, interventions, and even unintended environmental

exposure, such as to chemicals or nutrients. In their report on the validity of biomarkers in environment risk assessment, the WHO has stated that a true definition of biomarkers includes "almost any measurement reflecting an interaction between a biological system and a potential hazard, which may be chemical, physical, or biological. The measured response may be functional and physiological, biochemical at the cellular level, or a molecular interaction." [7]. Biomarkers have been approved by the U.S Food and Drug Administration (FDA) regulation for use as diagnosis tool for the cancers [7],[9]. Among biomarker categories, proteins, DNAs, RNAs and miRNAs are included in one of the most important group of biomarkers, which usually containing in blood, saliva, serum or tissue, and can be used as an effective pointer of the disease states [7]–[10]. The development of reliable, high throughput, cost effective, powerful detection and monitoring strategies for cancer is particularly important, due to the disease's prevalence, high rates of recurrence, and potential lethality.

1.1. Current state of the art and challenges

1.1.1. Protein biomarker detection techniques

Currently, there are many methods of protein biomarker detection have been invented such as Enzyme-Linked Immunosorbent Assay (ELISA) and Surface Plasmon Resonance Arrays (SPR). In many of the methods immunoassays are utilized to detect/quantify target biomarkers such as proteins, antigens and antibodies in biological samples [11],[12]. Typically, in immunoassays, first, target specific antibody is attached onto a solid surface of a device or a traditional well-plate. Second, the biological sample containing the target molecules (analytes) is pipetted on to/flow over antibodies allowing to conjugate with antibodies. Finally, the presence of antibody-analyte complexes are detected and quantify the levels of target analytes in the sample [12],[13]. For an example, during the diagnosis of tumors or monitoring the progress of

on-going treatments for tumors, it is required to monitor the levels of representative tumor markers (proteins) in patients' blood [14],[15]. This is typically performed through immunoassays and current gold standard for detecting/quantifying target analytes from blood samples is the ELISA. The ELISA uses antibody-analyte conjugation followed by quantification of antibody-analyte complexes in the sample [15]. The commonly use method for quantifying antibody-analyte complexes involves to measure the concentration (analyte) dependent color change or fluorescence intensity change in the sample. The detection limit of ELISA is about 250 pg/mL [16]. However, to detect/quantify analytes (proteins) that are related to various stages of tumors including early detection require to detect well below the current limit of the ELISA. For example, Interleukin 6 (IL-6) levels of early oral cancer patients have <100 pg/ml and prostate specific antigen (PSA) level of the early stage of prostate cancer patients is about 1ng/mL [17]. Further, it has been reported that there are << pg/mL analytes in the early stage of tumors [17]. Therefore, depending on the tumor type and the stage of the tumors, it is required to quantify various levels of analytes ranging from (ng/mL) - (pg/mL) [16],[17]. Furthermore, typically, it requires to detect/quantify levels of number of protein targets (typically 4-6 protein targets) in single-experiment [18]. To accommodate these critical needs in the current diagnosis, there is a need to for a technique that has a large dynamic range with an ability to detect extremely low levels of target analytes (<pg/mL).

To address this critical need in biology/medicine, there are number of new techniques have been proposed and utilized [19]. Among the new techniques, the impedimetric based analyte detection/quantification offers low cost and label-free technique [18],[20]–[22]. It uses an array of microelectrodes called interdigitated electrodes that are fabricated on glass or similar materials [23]–[25]. In impedimetric experiments, the change of impedance upon binding the

target analytes on to antibodies that are immobilized on the electrodes or between electrodes is measured at low frequencies (<1000 Hz). Using a standard curve of known analyte concentration vs. change in impedance, the unknown analyte concentrations are calculated [24]. It has been reported that the lowest analyte concentration that can detect/quantify using this technique is about 80 pg/mL [18]. However, impedimetric based analyte detection/quantification suffers number of limitations such as impedance is dependent on the conductivity of the biological sample, there is a need for an expensive electric circuits and equipment (impedance analyzers) to record the impedance and impedance vary from analyte type to analyte type. In addition to impedimetric based detection/quantification, there are number of other techniques such as ion sensitive field-effect transistors, semiconducting carbon nano-tubes, thin-film gate transistors and electrolyte-insulator-semiconductor structures are available to detect/quantify target analytes of a sample [18],[26]. However, almost all of these techniques require target analytes in very low ionic buffer solutions. Therefore, these techniques have been using in applications such as detecting DNA molecules and DNA hybridization events in low conductivity buffers. Furthermore, it has also been reported that successful development of these techniques for DNA analysis is much complex than expected. In particular, theoretical basis of the observed results including wide variety of reported signal amplitudes and response times, still remains unclear [26]. Therefore, these techniques have very limited applicability in immunoassays.

1.1.2. Nucleic acid biomarker detection techniques

Currently many miRNA, DNA, mRNA detection methods have been used in the disease diagnosis field, mostly almost all relying on hybridization of the target nucleic acid molecules with the complimentary DNA capture molecules. This hybridization is completed through an interaction of complementary nucleotides between a target miRNA and a complementary strand

of nucleic acid to produce a double-stranded helical molecule [27]. Once hybridization occurs, there must be a way to translate the hybridization event into a measurable signal. These signals can be detected in various ways, such as electrochemically and measuring fluorescence and bioluminescence intensities [27],[28].

Among all the mRNA nucleotide biomarker detection methods the most standardized and widely used method to detect mRNA nucleic acid molecules is northern blotting [29]. In this method, the sample containing mRNA nucleic acid molecules is run on an electrophoresis gel, then the nucleotide is transferred to a nitrocellulose membrane, followed by soaking in a solution containing a fluorescent or radiolabeled oligonucleotide probe which is complementary to the target nucleotide for hybridization to occur. This method is very time-consuming (more than 24 hours) and it have very low throughput [29],[30].

The popular miRNA/DNA nucleic acid molecules detection method in the diagnosis field is quantitative real time polymerase chain reaction (qRT-PCR), which can detect target nucleic acid molecules in real time [29],[31],[32]. In this method, nucleotide that present in the sample is modified, for example, with a polyadenylated tail. A primer is then added which anneals to the nucleotide target and results in cDNA via reverse transcription. Once the cDNA has been synthesized, two primers are added which anneal to the cDNA and produce multiple copies of the cDNA. The forward primer is nucleotide -specific, while the reverse primer is not. For real time monitoring to occur a fluorescent intercalator added to that sample, which intercalates double-stranded DNA. Then the increase in fluorescence observed and analyzed for the detection of target miRNAs/DNAs. In this method requires stable genes to serve as a reference. Specifically during target miRNA detection, finding stable genes to use as references is technically difficult. Further, qRT-PCR reactions are expensive (> $2000), time consuming (>7

hrs) and also this method is not capable of detecting low concentration nucleic acid molecules (<pM), thus it is also not suitable for routine testing [29],[33],[34].

There are some other techniques, including microarrays and electrochemical and hybridization-based sensors, but they are fundamentally incapable of detecting rare nucleic acid molecules (<pM) from a complex mixture of nucleic acid molecules [29],[35],[36]. In microarray hybridization-based sensors the capture probes were placed at the bottom of a microfluidic channel in an array and the sample solution was pumped in to the microfluidics channel for hybridization with entire length of its target nucleotide as well as with that of the signaling probe. To increase the diffusion the molecules a convection flow of sample solution was introduced over the microarray, with the use of an integrated microfluidic platform, entailed expedited hybridization. Finally, the detection was performed through observing the fluorescence signal [29],[33].

In electrochemical hybridization based sensors, first nucleotide molecules were directly conjugated to electrocatalytic moieties such as OsO2 nanoparticles or Ru (PD)2Cl2 (PD is 1,10-phenanthroline-5,6-dione) [29],[33],[37],[38] .DNA probes which are complementary to the target nucleic acid molecules are immobilized onto a solid support, and the target nucleotide is allowed to hybridize with the immobilized probe. After wash steps, the labeled target nucleotide is detected through measuring an increase in current. This increase in current can be correlated to the amount of nucleotide target that is present in the sample [29],[38].

Fundamentally, nearly all-current detection methods rely on non-specific, time-dependent, and unsteady molecular diffusion for critical target-probe hybridization, causing significant variation in results [39]–[41]. Additionally, molecular crowding near detection electrodes or substrates produces steric hindrance [39]. These issues affect the sensitivity, limit

of detection, and speed of detection, especially, in the detection of minute amounts (< 1%) of target nucleotide biomarkers from a larger background [39]. To minimize molecular crowding, a significant dilution of serum is needed. However, a diluted serum sample (from μLs serum) is insufficient to identify target biomarkers that are clinically important [39]–[45]. To address this issues in the current detection methods, I have utilized Dielectrophoretic (DEP) force and fluorescence based platforms to develop a potential biomarker detection technique.

1.2. Dielectrophoretic spectroscopy for biomarker manipulation

The term dielectrophoresis (DEP) was first used by Phol in 1951, derived from the Greek word "phorein", an effect where a particle is carried as a result of its dielectric properties [46]. First, Phol defined this effect as " the motion of suspensoid particles relative to that of the solvent resulting from polarization forces produced by an inhomogeneous electric field" [46] [47]. Any electrical insulator materials, which can be polarizable when its subject to an exterior electric field is known as dielectric materials [48]. When a dielectric material is placed in an applied exterior electric field, electric charges do not pass through them due to the electrical insulator characteristic; only the electric charges deviate slightly from their average equilibrium positions, which cause a dielectric polarization in the dielectric materials [47],[49],[50]. Due to the polarization of the dielectric material, electric dipoles are produced in the dielectric materials [51],[52].

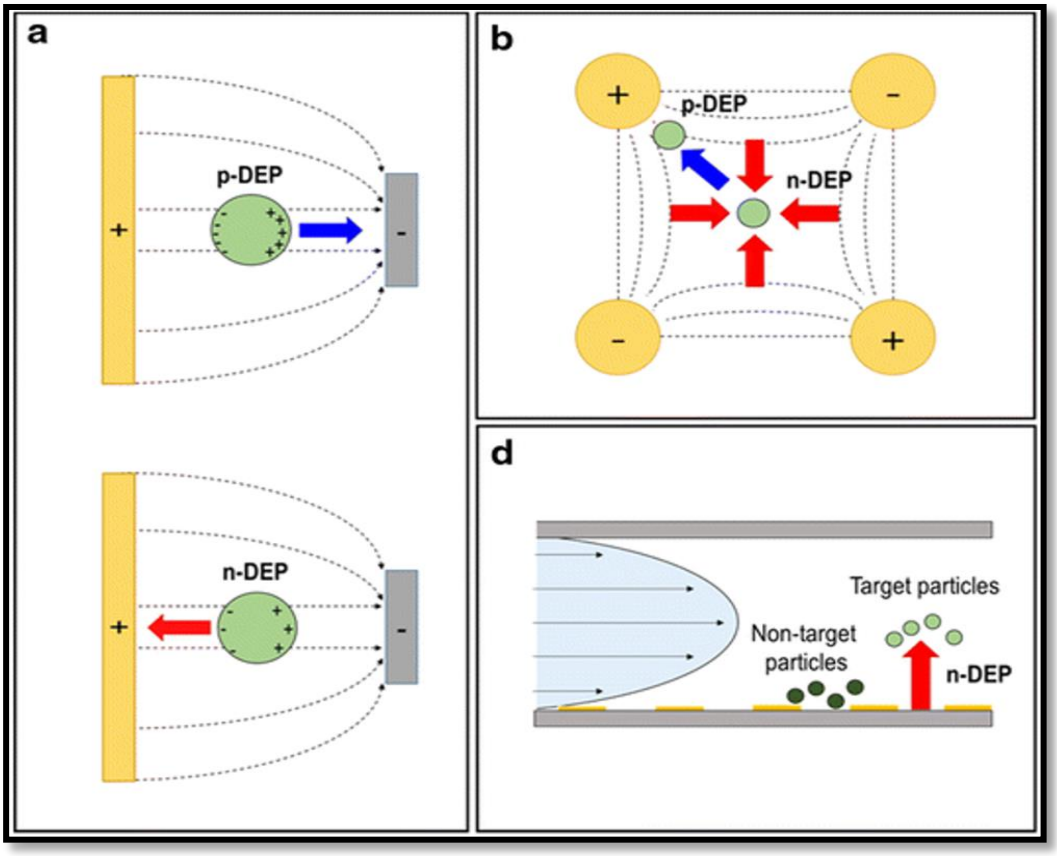

Figure. 1.1: **Methods of utilizing DEP force on biomedical engineering assays**. **(a)** Traditional DEP can be used to concentrate particles near electrodes using positive or negative DEP, **(b)** another electrode configuration to concentrate particles either on electrodes, or away from electrodes, **(d)** integration of DEP with viscous drag force for continuous separation of particles. This figure was adopted from ref [53] with permission.

The time-average magnitude of the DEP force on a spherical isentropic homogeneous dielectric particle located in a non-uniform electric field region can be represented by the equation (1.1).

$$F_{DEP} = \frac{1}{2}\alpha \nabla |E|^2 \qquad (1.1)$$

where α is the polarizability of the dielectric particle, ∇ is the vector operator, and E is the r.m.s value of the electric field. The α or polarizability of the suspended dielectric particle depends on the frequency and field dependent dielectric properties of particle and the suspended medium [47],[50],[62]–[64],[54]–[61]. The DEP force can be attractive or repellent from electrodes

based on the value of α. The attractive DEP (positive DEP) produced when α is positive and the DEP force move the dielectric particle towards electrode edges or to the higher electric field gradient region or to the region that has maximum value for $\nabla|E|^2$; similarly, repellent DEP (negative DEP) is produced when α is negative and DEP force move the particle in the opposite direction of the higher electric field gradient and to the weak electric field gradient (Figure. 1.1).[61],[63]–[68].

The polarizability of the spherical particle can be derived as:

$$\alpha = 4\pi r^3 \varepsilon_m Re[f_{CM}(\omega)] \tag{1.2}$$

where is the radius of the spherical dielectric particle, ε_m is the permittivity of the suspending medium, ω is the radial frequency of the applied electric field, and $\boldsymbol{Re}\{f_{CM}(\omega)\}$ is the real part of the Clausius-Mossotti factor (CM) and for the spherical particle, is defined as:

$$f_{CM}(\omega) = \frac{\varepsilon_p^* - \varepsilon_m^*}{\varepsilon_p^* + 2\varepsilon_m^*} \tag{1.3}$$

where ε_p^* is the complex permittivity of the dielectric particle and ε_m^* is the complex permittivity of the suspending medium. The complex permittivity is given by $\varepsilon^* = \varepsilon - j(\frac{\sigma}{\omega})$ with σ the real conductivity, ε the real permittivity, and $j = \sqrt{-1}$ and ω the angular frequencies [46],[47],[70]–[77],[56]–[62],[69].

Variations in the CM factor alter the value of α and subsequently vary the DEP force. For example, for a sphere, the real part of the CM factor is theoretically bounded between -1/2 and 1. Moreover, we can re-define positive DEP and negative DEP. Positive DEP occurs when $Re[f_{CM}(\omega)] > 0$ and negative DEP occurs when $Re[f_{CM}(\omega)] < 0$. If $Re[f_{CM}(\omega)]$ becomes zero under certain conditions, the DEP force act on the polarized particles also becomes zero [69]–[75]. The frequency at which zero DEP force occurs is called crossover frequency (f_{CO}), which is defined as:

$$f_{CO} = \frac{1}{2\pi\varepsilon_0}\sqrt{\frac{(\sigma_m-\sigma_p)(\sigma_p+2\sigma_m)}{(\varepsilon_p-\varepsilon_m)(\varepsilon_p+2\varepsilon_m)}} \quad (1.4)$$

where σ is the real conductivity and ε is the real permittivity, and sub-index *p*, *m* are the particle and medium respectively [47],[69],[70],[78]. It has been demonstrated that f_{co} depends on the conductivity (σ_p) of the particle at low frequencies (< 1MHz) [79]. The conductivity (σ_p) of the homogeneous dielectric spherical particle can be written as the sum of bulk conductivity (σ_{pbulk}) and surface conductance (K_S), which can be represented as:

$$\sigma_p = \sigma_{pbulk} + \frac{2K_S}{r} \quad (1.5)$$

where r is the radius of the spherical particle. Depending on the material of the particle, such as polystyrene and silica, the bulk conductivity (σ_{pbulk}) can be negligible. Therefore, surface conductance (K_S) provide a dominating contribution to the conductivity of the particle [47],[69],[70],[75],[78].

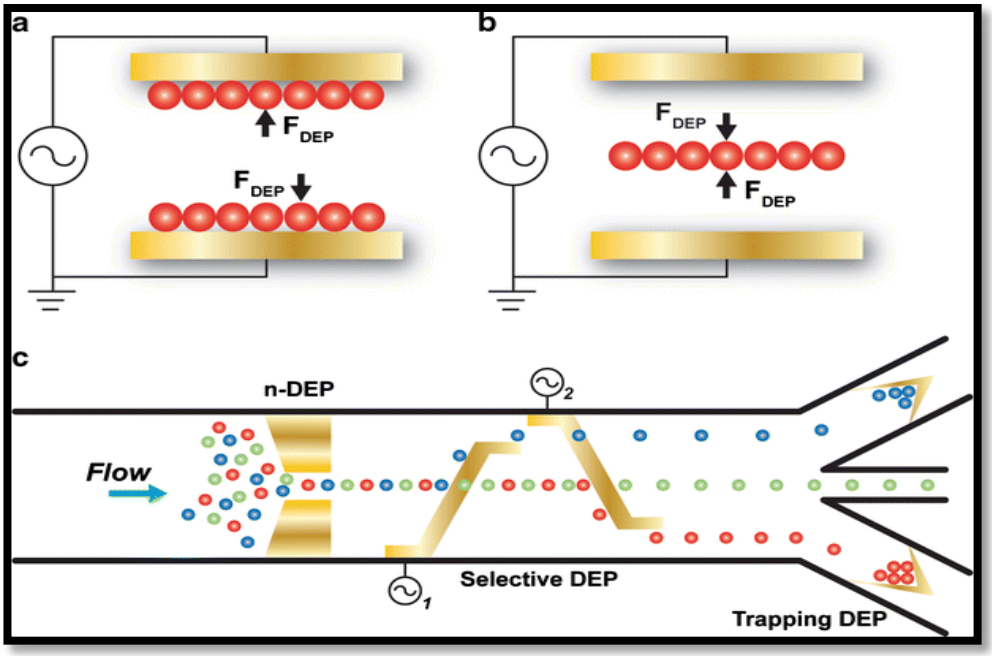

Figure. 1.2: DEP particle separation. DEP separation can be **(a)** positive (pDEP) or **(b)** negative (nDEP) which affects where cells are positioned within a field. **(c)** DEP has been utilized in microfluidic systems in a variety of arrangements, some of which are depicted here. This figure was adopted from ref [80] with permission.

DEP has been used in sensing, trapping, transporting, and sorting different type of dielectric particles (Figure 1.2) [47],[81]. Since the biological samples, such as cells, proteins, DNAs, RNAs, and miRNAs have dielectric properties, it was widely used in medical applications. The earliest dielectrophoretic studies were largely conducted with the aim of understanding how cells produce DEP forces, and how to use DEP and dielectric properties of cells to better understanding their physicochemical properties [47],[66],[81],[82]. Currently, DEP has made it possible to achieve: separation of cancer cells from healthy cells [47],[81],[83]; separation dead cells from live cells [84],[85]; high speed cell sorting [81],[82]; cell patterning [66],[81],[86],[87]; and electroporation [47],[64],[81].

Positive and negative dielectrophoretic phenomenon utilized in the separation of cells or particles. A selected frequency of the signal will be applied to the particle sorting device, where the target particles will feel the positive DEP and become trapped at the electrodes; at the same

time nontarget particles experience negative DEP (or repulsive DEP from electrodes) or zero DEP force, and flow out without trapping (Figure 1.2). Finally, the trapped target particles were released from the electrodes by switching off the field and collected separately. In addition, there are other methods that combine DEP trapping with viscous drag force used to separate materials continuous fashion [68],[69],[81],[82]. In addition to cells, biomarker molecules (such as DNAs, proteins, and RNAs) were trapped on the electrodes using DEP force for calculation of expression levels or molarities [57],[88] [89]. In addition, high-speed hybridization of DNAs and RNAs was also successfully conducted using the DEP force, and this might drastically improve the biological assay time [90],[91]; these developments collectively advanced the biosensing techniques involved in the detection of rare biomarkers in biological, environmental, and other samples [47],[89].

In addition to cellular studies, studies have also focused on using DEP in biomarker sensing applications [92]. With the introduction of DEP in biosensing, critical sensing parameters such as sensitivity, specificity, and detection limit have significantly improved [89],[93]. For example, the miRNA molecules, which are short in size (~8 nm) and represent a biomarker for early-stage cancers, have been successfully detected using DEP and proved to be superior to the other current detection techniques available in the medical industry [89].

In addition to the medical applications, DEP has also been widely used in other industrial applications, such as separating minerals [94]–[96], self-recovering current limiting fuse [97], depositing a patterned coating of a nanostructure material onto a substrate [47],[98], collecting of micron-scale particles (granular, threadlike, sheets, or microelectronic parts) [47][99], polishing local areas of 3D surfaces using abrasive powders [47],[100], biodegradation of organic pollutants in soil [47],[101], and in water treatments systems [47],[102]. During the separating of

minerals, DEP is applied at different frequencies and, based on the frequencies, the polarizability of the mineral partials changes. Because of these polarizability changes, the minerals are separated from each other due to the DEP force [94],[95],[103]. In self-recovering current limiting fuse, the current-limiting operation was attained by frequently switching between a conducting position, collection of conductive particles between two electrodes brought by DEP, and evaporation or spreading state of the conductive particles due to Brownian motion or diffusion [47].

In the process of coating a nanostructure material onto a substrate, an AC potential applied between two electrodes for a time limit period. The applied AC potential create a DEP force on the nanostructure materials suspended in the solution. Due to the DEP force the nanostructure materials move and attach them to the electrodes [47],[97]. The polishing of 3D surfaces was achieved by abrasive powders, such as Al_2O_3, diamond or SiC, dispersed in silicone oil and agitated by DEP forces similar to the coating process [46],[99]. In the water treatment systems, the live bacteria and microbes in water were selectively concentrated and separated by the nature of the polarizability of the particle due to the DEP force in different frequencies [46],[101].Advances in the use of DEP for manipulation of nanoparticles are also opening up new applications, including the fabrication of a new generation of electronic devices and sensors [47].

In addition to the traditional metal electrode based DEP studies, the electrode-less DEP has also been developed and used in multiple studies [57],[103]–[105]. The electrode-less DEP could be produced in the molecules that are suspended in the physiological buffers, such as blood, serum, and urine [57],[105]; it could further simplify the assays.

1.3. Fluorescence spectroscopy for biomarker sensing

Fluorescence spectroscopy which is also known as fluorometry or spectrofluorometry, is a category of electromagnetic spectroscopy that examines the fluorescence from a sample[106],[107]. Fluorescence spectroscopy is a popular research tool which commonly used in biochemistry, molecular biology, and biomedical applications for medical diagnosis, DNA sequencing, single bio-molecule sensing, mineralogy, and genomics[107],[108]. Up to the present, all fluorescence findings, including spectral offsets, quantum yields, lifetimes, fluorescence quenching and anisotropies, have all been utilized in fundamental and applied uses of fluorescence[106].

Fluorescence molecules have different states called energy levels. Fluorescence spectroscopy principally concerns electronic and vibratory states of the fluorescence molecules. In general, the fluorescence species inspected have a basic electronic state which is known as a low energy state, and an excited electronic state which is also known as higher energy state. In each of these electronic states, there are different vibratory states [106]–[108]. In fluorescence, the molecules is first excited through a desired light wave, from the light wave by absorbing a photon, the molecule will transfer from its ground electronic state to one of the different vibratory states in the excited electronic state. Collisions with other molecules cause the vibratory energy loss of the excited molecule until it reaches the lowest vibratory state of the excited electronic state. Due to the energy loss, the exited molecule fall downward to one of the different lower vibration levels of the ground electronic state, by emitting a photon during the process. The emitted photons will have different energies and different frequencies. Therefore, the emitted photon will have different color and different intensities for different fluorescence molecules [106]–[108].

The fluorescence excitation and emission can be simply demonstrated by the below equation

$$\text{Excitation: } S_0 + hv_{ex} \rightarrow S_1 \tag{1.6}$$

$$\text{Emission: } S_1 \rightarrow S_0 + hv_{em} + heat \tag{1.7}$$

where $h = \text{Planck}'\text{sconstant}$ (6.626 x 10^{-34} J) and $v = \text{frequency}$ of the light, hv represents the photon energy. S_0, S_1 represents the ground state and the electronic excited state of the fluorescent molecule respectively [106],[107]. A molecule at the electronic excited state (S_1) can be relaxed by different rival pathways. It can undertake non-radiative relaxation where the excitation energy is debauched as heat (vibrations) to the solvent where the fluorescence molecule suspended. The excited organic molecules can also relax by transform to a triplet state, which can then relax by phosphorescence, or by a non-radiative secondary relaxation step. Relaxation from S_1 can also happen through interaction with a second molecule through fluorescence quenching, near-field dipole-dipole interaction (resonance energy transfer), internal conversion and intersystem crossing [106],[107]. In most of the cases the emitted light form the fluorophore has a longer wavelength (λ) compared to excited light, therefore according to the speed (c) equation of light $c = f.\lambda$ the frequency (f) will be reduced. Therefore the energy of the photon ($E = h.f$)will also reduced. This wave energy and the frequency reduction is known as Stokes shift [107]. However, when the electromagnetic radiation absorbed is intense, it is possible for an electron to absorb two photons at the same time; this two-photon absorption can result in the emission of shorter wavelength radiation than the excited light wave length [106],[107]. There are some possibilities that the emitted light wave length is equal to the excited light wavelength, which is called "resonance fluorescence" [107].

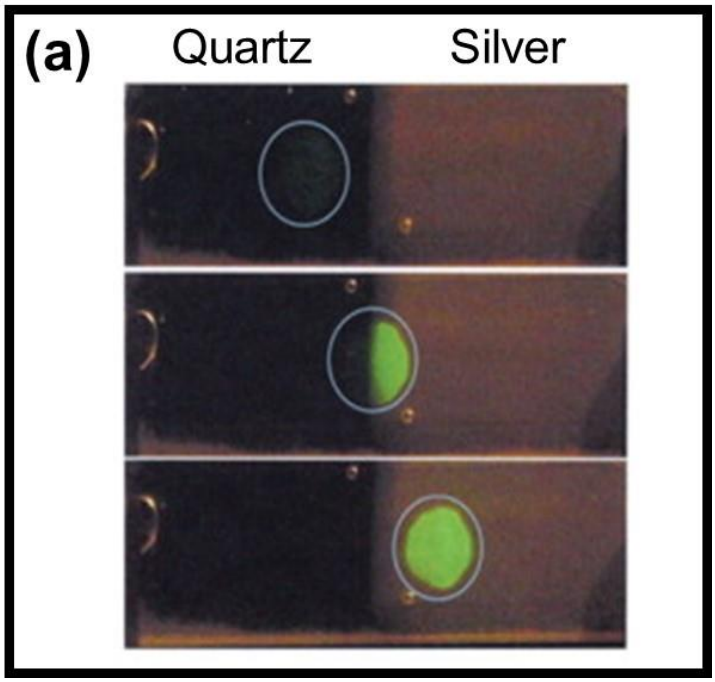

Figure. 1.3: Fluorescence enhancement from silver nanostructures. (a) Photographs of fluorescein-labeled human serum albumin (molar ratio of fluorescein/ human serum albumin = 7) on quartz and on Silver fractal-like structures. Fluoroscence was observed with 430 nm excitation and 480 nm long-pass filter. The excitation was progressively moved from the quartz side to the silver side. This figure was extracted from ref [109] and [110] with permission.

The inclusion of fluorescence as a part of biosensing has led to tremendous growth in both biosensing and fundamental fluorescence studies. As a result, optical based bio-sensors have paved the path toward the advancement of highly sensitive, strong, and facile detection of target biomarkers [111],[112]. To use fluorescence in the detection, labeling of target molecules with fluorophore tags is needed, and then fluorescence intensity is measured. Later, the fluorescence intensity is converted to molarity values [111],[113]–[115]. In sensing applications of biomolecules, there are three fundamental parameters used to determine the applicability of the sensing method to a specific application. These are sensitivity, specificity, and limit of detection [116]. Although sensitivity and specificity of fluorescence-based detection are very high, the limit of detection could be further improved to be applicable in many medical applications[117]. For example, studies have reported that the current detection limit of

fluorescence-based detection is not sufficient to detect many disease-related biomarkers, particularly for detecting early-stage disease development [17],[93],[118].

To further improve the detection limit of the fluorescence-based assays, near-field metal-fluorophore interactions could be used (Figure 1.3). For example many studies including Fu et al. [119], White et al., [120], Choudhury et al. [121], and others have used near-field metal-fluorophore interactions to enhance the fluorescence intensity. Moreover, studies have reported that metal (e.g., silver and gold) could alter the characteristic features of properties of fluorophore molecules; these changes have led to increased fluorescence intensity and stability of fluorophore molecules. We will briefly discuss some of these properties below.

$$\emptyset = \frac{Number\ of\ photons\ emitted}{Number\ of\ photons\ absorbed} \tag{1.8}$$

The quantum yield of a fluorophore ($\emptyset$) is an important parameter in fluorescence measurements, which gives the efficiency of the fluorescence process [122]–[124]. This can then be simply expressed as the ratio between the numbers of photons emitted to the numbers of photons absorbed (equation 1.8). The highest quantum yield of a fluorophore is 1 (100%) when the photon absorbed is equal to the photon emitted [122]–[124].

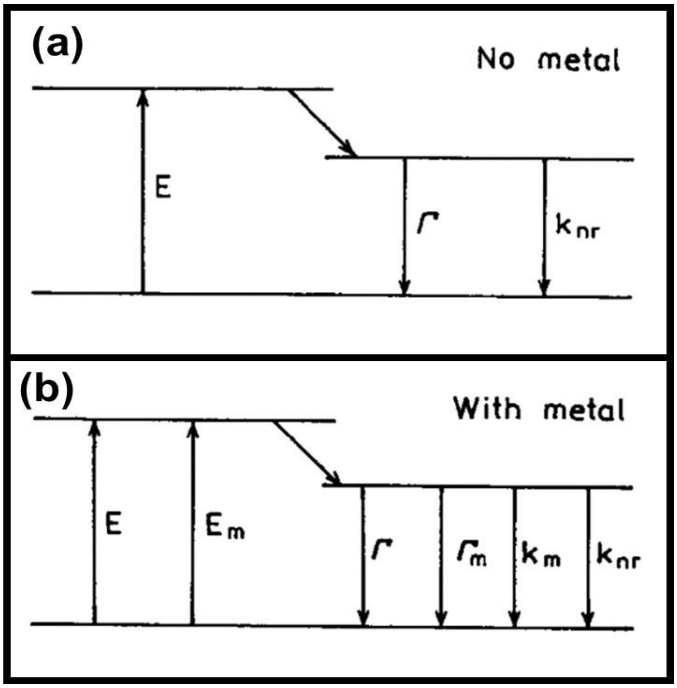

Figure. 1.4: Jablonski diagram, without **(a)** and with **(b)** the effects of a nearby metal surface. For metal-fluorophore distances over 5 nm, the effect of quenching by the metal (k_m) is expected to be minimal. This figure was adopted from ref [122] with permission.

The quantum yield can be demonstrated through the Jablonski diagram (Figure 1.4). Moreover, the quantum yield and lifetime of a fluorophore are dominated by the magnitudes of the radiative rate (Γ) and the sum of the non-radiative decay rate (k_{nr}) [122],[123]. The quantum yield ($\emptyset_0$) of the fluorophore in the absence of quenching can be represented as:

$$\emptyset_0 = \frac{\Gamma}{\Gamma + k_{nr}} \tag{1.9}$$

The natural lifetime of a fluorophore (τ_n) is the inverse of the radiative decay rate ($\tau_n = \Gamma^{-1}$) where there in no nonradiative decay occur ($k_{nr} = 0$). Fluorophores with high radiative rates have high quantum yields and short lifetimes [122],[124]–[126]. The radiative decay rate is essentially constant for any given fluorophore. Hence, the quantum yield can only be increased by decreasing the nonradiative rate k_{nr}. In a fluorescence system if the nonradiative decay rate presents the life time of the fluorophore can be modified as $\tau_0 = (\Gamma + k_{nr})^{-1}$. The

lifetime of a fluorophore can be increased or decreased by changing the value of k_{nr}. In other words the quantum yield and the life time increase or decrease together when the nonradiative rate presents in the fluorescence system. By modifying the nonradiative decay rate we can manipulate the quantum yield and the life time of a fluorophore [122],[124]–[126]. The same equation can be derived in a different way when a presence of a metal surface or metal nano structure in the fluorescence system, as below

$$\emptyset_m = \frac{\Gamma+\Gamma_m}{\Gamma+\Gamma_m+k_{nr}} \tag{1.10}$$

Where Γ_m represents the radiative decay rate increase due to the presence of metal nano structures or metal thin films. Then, the lifetime of the fluorophore is ($\tau_n = (\Gamma+\Gamma_m + k_{nr})^{-1}$) [122]–[124]. Therefore, presence of metal could increase the quantum yield and decrease the lifetime of the fluorophore; both of these effects will make the fluorophores very bright and stable. At fundamental level, increasing the radiative decay rate of fluorophore molecules is highly dependent on the ability to orient the fluorophore dipole with the plasmonic axis of the hotspots and subsequently place the fluorophore molecules in the area with the highest density of surface plasmon. For example, this effect is maximum when the fluorophore molecule is perpendicular to the surface of an ellipsoidal nano-structures that has $\frac{a}{b}$ ratio equal to 1.75; the radiative decay rate of the fluorophore could be increased by a factor of 1000-fold or greater [122],[124].

The presence of metal could alter the apparent quantum yield (Y) of the fluorophore molecules, which is defined as the intensity of the fluorophore relative to the control sample (without metal surface) measured with the same intensity of excited light. Mathematically, Y can be represented as

$$Y = \left|L_{(\omega_{ex})}\right|^2 Z_{(\omega_{em})} \tag{1.11}$$

where $L_{(\omega_{ex})}$ is the product of the fluorophore quantum yield without metal, and the amplification of the incident field $(\frac{E}{E_0})$ by the metal; $Z_{(\omega_{em})}$ represent the partition of energy into the radiative and non-radiative decay pathways, as modified by the metal particles (Figure 1.5) [122]. The electric field enhancement could be due to the light scattering near nano-scale structures. In addition, since the fluorescence intensity depends on the square of the electric field enhancement$(\frac{E}{E_0})$, metal structures can significantly enhance the intensity of the fluorophore relative to the control sample.

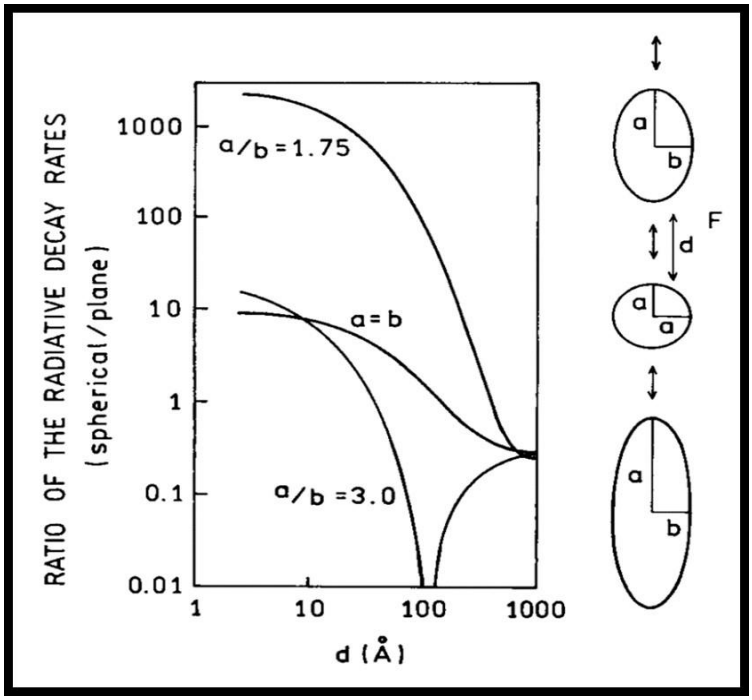

Figure. 1.5: The effects metallic nano-structures on the radiative decay rate of a fluorophore. The volume of each spheroid is equal to a sphere with 40 nm diameter. This figure was adopted from ref [122] with permission.

Studies have reported that the electric field enhancement due to the metal surfaces can be as high as 140 [122]. To achieve large enhancement of fluorescence intensity, the fluorophore should be placed 5–20 nm from the metal surfaces or nano-structures [122]–[124].

As stated above, the presence of metal can have detrimental effects, such as fluorescence quenching on fluorophores. Quenching refers to any process that results in a decrease in the fluorescence emission intensity [122],[127]–[129]. During the quenching process, the fluorophore returns to the ground state, without emitting energy or a photon. The quantum yield ($\emptyset_0$) of a fluorophore with quenching can be represented as:

$$\emptyset_0 = \frac{\Gamma}{\Gamma + k_{nr} + k_q[Q_u]} \tag{1.12}$$

$k_q[Q_u]$ represents the quenching rate [117],[122]. The quantum yield of a fluorophore in the presence of a metal surface ($\emptyset_m$) can be represented as

$$\emptyset_m = \frac{\Gamma + \Gamma_m}{\Gamma + \Gamma_m + k_{nr} + k_m} \tag{1.13}$$

where the k_m refers to the quenching effect by the metal surface. Because of the quenching effect, the lifetime of a fluorophore can be defined as ($\tau_n = [\Gamma + \Gamma_m + k_{nr} + k_m]^{-1}$) [122],[123]. The quenching effect could decrease both quantum yield and the lifetime of a fluorophore. As a result, quenching will significantly decrease the fluorescence intensity. One way to minimize the quenching is to increase the metal-fluorophore distance [122]–[124],[130].

As we discussed above, the fundamental level mechanisms responsible for the fluorescence enhancement are:

(a) Decreasing fluorophore quenching by reducing the energy transfer from fluorophore molecules to the metal or increase the metal-fluorophore distance,

(b) Increasing the radiative decay rate of fluorophore molecules by aligning the fluorophore dipole with the plasmonic axis and placing the fluorophores in the high surface plasmonic region, and

(c) Concentrating the fluorophore molecules in an area where a local electric field is produced from light scattered by plasmonic structures [110],[122],[126].

Under optimized conditions, mechanism (b) contributes about 10^5 times (maximum), and mechanism (c) contributes about 10^4 times (maximum) to the fluorescence enhancement [110],[122],[126]. Therefore, if mechanisms (a), (b) and (c) are integrated, a maximum of one billion-fold fluorescence enhancement is possible to achieve. Billion-fold enhancement will easily produce the detection of few fluorophore molecules.

CHAPTER 2. UTILIZATION OF CROSS-OVER FREQUENCY PHENOMENON OF DIELECTROPHORESIS TO QUANTIFY RARE TARGET BIOMARKERS FROM BIOLOGICAL SAMPLE

2.1. Introduction

Due to the limitations in the current biomarker detection techniques (discussed in chapter 1) the detection of extremely low level (aM-fM) of target biomarkers are impossible. To address this gap here we report on a new label-free, high-throughput technique that is capable of detecting/quantifying target analytes down to few thousands of molecules (~zmoles). Furthermore, presented technique can be integrated with microfluidics chips for developing point-of-care diagnosis. This technique utilizes the interaction between antibody-analyte complexes with externally applied electric fields. Moreover, it uses the frequency dependent DEP to detect and quantify analytes.

According to the DEP theory at higher frequencies (>1MHz), *fco* depends on the permittivity the particle (ε_p) (equation 1.4) [64]. From the equation (1.5) from the DEP theory, it can be proved, at low frequencies, cross-over frequency is dependent on the surface conductance. We have utilized crossover frequency as our method of detection/quantification of various levels of target analytes in biological samples. Moreover, we have utilized the polystyrene beads with modified the surfaces with antibodies that are selectively conjugating with target analytes. We

---

This chapter was extracted from a published article in Physical Review E (Velmanickam L., Laudenbach D. and Nawarathna D., "Dielectrophoretic label-free immunoassay for rare-analyte quantification in biological samples", Physical Review E, vol 94, 11 Oct 2016. Doi:10.1103/PhysRevE.94.042408). Velmanickam L. had primary responsibility for simulation, calculation, sample preparation and experiments. Laudenbach D. was the primary developer of the electrode mask design. Velmanickam L. also drafted and revised all versions of this chapter Nawarathna D. served as proofreader and simulations, calculations, and results of the experiments conducted by Velmanickam L.

then mixed the beads and the sample to conjugate the antibodies and target analytes. After conjugation, we have re-suspended the polystyrene beads in testing buffer (this will be discussed in details below) and measured the crossover frequency. As predicted in the theoretical calculations above, our data indicates that crossover frequency is dependent on the number of antibody-analyte complexes on the polystyrene beads surfaces. We have found a relationship between cross over frequency and number of avidin-biotin conjugates, which can be used as a standard curve to find number of avidin molecules in unknown samples. Therefore, this technique can be utilized to quantify unknown level of target analytes in a biological sample. Our experiments were performed using the avidin molecules that are suspended in standard laboratory buffers. However, in real-world applications, where we apply this concept, for example, to find the molarity of biomarker proteins in blood, the results will not be affected by the non-specific binding of other molecules. This is because, the cross over frequency is dependent on the polarization of biotin-avidin or (analyte-antibody) with the applied electric field. If there is non-specific binding, depending on the number of non-specific molecules, it may produce a cross over frequency that is outside the standard curve generated for specific analyte-antibody conjugation. Furthermore, near the cross over frequency, DEP is very small and polystyrene beads will scatter from the Brownian motion. However, this happen when polystyrene beads are extremely close to its cross over frequency. Therefore error estimating cross over frequency is very small. Prior to our studies, Gagnon and co-workers have used the crossover frequency to detect the DNA hybridization on polystyrene beads [131]. We used their work as the basis for our work. In particular, we have designed and used new set of electrodes that can be used to easily identify the positive, negative and zero DEP forces. In addition, we have detected and quantified the conjugation of low amounts of biotin-avidin conjugates. We

have also studied the variation of the cross over frequency with number of biotin-avidin conjugates. In comparison with Gagnon's work, detecting protein binding events are extremely useful in biology and medicine than DNA hybridization. At the same it is technically challenging to detect the protein binding without the electrodes that we have developed. Further, our work will be the first demonstration of DEP based label—free ELISA. We will explain the details of experiments that we performed.

2.2. Theoretical calculations

To properly implement our concept in experiments, first, we have designed an electrode array that is capable of detecting DEP forces (positive DEP, negative DEP or zero DEP (cross-over frequency)) of polystyrene beads through a simple bright field microscopy observation. We then successfully fabricated the electrode arrays on commercially available glass wafers using traditional photolithography, metal sputtering and lift-off procedures [132]. All the electrodes were fabricated using 1000Å thick gold films.

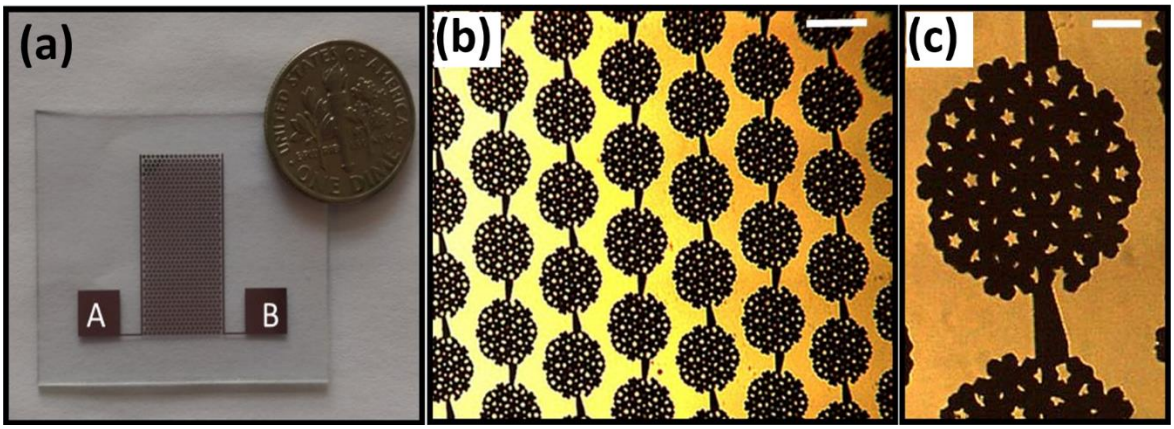

Figure 2.1: **Pictures of the PIDE electrodes utilized in the experiments**. **(a)** A Picture of a clean PIDE structures with connecting pads (A and B) to connect the electrodes to external function generator. **(b)** Section of PIDE structures showing how individual bead electrodes are placed, gap between electrodes and connection between individual bead electrodes. Scale bar indicates 500 μm. **(c)** Close-up of the single bead electrode showing hollow interior with uneven outer boundaries to generate large electric field gradients. Scale bar indicates 250 μm.

We have designed pearl-shape interdigitated electrodes (PIDE) in for crossover frequency experiments (Figure 2.1). In comparison with traditional interdigitated electrodes, PIDE electrodes are capable of generating high electric field gradients (∇E^2). Typical interdigitate electrodes generate electric field gradients in the range of 10^{12} V^2/m^3 [65]. However, our PIDE electrodes are generating about 2-3 times higher electric field gradients than the traditional interdigitated electrodes. This high electric field gradients are necessary for quickly detecting DEP forces of polystyrene beads for our high-throughput label-free immunoassay. In particular, depending on the frequency and the surface charges of the polystyrene beads, these high-electric field gradients are capable of establishing extremely high negative or positive DEP forces on polystyrene beads allowing clear distinction between them. Further, other forces acting on the

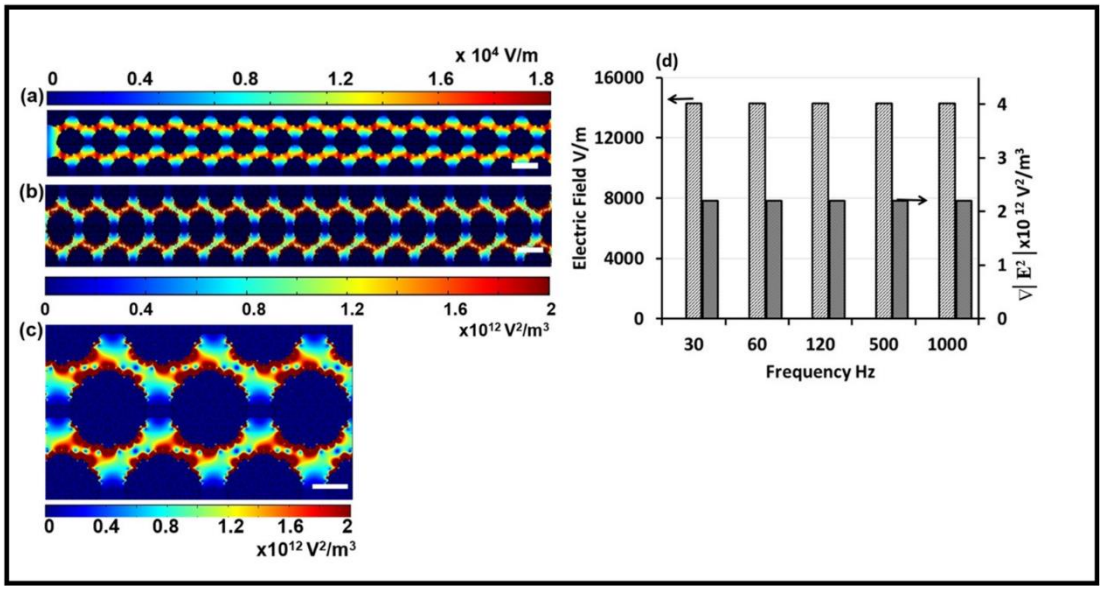

Figure 2.2: **COMSOL simulations results**. **(a)** Variation of the electric field at 120 kHz over PIDE electrodes. These electric fields are sufficient to polarize the polystyrene beads and generate DEP forces. **(b)** Calculated electric field gradients (∇E^2) at 120 kHz over the PIDE electrodes. Both electric field and electric field gradients are necessary to set-up DEP forces on the beads. **(c)** Close-up view of the electric field gradient (∇E^2) showing high and low electric field gradient regions in PIDE structures. When polystyrene beads are experiencing attaching or positive DEP, they are attracted to the high field gradient regions. Polystyrene beads move to the lowest field gradient regions when they experience negative DEP. **(d)** Variation of the average electric field and electric field gradients (∇E^2) with frequency. Scale bars indicate 500 μm in (a) and (b), 250 μm in (c).

beads such as viscous drag and buoyancy forces are much smaller than the DEP forces. Therefore, DEP forces are easily detectable. In addition, PIDE have designated regions for positive and negative DEP, where beads will be accumulated. Therefore, it is easy to characterize the DEP forces (+ or – DEP).

To quantitatively understand the electric fields and electric field gradients (∇E^2) generated by PIDE structures, we have utilized the commercially available COMSOL (COMSOL, Inc.) software and calculated the electric field and electric field gradients that we can expect from the PIDE structures. To set-up COMSOL calculations, briefly, PIDE were drawn to a scale using AutoCAD (Autodesk) software and imported into COMSOL software. We then used the AC/DC electric current (*ec*) module and frequency domain studies to calculate electric fields and field gradients. Furthermore, we assumed that a buffer solution (σ=1.67 S/m and ε_r=80.3) was filled over the electrodes. Further, an external potential (1 $V_{peak\text{-}peak}$) with a known frequency was applied to the electrodes and the electrode design was meshed using free triangular extremely fine mesh with maximum element size of 10 μm and minimum element size of 0.21 μm. Finally, we calculated the electric fields and field gradients for each frequency. Figure 2.2 illustrate the summary of the electric fields and field gradient calculations. Figure 2.2(a) indicates the electric fields generated by an external electric potential of 120 kHz on PIDE structures. Large electric fields are necessary to polarize polystyrene beads and generating DEP forces on polystyrene beads. Our electrodes are capable of generating maximum electric field of 1.8×10^4 V/m and this electric field is sufficient to polarize the polystyrene beads. Figure 2.2(b) indicates the variation of the electric field gradient (∇E^2) near PIDE structures. These electric field gradients were calculated for 120 kHz external electric potential. Figure 2.2(c) shows the high and low electric field gradient regions (positive and negative DEP forces). Blue colored

regions are negative DEP regions because of the lowest electric field gradient (~10^{11} V^2/m^3). The red colored regions are the positive DEP regions because the highest electric field gradients (~$3x10^{12}$ V^2/m^3). Figure 2.2(d) illustrate the variation of the average electric fields and electric field gradients with frequency. As expected, there is no variation with the frequency. Therefore, it can be concluded that polystyrene beads are subjected the same electric fields and field gradients in all frequencies

2.3. Experiments and results

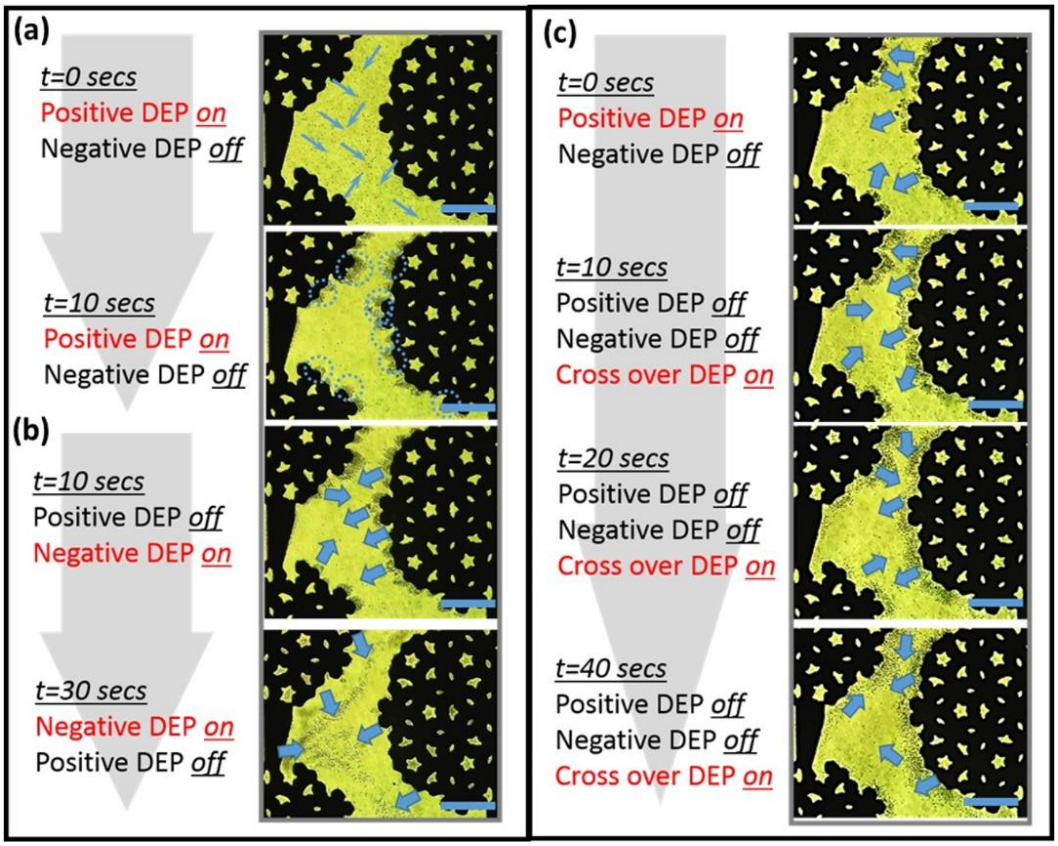

Figure 2.3: **Experimental scheme used to find the crossover frequency of the polystyrene beads**. The moving directions of polystyrene beads under various frequencies are indicated in arrows. **(a)** Experimental observation of positive DEP. During the positive DEP, polystyrene beads are moving to the highest electric field gradient (∇E^2) regions.**(b)** Observation of negative DEP. Note that the polystyrene beads are moving are moving to the lowest electric field gradient (∇E^2) regions (away from the electrodes). **(c)** Polystyrene beads are transitioning from positive DEP to crossover DEP. Note that at crossover frequency, polystyrene beads are gradually scattering over the PIDE electrodes. Scale bars indicate 100 µm.

and the variations in crossover frequency is dependent on the number of analyte molecules on the bead surfaces.

To demonstrate the proof-of-concept of our technique, we have used biotin-avidin conjugations. In particular, we studied the variation of crossover frequency with biotin-avidin conjugates on the polystyrene beads surfaces. Briefly, biotinylated polystyrene beads were purchased from Spherotech Inc. (0.74 μm diameter beads; 10,000 biotin molecules in beads surfaces). To conjugate avidin molecules (Vector Labs, Inc, ~$1.1x10^6$ beads/μL, fluorescently labelled avidin molecules) with biotin molecules that are on the surfaces of the polystyrene beads, we followed the manufacturer suggested procedure. Briefly, to have 100% (means 10,000 molecules) biotin molecules to be conjugated with avidin molecules, we incubated 3μL of avidin solution (1mg/mL) and 10μLpolystyrene beads for 30 minutes in room temperature. We then centrifuged the beads mixture at 5000 rpm for 12 minutes and supernatant were removed and added 400μL of testing buffer. We then pipetted 10μL (8x 10^{11} beads/μL) of polystyrene beads onto the commercially available glass slide and recorded a fluorescent image of the sample. The fluorescent intensity of the sample was measure using fluorescent image and the ImageJ software. Similarly, to have 75, 50, 25, 12.5 and 6.25% conjugations, we diluted the avidin solution appropriately and kept the other experimental parameters (incubation time, temperature and centrifuge speed) unchanged. Figure 2.4(a) indicates the variation of the measured fluorescence with avidin molecules. As we expect, fluorescence intensity is gradually increasing with number of avidin molecules.

The crossover experiments were performed in following manner. First, a clean PIDE electrodes were mounted on a low power microscope (OMFL600). We then pipetted a 10μL of biotin-avidin conjugated beads over the PIDE electrodes. We then connected the PIDE

electrodes to a commercially available function generator (HP 33120A). During the crossover measurement experiments, we first established the positive DEP by applying a low frequency electric field (~ 10 kHz). Reported literature and our experiments indicate that polystyrene beads experience positive DEP force at lower frequencies (<50 kHz) [65],[133],[134]. We have applied a low frequency electric field (~ 10 kHz) and observed the positive DEP. Since the positive DEP is always making the beads attract toward electrodes, we observed it very clearly (Figure 2.3(a)). We then switched the frequency and observed the negative DEP. Since the positive DEP is in the low frequency, the negative DEP must be in the high frequencies. The highest frequency that our generator can produce is 10MHz, we started with the highest frequency. During the negative DEP, beads must repel from the electrodes and move into the region where it has the lowest electric field gradient. Since we are changing the frequency from 10 kHz to 10 MHz, we were able to observe the repelling of the beads from electrodes. These steps are shown in the Figure 2.3(b). After establishing the negative and positive DEP regions, the cross over frequency must be between those two regions. At the cross over frequency, beads do not experience any DEP force, therefore it will scatter randomly through Brownian motion (Figure 2.3(c)). To locate the cross over frequency, we have used a simple binary search algorithm. Briefly, we calculated the average of the two frequencies (10 kHz and 1 MHz, average=505 kHz) and apply the new frequency and observe the DEP (whether positive or negative). If the DEP is negative, we took a new average between 10 kHz and 505 kHz. Similarly, if the DEP is negative, we took the a new average between 505 kHz and 1 MHz. We continued this process and located the cross over frequency. Figure 2.3 illustrate the implementation of these steps in experiments. In particular, PIDE provide regions where positive, negative and crossover DEP forces are easily detectable. Therefore, there is no need to have complex circuitry or algorithms. Typically, it take about 45-

60 minutes to manually find the crossover frequency of a polystyrene bead sample that has certain number of avidin molecules. This timing can be significantly reduced down to minutes through automation. Figure 2.3(a) demonstrate how did we determine the positive DEP of a sample. In positive DEP, note that polystyrene beads are getting collected in the high electric field gradient region as expected. As shown in the Figure 2.3(b), during the negative DEP, polystyrene beads are getting collected near the regions where lowest electric field gradient regions. At cross-over frequency, there was not DEP force acting on the polystyrene beads, therefore beads are free to move in any direction over the PIDE electrodes (Figure 2.3(c)). Figure 2.3(c) illustrate the how beads are gradually scattering over electrodes at the crossover frequency. This experimental procedure was utilized to experimentally find the cross-over

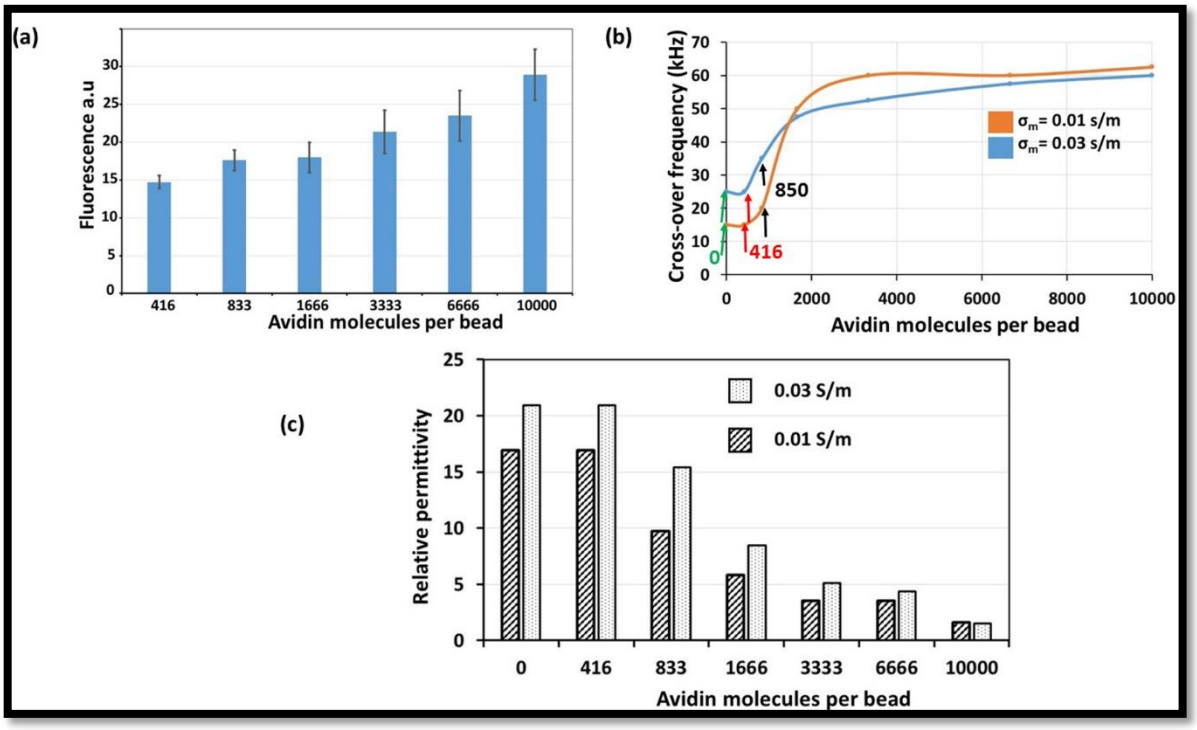

Figure 2.4: **Experimental and theoretical results**. **(a)** Variation of the fluorescence intensity of polystyrene beads with number of fluorescently labeled avidin molecules on their surfaces. **(b)** Experimentally measured crossover frequency of the polystyrene beads with avidin molecules on the surfaces. **(c)** Calculated relative dielectric constant of polystyrene beads with varying number of avidin molecules. This calculation was performed using the experimental data in (b).

frequency of polystyrene beads with avidin molecules on their surfaces. In addition, we have also repeated each experiment 2-3 times for repeatability.

To study the applicability of our techniques in low and high conductivity buffers, we have performed the crossover frequency experiments in two separate buffers (σ_1=0.03 and σ_2=0.01 S/m). Conductivity, σ_1, is comparable with common Phosphate Buffered Saline (PBS). PBS buffer was diluted by 100X in DI water and used as the low conductivity buffer (σ_2) in our experiments. Figure 2.4(b) shows the average crossover frequency (averaged using 2-3 experiments) for each condition (number of avidin molecules). The cross over frequency for zero and 460 avidin molecules are identical (Figure 2.4(a) red and green arrows) and therefore 460 avidin molecules cannot be quantified. From these experimental evidences, it can be concluded that our crossover frequency based quantification can quantify about 850 molecules (smallest bead quantity) per polystyrene bead (~ 1.4 zmoles per bead). The number of beads was calculated in following manner, for 100 % Biotin-avidin conjugation in a bead, there will be 10,000 avidin molecules on a single bead surface. To cover the beads 8.33 % of surface, there should be about 850 avidin molecules in a single bead surface. Furthermore, crossover frequency of the polystyrene beads is dependent on the number of avidin molecules on the bead surfaces and the conductivity of the buffer solutions. These variations can be explained theoretically using the expression derived for the crossover frequency (equation 1.4). To demonstrate the applicability of our technique in sensing applications in various biological buffers, we have plotted the variation of the cross over frequency with number of biotin-avidin conjugates (Figure 2.4(b)) and generated a standard curve. This standard curve can be used to find the number of avidin molecules of an unknown experiment.

The dielectric properties (conductivity or the dielectric constant) of the polystyrene beads strongly contribute to the crossover frequency [79],[133],[134]. Since the cross over frequencies of polystyrene beads with avidin molecules were below 1MHz (Figure 2.4 (b)), we were interested in finding how surface conductivities (surface conductivity is closely related to the biotin-avidin conjugation) and relative dielectric constants contribute to the measured cross over frequencies. However, surface conductance is closely related to the biotin-avidin conjugation as it determines the property of beads with biotin-avidin molecules. We first calculated the variation in the surface conductance of beads at cross over frequencies. To calculate the surface conductance, we have utilized the equation (1.4) and (1.5) with ε_m =80.3, ε_p =2.6, and σ_m = 0.03, 0.01 S/m. From our calculation, we found out that there is no change in surface conductance of polystyrene beads (K_s) and the value of the surface conductance is about 6.16 nS in all the experiments. We then calculated the ε_p at each cross over frequency and those results are indicated in the Figure 2.4(c). Since there is a significant variation in the dielectric constant from experiment to experiment. From these calculations, it can be concluded that avidin binding to the biotin molecules on the beads surfaces is reflected as change in dielectric constant.

2.4. Conclusions

In summary, we have proposed a new concept for developing label-free immunoassays. In addition to addressing the current technological gap in immunoassay, this technique can be developed into a *point-of-care* technology for quickly detecting other diseases such as myocardial infractions (heart attacks) and infections. Since our proposed technique is capable of quantifying few thousands of analytes (zmoles per bead), this can be developed to perform single-cell proteomics. To successfully implementing, it is required to integrate our technique

with microfluidics device design and instrumentation. Therefore, the research presented here holding a great promise in many important areas of biology and medicine.

Here we had some limitations while performing this study. We have detected 850 molecules for a bead. When we attempted to reduce the molecules per bead and determine the cross-over frequency, there were not much difference observed in the results. Meanwhile we used nearly 1000, 0000 beads for the experiment. Therefore the total number of detected molecules were multiplied by the number of beads. We performed the experiments by reducing the number of beads, and we could not go beyond a certain number of beads because we could not see the beads clearly during the experiment. Due to this limitations we designed a new study by integrating DEP and fluorescence-based platform to detect the target biomarker from serum sample, which study was discussed in the chapter 3.

CHAPTER 3. UTILIZATION OF INTEGRATED DIELECTROPHORESIS AND FLUORESCENCE BASED PLATFORM TO QUANTIFY RARE TARGET BIOMARKERS FROM BIOLOGICAL SAMPLES

3.1. Introduction

In this study we have demonstrated a development of a new technique for biomarker detection, which is suitable for use in early-stage disease detection in point-of-care settings. The underlying principal of the technique is the enhancement of the fluorescence of the target biomarker molecules by automated trapping and clustering using DEP [54],[79]. Studies have also focused on developing bio-sensing assays, but, to the best our knowledge, almost no studies have focused on developing DEP-based assays to detect biomarkers directly in body fluids [79],[133],[135]–[137]. Therefore, the main focus of our study is to develop a technique that has the potential to be used in diagnosis. We have utilized the DEP force to selectively trap fluorescently labeled target biomarker molecules in specific areas of an electrode array. We have then studied how the fluorescence varies with the concentration of the biomarker molecules and determined the limits of the new detection method. Moreover, trapping and clustering of molecules produce fluorescence spots that have fluorescence intensities well above background auto fluorescence. Therefore, weak fluorescence from low concentrations of biomolecules can be rapidly distinguishable without complex machinery or additional steps. Typically, large DEP forces need to be exerted on small molecules for rapid manipulation. To exert large DEP forces

---

This chapter was extracted from a published article in Biomedical Physics and Engineering Express (Velmanickam L., Fondakowski M. and Nawarathna D., "Integrated dielectrophoresis and fluorescence-based platform for biomarker detection from serum samples", Biomedical Physics and Engineering Express, 24 Jan 2018. Doi: 10.1088/2057-1976/aaa516). Velmanickam L. had primary responsibility for simulation, calculation, sample preparation and experiments. Fondakowski M. had primary responsibility for analysis. Velmanickam L. also drafted and revised all versions of this chapter. Nawarathna D. served as proofreader and simulations, calculations, and results of the experiments conducted by Velmanickam L.

on small molecules, such as antigens, large electric fields and electric field gradients are needed. These electric fields produce joule heating and thermophoresis, which destroy the target biomarker antigen molecules and lower the limits of detection [93],[135]. To overcome these problems, we have used polystyrene beads attached with target biomarker molecules as a carrier for biomarkers to transport them to specific places in the electrodes. Since the polystyrene beads are large particles, significantly smaller electric fields are needed to manipulate polystyrene beads. Therefore, adverse effects that are harmful to the sensing molecules will not take place.

3.2. Materials and methods

In this study, to demonstrate the proof-of-principle, we used commercially available, fluorescently labeled avidin molecules conjugated to biotin on a polystyrene bead surface. Biotin and avidin were chosen because they have been widely used in biosensor development studies [19]. The experimental factors that contribute to the biotin-avidin conjugation are well-known and conjugation is straightforward to perform [19]. Therefore, we could focus on the engineering of the biosensor and determine strengths and limitations. Figure 3.1 shows the steps of our technique. First, we have conjugated avidin molecules to the complementary biotin molecules that are immobilized on the surfaces of commercially available polystyrene beads (Steps a–h). We have then used the DEP force to concentrate the polystyrene beads in specific locations on an array of micro-interdigitated electrodes (IDE) (Step k). We will describe the steps of DEP based on the manipulation of the polystyrene beads below. Finally, we recorded a fluorescent image of the sample and developed a simple method to calculate the fluorescence intensity of the sample. We then studied the variation of fluorescence with the concentrations of the avidin molecules.

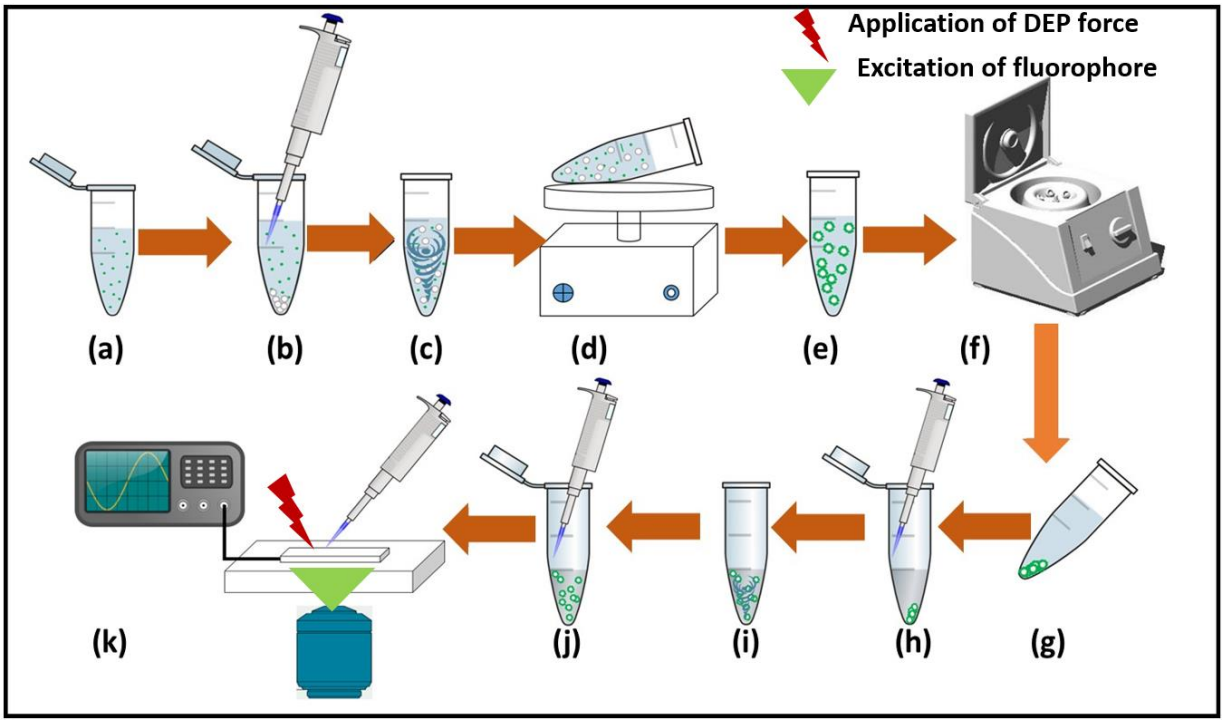

Figure 3.1: **Schematic representation of the steps of the biomarker detection technique**. **(a)** Biomarker sample (1mL), **(b)** Biotinylated beads are added to the mixture, **(c)** Gentle vortexing to mix the contents in the sample, **(d)** Incubation on a shaker to conjugate biotin and avidin, **(e)** Conjugated biotin and avidin molecules, **(f)** Centrifuge to remove the free avidin molecules, **(g)** Sample after centrifugation, **(h)** Supernatant was removed and 50 µl of 0.01xPBS buffer was added, **(i)** Gentle vortexing to mixture sample, **(j)** 10 µl of sample was pipetted, and **(k)** Perform the detection and quantification.

The selectivity is dependent on the molecular type, conductivity of the medium and frequency of the external electric field applied in the sample [79]. Selective polarization produces a movement in the particle towards non-zero electric field gradient regions. For example, polarized molecules move toward the highest (positive DEP) or lowest (negative DEP) electric field region, or it will stay stationary (zero force DEP) depending on the magnitude of polarization (positive, negative or zero) [79],[133],[134],[137]. From the DEP equation (1.4) the value of the CM factor is depends in the frequency-dependent dielectric properties of the biomolecule and the surrounding medium, which plays an important role in determining the magnitude and direction of the DEP force [79],[93]. From the CM factor theoretical bound, it is

clear that the highest positive DEP force is greater than the highest negative DEP force [79],[133],[134],[137].

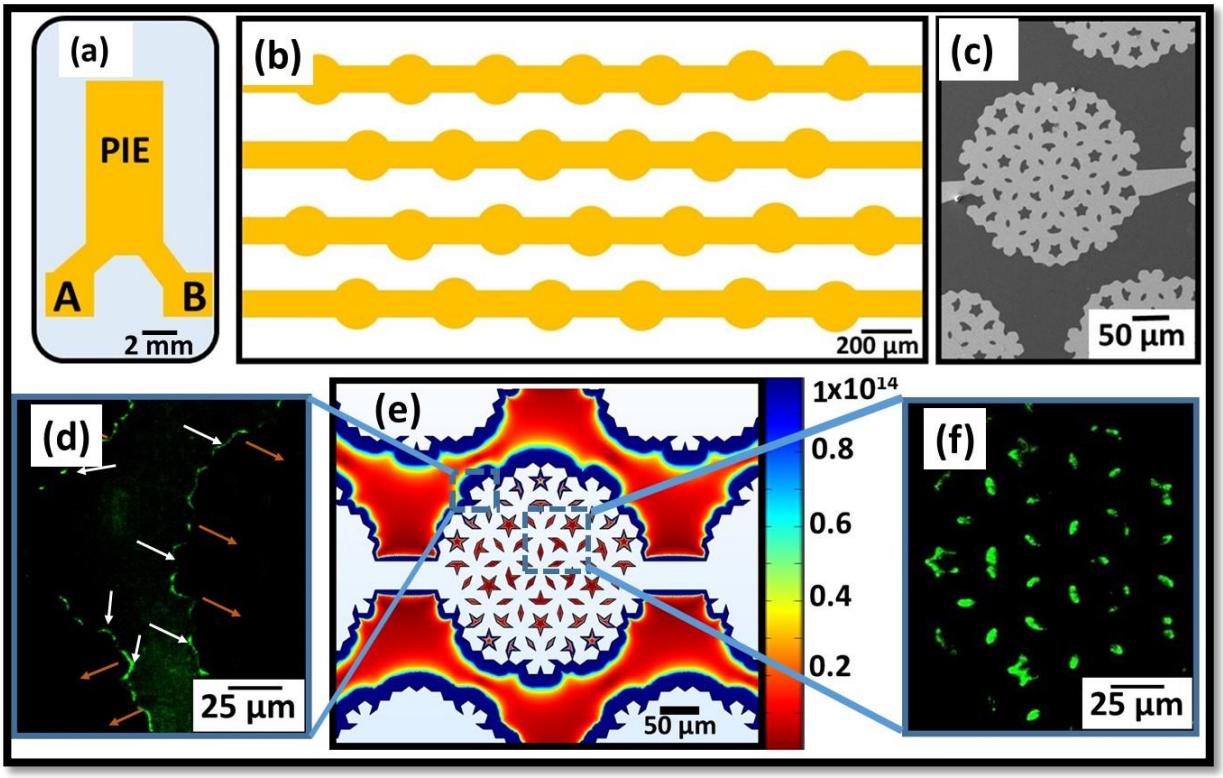

Figure 3.2: Design and fabrication of electrodes for DEP experiments. **(a and b)** Schematic view of the PIE electrodes. We have used the pearls shaped to produce large electric field s and field gradients needed to quickly detecting and quantifying biomolecules. **(c)** Scanning Electron Microcopy image of the fabricated PIE electrode. **(d)** Fluorescence image of the electrode when attractive DEP is applied and concentrated the beads in the highest electric field gradient regions, **(d)** calculated field gradient around one pearl of the PIE, **(e)** Fluorescence image of the electrode when beads are concentrated using negative DEP force.

In this study, we have used the combination of positive and negative DEP forces to attract and concentrate polystyrene beads in specific regions of the electrodes. First, we have used positive DEP (or attractive DEP) to concentrate the polystyrene beads in the electrode edges (Figure 3.2(d)). Moreover, attractive DEP will push free polystyrene beads toward the regions indicated by white arrows. We then changed the frequency of the electric field to produce negative DEP (or repulsive DEP) on the polystyrene beads to repel them (Figure 3.2(d)) towards

regions indicated in orange arrow to concentrate them in a specific location between the electrodes. Figure 3.2(f) shows the concentrated beads at specific locations on the electrode. The ability to manipulate polystyrene beads using DEP depends on the magnitude of the DEP force that is dependent on the electric field gradient produced by the electrodes. Therefore, the design of an electrode array that generates large electric field gradients in needed to produce larger DEP forces. We designed the electrodes using finite element modeling software and fabricated on a glass wafer. Interdigitated electrodes are commonly used for DEP experiments. Therefore, we have used our previous study as the basis [19] to develop an interdigitated electrode design capable of generating large DEP forces on polystyrene beads. Figure 3.2(a) shows the sketch of the electrodes with dimensions, and Figure 3.2 (b) shows a sketch of individual electrode pairs. We call these electrodes as pearl-shaped interdigitated electrodes (PIE).

To calculate the expected electric field gradients, we have used COMSOL software and built a three-dimensional model using an AC/DC electric current (*ec*) physics module with frequency domain studies. We have assumed that an external voltage of 10 $V_{peak\text{-}peak}$ with 120 kHz frequency was applied to the electrode. Studies have used electric potentials with 120 kHz to generate large DEP forces on biomolecules, and this was sufficient to manipulate them [19]. Finally, we calculated the electric field gradients generated by our electrode design. Figure 3.2 (e) shows the variation of the electric field gradient near the electrodes (x, y, z=50 nm plane). The calculated maximum and minimum electric field gradients were approximately $1x10^{14}$ V^2/m^3 and 10^{12} V^2/m^3, respectively. We have compared these numbers with those for the standard interdigitated electrodes that were utilized in the literature, and our electrodes generate electric field gradients approximately 2–3 times higher than the traditional interdigitated electrodes [19],[79]. Therefore, these electrodes generate 2–3 times higher DEP forces on polystyrene

beads. A larger DEP force is expected to facilitate speedy manipulation of the beads and eventually contribute to the detection speed of sensing. To fabricate the electrodes, we have first designed a photolithography mask in AutoCAD software and printed it on Mylar films using a dot-matrix printer (Fineline Imaging Inc, Colorado Springs, CO). The electrode was then fabricated using standard photolithography processes followed by metal deposition and a lift-off process [54]. Figure 3.2(c) shows a scanning electron microscope image of fabricated electrode on glass wafer.

We purchased avidin molecules (Excitation: 495–500 nm, Emission: 514–521 nm) from Vector Laboratories (Burlingame, CA, USA), and biotinylated polystyrene beads (diameter=0.74 μm) were purchased from Spherotech Inc (Lake Forest, IL, USA). The selection of 0.74 μm as a bead size is based on our ability to manipulate the polystyrene beads using DEP force. In particular, in previous studies, we determined that the polystyrene beads with a diameter ranging from 500 nm to 1 μm were easy to manipulate with DEP [54].

In experiments, we varied the molarity of the avidin molecules from μM to pM and measured the fluorescence of each concentration. Since the DEP force on a polystyrene bead is dependent on the number of biotin-avidin complexes on the surface, we have kept the number of biotin-avidin complexes on a bead constant for each avidin concentration by varying the number of polystyrene beads with concentrations of avidin molecules. The conjugation of biotin and avidin molecules was performed according to the manufacturer's instructions. Briefly, to achieve 100% labeling of biotin molecules (approximately 10,000 molecules of biotin were on the surface of a bead) with avidin molecules, a 1:30 ratio of avidin molecules to biotinylated polystyrene beads (1% w/v) was used. The sample (avidin molecules and biotinylated beads) was uniformly mixed with gentle vortexing for about 30 seconds. After that, the sample was kept on a

shaker (Ultra Rocker, BIO-RAD, Hercules, CA, USA) for 20 minutes at room temperature. Finally, the sample was centrifuged for 20 minutes at 5000 rpm. The supernatant containing the unbound avidin molecules was removed, and 50 µl of 0.001 X PBS (σ=0.01 S/m) buffer was added to the tube [54]. We used low-conductivity buffer to avoid adverse effects when we use DEP force, such as electrolysis [54]. Studies have reported that biotin-avidin duplexes were stable in this low-conductivity buffer. Finally, the sample was uniformly mixed by gently vortexing for about 30 seconds. We have taken many precautions during this assay to make sure that we will have an intact sample of biotin-avidin duplexes. For example, we have covered the centrifugation tube with aluminum foil to avoid bleaching the avidin molecules by exposure to light.

To prepare the electrodes for experiments, we have cleaned the electrodes using a 75% ethanol solution, washed them in DI water, and then dried them using pressurized air [19]. The clean electrode was placed firmly on the electrode holder using commercially available adhesive tape, and the electrode holder with the electrodes was mounted on a low-power fluorescence microscope (Omano, OMFL600, Roanoke, VA, USA). Next, the electrical connections to the electrodes were made by connecting them to a function generator (Tektronix, AFG 3021B, Beaverton, OR, USA). We then determined the frequencies needed to generate positive and negative DEP forces on the beads. Studies have indicated that polystyrene beads experience positive DEP forces at lower frequencies (<500 kHz) (6, 16-18). Therefore, we varied the frequency below 500 kHz and determined the most suitable frequency (10 Vp-p and 10 kHz) needed to generate the largest DEP force on the polystyrene beads with conjugated biotin-avidin molecules. Similarly, to find the appropriate negative DEP frequency (repulsive DEP), we varied the frequency from 500 kHz–5 MHz. The largest repulsive DEP force was generated at 3 MHz.

These attractive and repulsive DEP forces were calculated by recording videos when beads were moving with positive or negative DEP frequencies. We then calculated the velocities of beads because velocities are proportional to the DEP force on the beads. These frequency values of the positive and negative DEP forces are dependent on various factors, such as the conductivity of the buffer, the type of molecules that we have on the surface of the polystyrene beads, and the diameter of the beads [79],[133],[134],[137].

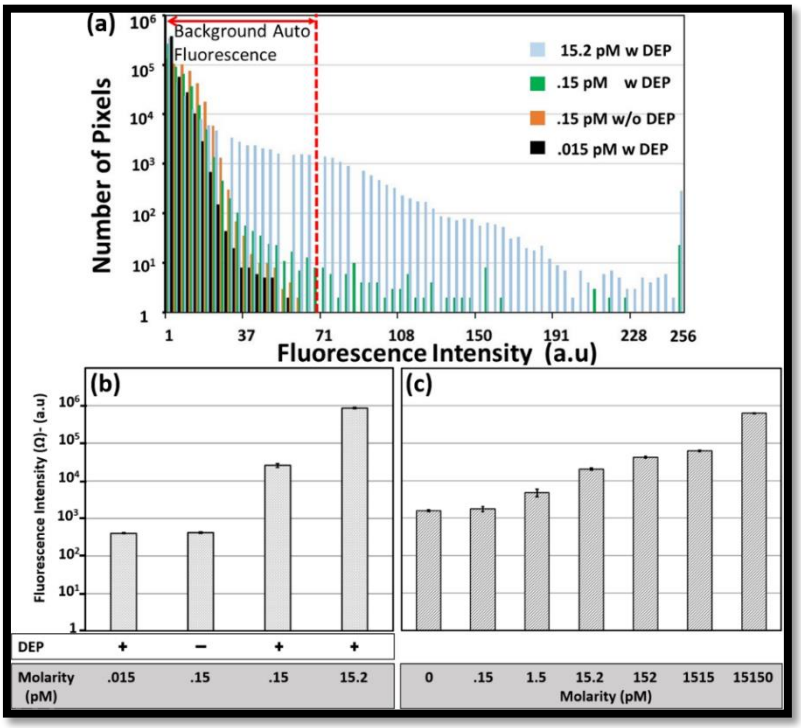

Figure 3.3: Results from the dielectrophoretic based detection and quantification of Avidin molecules. **(a)** Variation of fluorescence with molarity of the Avidin molecules, **(b and c)** Standard curve to be used in the finding molarity of unknown sample. (b and c) shows the variation of fluorescence with number of pixels for avidin molecules that were suspended in PBS buffer and serum respectively.

After figuring out the frequency values, we have performed avidin detection experiments. The first experiment was performed by spiking in avidin molecules of varying concentrations (from μM to pM) in 1X PBS buffer (positive control). The second experiment was performed by

spiking avidin molecules (μM to pM concentrations) into diluted serum samples (1:99=serum: DI water).

After conjugating biotin and avidin, we suspended the beads in 0.001X PBS buffer and loaded the sample on the electrodes to measure the fluorescence. First, we have applied the positive DEP force for about 15 seconds to bring biotin-avidin-labeled polystyrene bead electrode edges from all three x, y, and z directions. Then negative DEP was applied to concentrate beads in the regions where there was the lowest electric field gradient. Finally, we recorded a fluorescent image of the sample [79],[133],[134],[137] . Each experiment was repeated to assess reproducibility.

We used ImageJ software to analyze the fluorescent images (https://imagej.nih.gov/ij/). First, we determined a set of parameters to enhance the brightness, sharpness, and contrast of the images. We used these parameters to process all the images. We then extracted the fluorescent intensities of each pixel from each modified image by using a simple, custom-built software program. We then plotted the extracted fluorescence intensity of each pixel of the image as histograms. Figure 3.3(a) shows the variation in fluorescence intensities with respect to the concentration of the avidin molecules. As indicated in Figure 3.3(a), there was a significant enhancement in the fluorescence when DEP force was used to concentrate polystyrene beads with conjugated avidin and biotin molecules (see the bar charts for 0.15 M with and without an applied DEP force). We then calculated the total fluorescence of each image for each concentration. We used the fluorescence intensities that were above 70, and the total fluorescence intensity (Ω) was defined as follows:

$$\Omega = \sum_{i=70}^{256} I_i \,.\, n_i \tag{3.1}$$

where n_i is the number of pixels corresponding the I_i. We then plotted the variation of Ω with the molarity of avidin molecules (Figures 3.3(b–c)). Figure 3.3(b) shows the detection of the avidin molecules that were spiked into PBS buffer, and Figure 12c shows the avidin detection data from the diluted serum samples. Note that the fluorescence intensity varies with the molarity of avidin in both samples. We then selected a concentration that can be expected in early state disease progression (0.15 M) for comparison, Figure 3.3(b) shows the comparison of fluorescence intensity with and without DEP-based clustering. Note that the concentration of polystyrene beads using DEP force has increased the total fluorescence of the sample by 100-fold when compared to the fluorescence of the sample that did not experience DEP force. The 100-fold improvement is significant because it will improve the detection limit by at least 100 times. Figure 3.3(c) shows the detection of various molarities of avidin from diluted serum samples. The smallest molarity that we could detect was 1.5 pM. In comparison, the smallest molarity that ELISA can detect is about 40 nM [138].

3.3. Results and discussion

In summary, we have demonstrated a new sensing technique that utilizes DEP forces to concentrate polystyrene beads and enhance the fluorescence of biomarkers that are on the bead surfaces. This technique improves biosensing performance in the following ways. First, since the DEP force is actively concentrating polystyrene beads in well-defined locations within the electrodes, losing beads during the analysis will not take place. This is particularly important when detecting and quantifying rare target molecules. Second, the concentration of beads in a location will increase the fluorescence intensity of that location over background auto fluorescence. Therefore, our technique is capable of differentiating signal from background auto fluorescence. This also plays an important role when detecting and quantifying rare target

molecules. Finally, there are no complex steps or instrumentation needed to detect/quantify biomolecules. This technique can also be adopted for use in disease diagnostics in clinics or resource-poor settings. As shown in Figures 3.3(b–c), co-relation between the molarity and fluorescence can be used to determine the molarity of unknown sample. In addition, using this data, we have calculated the limit of detection of our technique. Finally, this technique is not limited to antigens. This can easily be modified to detect and quantify DNA, mRNA, and miRNAs, or it can be developed to detect multiple targets in a single device. Therefore, the research presented here can be a first step toward early diagnosis of diseases like cancer and heart disease in point-of-care settings or even in the home.

During this study we performed experiments to do the detection below pM (fM-aM) concentration. The limit of detection obtained from this study was 1.5pM, when we reduce concentration of the molecules further we couldn't observe any fluorescence signal. But in the real world problem it have been proved the disease related target bio-markers are available in the concentration of fM and aM. Therefore this technique is not suitable for the detection of target biomarkers in less concentrations than pM. Therefore we investigated another approach by integrating DEP and plasmonic enhancement to detect rare target biomarkers by enhancing the fluorescence emission by million-fold, which study was described in chapter 4.

CHAPTER 4. UTILIZATION OF DIELECTROPHORESIS AND PLASMONIC PLATFORM FOR RARE BIOMARKER DETECTION

4.1. Introduction

Among the promising methods available to quantify the target disease related biomarker molecules, fluorescence-based optical sensing techniques involve fluorescently labeling and measuring the fluorescence intensity of the target biomarkers in the sample. The fluorescence intensity is then converted to molarity and the number of target molecules [139]. The detection limit (or limit of detection) is an important factor in sensing because it indicates the smallest amount of detectable molecules. The limit of fluorescence detection is not sufficient to detect many disease-related biomarkers, especially in the early stages of disease development [140]. To address this issue, interactions of metal surfaces, particles and colloids with fluorophore molecules have been utilized in assays. Studies using silver or gold colloidal metal films and placing fluorophore molecules near those metals have reported producing undesirable chemical reactions between the fluorophore and metals such as metal etching by halide ions [125]. Therefore, additional studies were performed with modified metal colloidal films using about 10-nm glass films, and these studies reported an approximate 20-fold enhancement of fluorescence [125]. Additionally, nano-fabricated metallic nano-structures have been used in experiments to further improve the fluorescence enhancement of fluorescence-based assays [118],[121].

This chapter was extracted from a published article in Biomicrofluidics (Velmanickam L., Fondakowski M., Lima Jr. I.T., Nawarathna D., "Integrated dielectrophoretic and surface plasmonic platform for million-fold improvement in the detection of fluorescent events", Biomicrofluidics, Vol 11, 22 Aug 2017. Doi: 10.1063/1.5000008). Velmanickam L. had primary responsibility for simulation, calculation, sample preparation and experiments. Fondakowski M. had primary responsibility for analysis. Lima Jr. I.T. was the primary developer of the fluorescence lifetime measurement setup. Velmanickam L. also drafted and revised all versions of this chapter. Nawarathna D. served as proofreader and checked the simulations, calculations, and results of the experiments conducted by Velmanickam L.

Fabrication of metallic nano-structures is typically performed using an E-beam lithography tool [141].

Unfortunately, production of metallic nano-structures using an E-beam lithography tool is a complicated process that is expensive, time-consuming and can produce only small amount of nano-structures that can handle only small sample volumes. Thus, nano-fabricated metallic nanostructures with E-beam lithography is not feasible in a real diagnosis assay. To address this issue, studies have focused on producing metallic nano-structures using non-conventional methods [119],[142]. These nano-structures are easy to manufacture, cost effective and sufficient for handling large sample volumes. With these structures, studies have focused on improving the detection limits and sensitivity of fluorescence-based assays, particularly using the fluorophore and metal interactions, which are also called as surface plasmonic effects [119],[142]. In these methods, the interaction of metallic nanostructures and fluorescently labeled biomarkers near metal and dielectric interfaces was utilized to quantify biomarkers as they increase fluorescence intensity [119]–[121]. For example, Fu et al. demonstrated an increase of up to 1,000-fold in the fluorescence emission [119].

To drastically improve the detection limit of all these plasmonic-based sensing techniques, fluorescently labeled biomarkers would need to be placed within about >5 nm from metallic nanostructures (hotspots) [119],[122],[126]. Because of this limitation, detection is limited to the molecules that are about 5-20 nm from hotspots. To address this issue, we have used dielectrophoretic force to place the biomarkers on hotspots and studied the fluorescence intensity and lifetime. DEP is a process in which biomolecules experience a force, resulting in movement to the area that has the highest or lowest electric field gradient ($\nabla(|E|^2)$ [143]. Theoretical studies have shown that metallic nanostructures produce a greater fluorescence

enhancement compared with the colloidal metal films, and thus, we selected metallic nanostructures for our study [126].

In this study, we used fluorescently labeled Avidin (protein) molecules. Detection of protein is specifically important in diagnosis but most protein detection applications currently rely on traditional methods such as spectrometry and antibody-dependent methods. However, there are several sensitive methods available for detection of nucleic acids (DNA and mRNA), such as real-time polymerase chain reaction, micro-array techniques and gel electrophoresis [144]. These methods are commonly used and detection limits down to a few molecules are possible using these methods. In this regard, studies have reported detecting up to fM levels of nucleic acids [145].

Dielectric properties of nucleic acids were investigated by number of research groups and reported that nucleic acids have semiconducting-like properties [146],[147]. In addition, frequency dependent polarization mechanisms are well understood for nucleic acid molecules [79],[148]. Therefore, designing and implementation of assays that involve DEP forces are doable. In comparison, studies have reported that dielectric properties of proteins are more diverse than nucleic acids and dependent on number of parameters such as buffer conditions, molarity and size of the proteins [146]. Therefore, development of sensing assays that use DEP is challenging. Studies that are focused only on using plasmonic effects to detect proteins have reported the detection limit of 1μM [118][17]. Therefore, in this study, our starting molarity of Avidin molecules that we have used in experiments was 1 μM. Since the DEP force on protein molecules is significantly weaker than nucleic acids, we have developed a new electrode array that produces large electric field gradients. This high electric field gradient produce large DEP force on protein molecules. Since we integrate DEP force and plasmonic effects of fluorescently

labeled protein molecules, there must be a simple and scalable electrode design and micro-fabrication method that allows the production of integrated metal structures with hotspots. In this study, we have developed, tested and manufactured Pearl-shaped Interdigitated Electrodes (PIDEs) for integrated DEP and plasmonic experiments. We will present a detailed description about each important component of our method, experiments and results below.

4.2. Materials and methods

A number of nano-scale metal structures (e.g. Bowtie nano-apetures) have been successfully used in the context of plasmonic-based fluorescence detection [149]–[151]. Since we are combining DEP and plasmonic effects in our experiments, moreover, using DEP force to

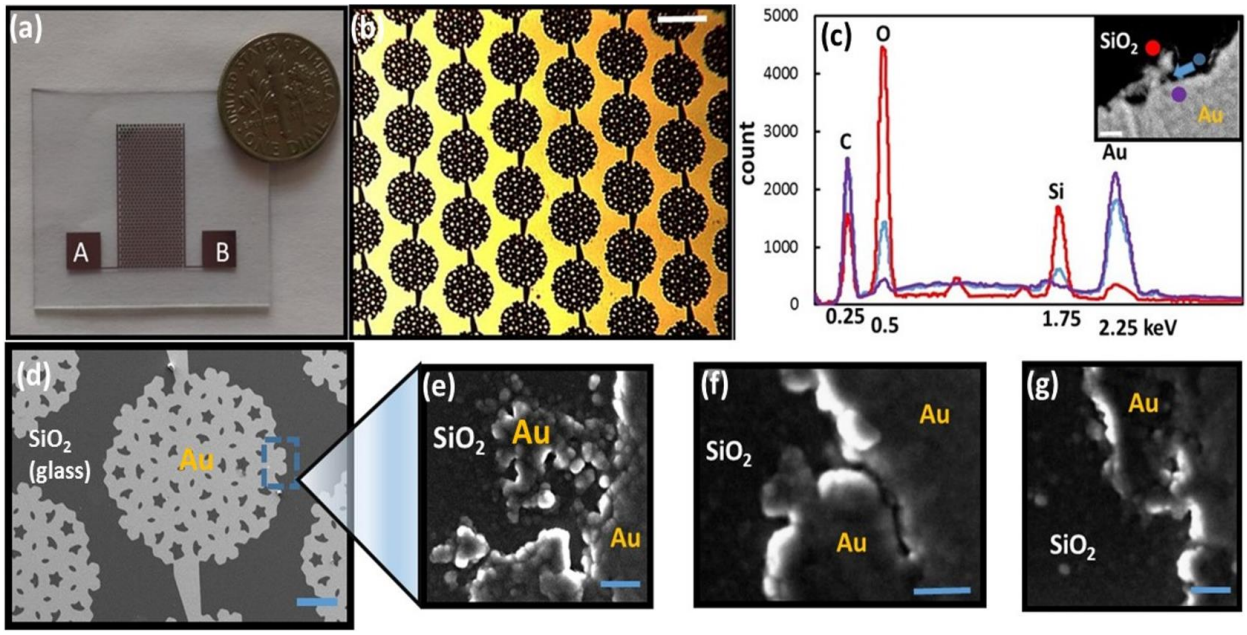

Figure 4.1: **Fabrication and characterization of PIDEs and hotspots for fluorescence experiments**. **(a)** Final version of the device that we have used in experiments. External electric potential was applied at A and B. **(b)** Close-up view of the PIDE array showing how PIDEs are designed and fabricated (scale bar 200 μm). **(c)** Characterization of the hotspots using EDS. The hotspot shown in the inset was characterized using EDS and spectra are shown in the figure. Scale bar of the inset 100 nm. **(d)** Characterization of the hotspots using SEM. Low magnification view of a PIDE (scale bar 50 μm). **(e, f and g)** The SEM images showing hotspots of various sizes and shapes (scale bars 200 nm).

place molecules on the hotspots, these plasmonic structures are not directly applicable to our experiments.

Further, fabrication of those nano-scale metal structures requires sophisticated equipment (e.g. electron beam lithography) and nanofabrication facilities. Therefore, first, we have designed and fabricated a new electrode design that allows us to establish a large DEP force on molecules while at the same time producing hotspots for the detection of molecules using plasmonic effects. Interdigitated electrodes (IDE) have been commonly used in the DEP experiments [152]. IDEs have been used in high-throughput manipulation of biological cells and molecule [152]. IDEs provide a simple electrode structure that generates the extremely high electric field gradients needed for DEP-based cell/molecule manipulation. Since we use DEP and plasmonic-based detection, traditional IDEs are not a viable solution for our experiments. Therefore, we designed and used the pearl-shape interdigitated electrodes (PIDE). Pictures of our PIDE are shown in Figure 4.1(a, b and d). In comparison with traditional interdigitated electrodes, PIDE electrodes are capable of generating higher electric field gradients ($\nabla(|E|^2)$ than traditional IDEs. Typically, interdigitated electrodes generate electric field gradients in the range of 10^{12} V^2/m^3 [54],[79],[143], and our PIDE electrodes are generating about two to three times higher electric field gradients than the traditional interdigitated electrodes. These high electric field gradients are necessary to rapidly concentrate biomarker proteins in the hotspots.

We then fabricated PIDEs using standard microfabrication techniques. The details of the fabrication are published elsewhere [54],[87]. We then produced hotspots in the periphery of the pearls of our PIDEs. The production hotspots are achieved through careful over-exposing of photoresists films to UV light during the photolithography. We then developed the photoresist films, sputtered 1000Å, Au and lifted off photoresists film in acetone to fabricate the PIDE with

hotspots at its periphery. This fabrication process produced a large number of hotspots with various shapes and sizes. A few of the shapes of the hotspots are shown in Figure 4.1(d, e, f, and g). This was a repeatable process that we used to produce hotspots throughout this report.

To gain a deep understanding on how the integration of DEP and hotspots can potentially enhance the surface-plasmonic effects, we used the scanning electron microscope (SEM) to image the locations of the hotspots and energy dispersive spectroscope (EDS) to perform an elemental analysis of the hotspots [153]. The SEM images were used to measure the dimensions of the hotspots (see Figure 4.1(d, e, f, and g)). Since our fabrication technique produces a large number of randomly distributed hotspots with various sizes and shapes, we do not have to choose a fluorescence dye that matches the plasmon resonance [119]. However, SEM images do not provide detailed elemental characterization of hotspots (locations of metals and dielectrics). To understand elemental composition of our hotspots, we have performed EDS analyses. In particular, we have used the "point-and-shoot" technique in the EDS software and determined the elements present in the hotspots. A typical result of an EDS analysis of a hotspot is indicated in the Figure 4.1(c). Note that if the DEP-placed biomarker molecules on the dielectric material is between gold electrode (violet color dot) and the gold arm (red color dot), it will be subjected to surface plasmon effects.

To quantitatively understand the electric field gradient, $\nabla(|E|^2)$, generated by the PIDE structures, we have used the AC/DC module of commercially available COMSOL (COMSOL, Inc.) software and calculated the expected electric field gradients. In this calculation, the PIDE were first drawn to scale using AutoCAD (Autodesk) software and then imported into the COMSOL software. We then assumed that a buffer solution (σ = 0.03 S/m and ε_r = 80.3) filled the space above the electrodes. We used the swept mesh technique to mesh PIDE electrodes.

This is needed to properly mesh nano and micro scale features of our electrodes. Briefly, first, we meshed x-y (z=0) plane of the electrode using "Free Triangular Mesh" with maximum element size 90 nm and minimum element size 1 nm. We then swept the "Free Triangular Mesh" in z direction with minimum and maximum mesh size of 5nm and 1nm respectively. This procedure allowed us the successfully mesh our electrodes. Further, we also assumed that an external potential with a frequency (120 kHz) and voltage (10 V_{p-p}) was applied to the electrodes. This is the AC potential that we have used in our DEP experiments. We chose 120 kHz because it has been reported that the positive DEP force will be maximum at 120 kHz for biomarker molecules [143]. Finally, we calculated the electric field from which we extracted the electric

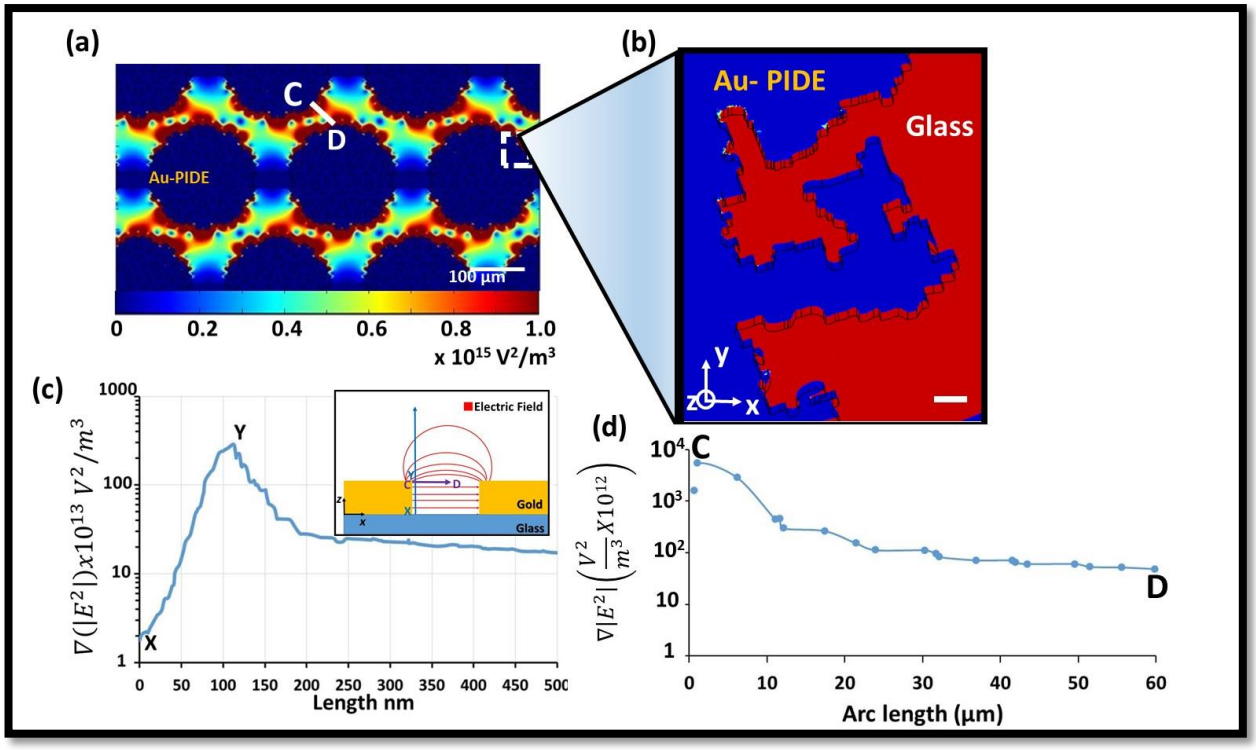

Figure 4.2: Calculated electric field gradients ($\nabla(|E|^2)$) near the electrodes and hotspots. **(a)** Calculated electric field gradients on the PIDEs in the x-y plane (z=100nm) **(b)** Close-up view of the electric field gradient of hotspots in z=100 nm plane. We have used the Figure 13(e) for this calculation. Scale bar indicate 200 nm. **(c)** Variation of the electric field gradient in the z direction. "X" indicates the z=100 nm plane and "Y" is the top plane of the hotspots. **(d)** Variation of the electric field gradient along the contour C-D (z=100 nm, Figure 14(a)).

field gradient in the vicinity of our PIDE structures.

In Figure 4.2(a), we show the calculated electric field gradient in the x-y plane (z=100nm) of the PIDE electrodes. There are high and low electric field gradient regions in the PIDE, blue colored regions have the lowest electric field gradient (~10^{12} V^2/m^3) and red colored regions have the highest electric field gradients (~$3x10^{15}$ V^2/m^3) [143]. We then calculated the variation of the electric field gradient along the contour C-D (Figure 4.2(d)). According to this calculation, in comparison, the DEP force is only about 70-80 times smaller at 60 μm (point D) than the DEP force at point C. To further understand the DEP-assisted molecular placing in the hotspots, we calculated the energy $\left(\frac{1}{2}\alpha E^2\right)$ provided by the external electric field to the molecules. We then compared the electric energy with the ground state energy of the molecules (kT; k is the Boltzmann constant; T is the average temperature on the electrodes). For the DEP force to be effective, the energy provided by the external electric field must be greater than the ground state energy of the molecules. For comparison, we calculated these energies along the contour C-D, and results are shown in the Figure 4.4(a). Since the energy provided by the electric field is larger than the ground state energy, it can be concluded that positive DEP will bring molecules from 50-60 μm away from the interface and place molecules on the hotspots for quantification through surface plasmonic effects. Since this calculation shows the variation of $(\nabla(|E|^2)$ in the x-y plane (along the contour C-D), we performed another calculation to find the variation of $(\nabla(|E|^2)$ in the z direction. The $(\nabla(|E|^2)$ in the z direction will produce DEP force on molecules in z-direction. In parallel, we have used the formula (above) and calculated the energy provided to the molecules by the electric field. We then compared the energy of the molecules to the ground state energy of the molecules. Our calculation shows that, at z=500nm (x=y=0), energy provided by the electric field is about 4 times greater than the ground state of

the molecules. Therefore, the electric field gradient in the z direction will produce a sufficiently large DEP force to bring molecules from z direction and combine with DEP in the x-y to place molecules in the hotspots. Furthermore, molecules that are far away from electrodes (z>> 500nm) will not be capable of using the DEP force to get trapped in the hotspots. One can use other forces such as electrophoretic force to bring those molecules to closer to the electrodes so that DEP force will be strong enough to place them in the hotspots. Other option will be to design the height of the channel within the DEP active area. Then DEP force will be sufficient to trap all the molecules in the hotspots. Figure 4.2(b) illustrates the variation of $(\nabla(|E|^2)$ in the z=100 nm plane and Figure 4.2(c) shows the variation of $(\nabla(|E|^2)$ in the x-z plane. From these analyses, it can be concluded that highest (∇(|E|^2) is generated at the top edge of the hotspots (Figure 4.2(c)). Therefore, these top edges (indicated as "Y" in the Figure 4.2(c)) will have large number of molecules collected through DEP. This analysis agrees with the experimental results

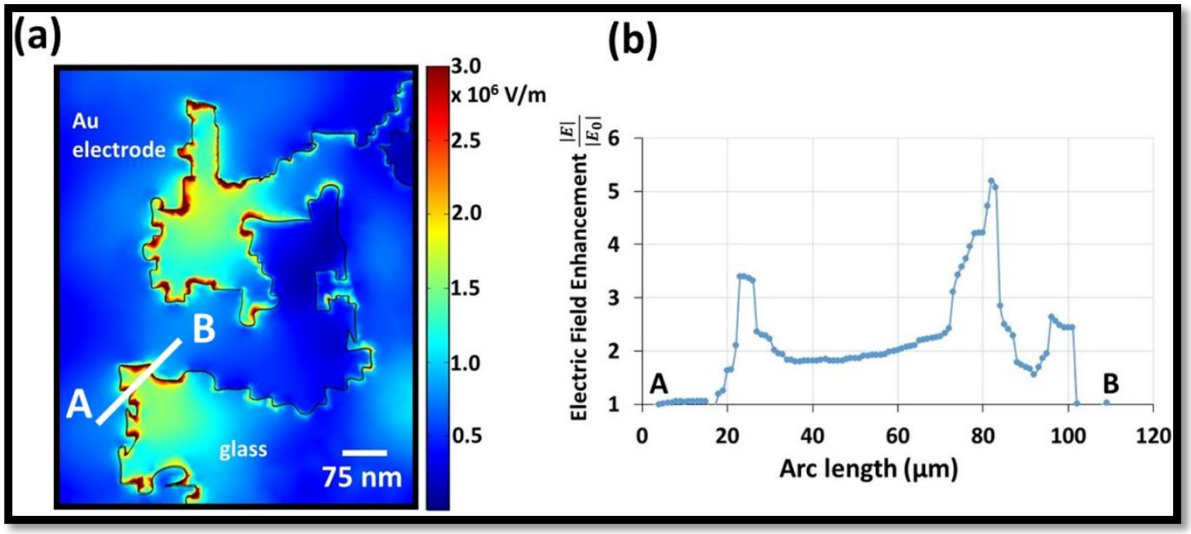

Figure 4.3: Calculated electric field enhancements due to the plasmonic effects. **(a)** We have used the SEM image of the Figure 4.1 (e) and used the COMSOL software to calculate the expected electric fields in the sample when 1mW light was applied perpendicular to the sample. **(b)** Calculated the electric field enhancement along the contour A-B of the Figure 4.3(a). This demonstrates the typical electric field enhancement that we expect from the hotspots. E_o is the electric field that is away from the hotspots.

in Figure 4.5(a) inset, where we observed the concentrating molecules at the top edges of the hotspots.

Next, we performed another COMSOL calculation to find the expected electric field enhancement near hotspots from the plasmonic effects. This electric field enhancement is expected when we excite the fluorescent biomarker molecules using the appropriate light source. To perform the calculation, we first drew the hotspots in AutoCAD software using a SEM image of our actual hotspots (Figure 4.1(e)) and imported into the COMSOL software. We then used the wave optics module of the COMSOL software and solved the traditional wave equation. In this application, when we assume the electric field as a planar traveling wave, the wave equation transform into equation (4.1). COMSOL software solved the equation (11) and calculated the expected electric field distribution and electric field enhancement near hotspots.

$$\nabla \times \mu^{-1}(\nabla \times E) - k_0^2 \left(\varepsilon_r - \frac{j\sigma}{\omega \varepsilon_0}\right) E = 0 \tag{4.1}$$

Where E is the electric field, μ = permittivity, k_0 = wave number, σ=electric conductivity, ϵ_r= relative dielectric constant, ϵ_0= dielectric constant of air, ω = angular frequency. We have also assumed that hotspots were made out of Au and a transverse electric wave with 500 nm wavelength and 1mW power passing through the hotspots. A 500-nm wavelength was chosen because it is close to the actual excitation wavelength that we have used in experiments. Figure 4.3(a) indicates the electric field distribution near hotspots. As we would expect, there is large electric field near hotspots. Published literature has been shown similar electric field distribution near metallic nanostructures [154]. For comparison, we calculated the electric field variation across the contour A-B. This will also provide good understanding of how the electric field varies across the hotspots. The contour A-B goes across a number of hotspots and Figure 4.3(b) shows the electric field enhancement across A-B and the maximum electric field enhancement

near our hotspots is about six-fold. Most of the published literature has reported about a three-fold electric field enhancement [119]. This electric field enhancement directly contributes to the fluorescence of Avidin molecules. Studies have shown that enhance electric field increase the fluorescence emission of Avidin molecules through "Lightning Rod Effect" [126]. In addition, the plasmonic hotspots increase the radiative decay rate of the fluorophore and therefore lifetime of the fluorophore will have a reduction [126]. Through this characterization, we have fully understood the abilities of electrodes to generate DEP and plasmonic effects.

In this high electric field and its gradients, there can be significant Joule heating resulting in a temperature increase near the electrodes. If the temperature is too high, the molecules that are being detected will be exposed to the high temperature and loss of their functionality. To understand the Joule heating in our PIDE electrodes, we have calculated the temperature increase ($\Delta T = (T_{actual} - T_{room});\ T_{room} = 300K$) in our PIDEs using COMSOL software.

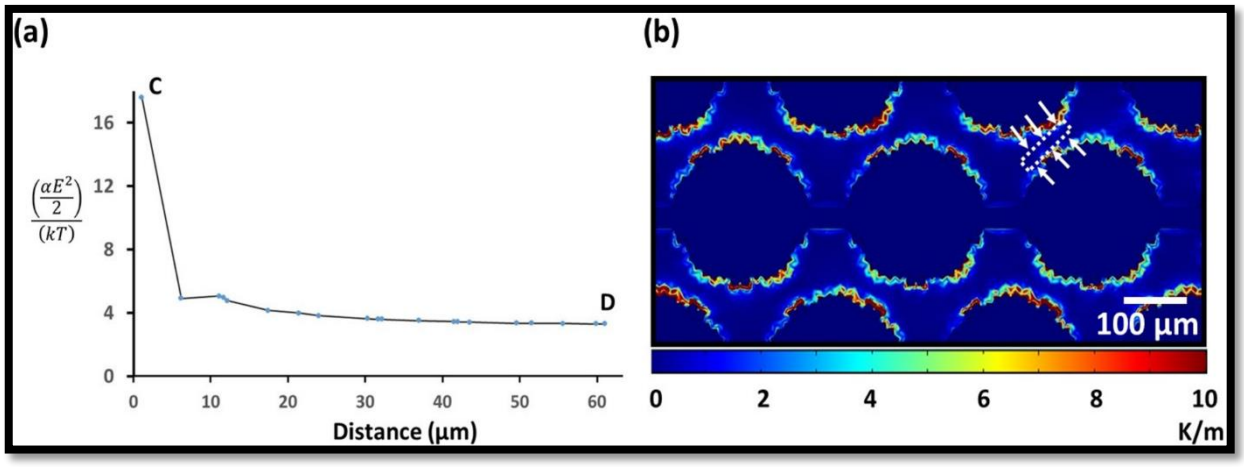

Figure 4.4: Comparison of energy harvested by biomolecules from AC electric field to ground state energy and thermophoretic effects on molecules. **(a)** Comparison of energy harvested from the electric field to ground state energy. Note that almost all molecules that are in the sample harvest at least four times more energy than the ground state energy. **(b)** Calculation of the temperature gradient near electrodes. This temperature gradient will produce thermophoeretic forces on molecules on biomolecules.

Briefly, we first calculated the electrical energy supplied to the surroundings through PIDEs. We then assumed that electrical energy is converted to the thermal energy through the

temperature increase. Through this calculation, we have found that a roughly 2° temperature increase (above the room temperature) will take place during the experiments, and this temperature will not cause any damage to the molecules. This result (temperature increase) can be deduced from the published work by others [155]–[157]. In addition, under this temperature distribution, one expects thermophoretic force (TP) on molecules through thermophoresis. The TP force on molecules causes thermodiffusion, (*j*) mathematically represented as,

$$\vec{j} = -D_T c \nabla T \tag{4.2}$$

D_T is the thermophoretic mobility, *c* is the concentration of molecules and ∇T is the temperature gradient. According to the equation (4.2), the TP will push the molecules away from the places where there are high temperature gradients. To further understand the motion of molecules through TP, we have extended our temperature calculation and determined ∇T. Figure 4.4(b) indicates the variation of ∇T on our sample. The thermodiffusion will push the molecules away from the electrode boundaries to the region indicated in the white box in the Figure 4.4(b). At the same time, DEP will attract the molecules toward the electrode boundaries (Figure 4.2(a)). If the electrodiffusion is dominant, there must be an accumulation of molecules in the area indicated by the white rectangle (Figure 4.4(b)). However, in experiments, we did not observe any accumulation of molecules in that area (Figure 4.6(a) inset). Therefore, it can be concluded from these calculations that the effect of the electrodiffusion is not significant. We then proceed to experiments, where we have measured the fluorescence and lifetime of the target biomarker molecules.

4.3. Results and discussion

To experimentally demonstrate how will the integration of DEP and plasmonic effects enhance the detection of biomarker molecules, we have used fluorescently labeled Avidin

molecules (size: 68 kDa; ex: 500 nm, em: 515 nm; suspended in a buffer that has a conductivity of 0.03S/m; Vector laboratories Inc, Burlingame, CA,) as the molecules of interest. Published literature reports have used similar molecules such as BSA and IgG molecules to show their proof of concepts [119]. Published reports that utilize only plasmonic effects have reported detecting about 1μM [119]. To demonstrate the quantification of low concentrations of Avidin molecules, we have used ~ 1pM Avidin molecules in our experiments. To find the optimum frequency of the electric field (positive DEP force) that can quickly bring molecules and place in hotspots, we varied the frequency from 50 kHz-500 kHz and measured the number of Avidin molecules collected near the electrodes. Briefly, for each frequency, we recorded a fluorescence picture of the electrodes with molecules and measured the fluorescence intensity at the periphery of electrodes. We then choose the frequency that generated the highest fluorescence (120 kHz). We used this frequency for the experiments involving Avidin molecules. In experiments, briefly, we pipetted 150 pM Avidin molecules onto PIDEs and electric field (10Vpp with 120 kHz) was applied to the terminals A and B (Figure 4.1(a)) to concentrate Avidin molecules on the hotspots. The electric field was kept on (active) for approximately 5 minutes to positive DEP to place molecules in the hotspots. We then turned off the electric field and imaged the PIDEs using a low-power fluorescent microscope and recorded the fluorescence image (inset of Figure 4.6(a)). We have turned off the electric field to avoid any interference from the electric field during fluorescence microscopy. After turning off the electric field, we have recorded a fluorescence image instantly (<5 seconds). Since the DEP off time is very short, Avidin molecules did not move away from hotspots during the fluorescence measurements. Further, we have also noticed that the Avidin molecules that are extracted by positive DEP near the electrodes do not scatter out immediately after turning off the DEP force. To compare the effects of DEP concentrating

biomarker molecules in hotspots, we have performed another experiment using another PIDE array without applying DEP. Finally, using a custom made software program, we have extracted the fluorescent intensity of each pixel of each image and plotted for comparison. The Figure 4.6(a) illustrates the fluorescence intensity vs. the number of pixels for the two experiments discussed above. By simple comparison, we can conclude that there is a large-number of bright pixels in the sample with DEP (plotted in green) when compared with the same sample that had no DEP (plotted in red). Therefore, we have assumed that DEP effectively concentrated the biomarkers on the hotspots and biomarker molecules in the hotspots are subjected to plasmonic effects and produce high fluorescence signal. Further, in Figure 4.6(a), we indicate the pixels, where there are no plasmonic effects as well as there are significant plasmonic effects. If DEP place molecules in the hotspots, those molecules must have a significant reduction on the fluorescence lifetime. To experimentally show this, we used fluorescence lifetime spectroscopy. The purpose of measuring the lifetime is based on the hypothesis that the biomarkers in the hotspots will have a significantly shorter fluorescence lifetime than the biomarkers that are not under the influence of the plasmonic effect. There are number of methods available for measuring fluorescence lifetimes [158]. Time-correlated single photon counting (TCSPC) is commonly used in many applications in which exponential decay of fluorescence light intensity is measured and used to calculate the lifetimes [158]. The detailed procedure for calculating the lifetime of a sample is published elsewhere [158]. To measure the lifetimes of molecules that are placed in the hotspots, we have used 150 nM, Tetramethylrhodamine (TRITC) labeled streptavidin molecules (ProteinMods, Madison, WI).

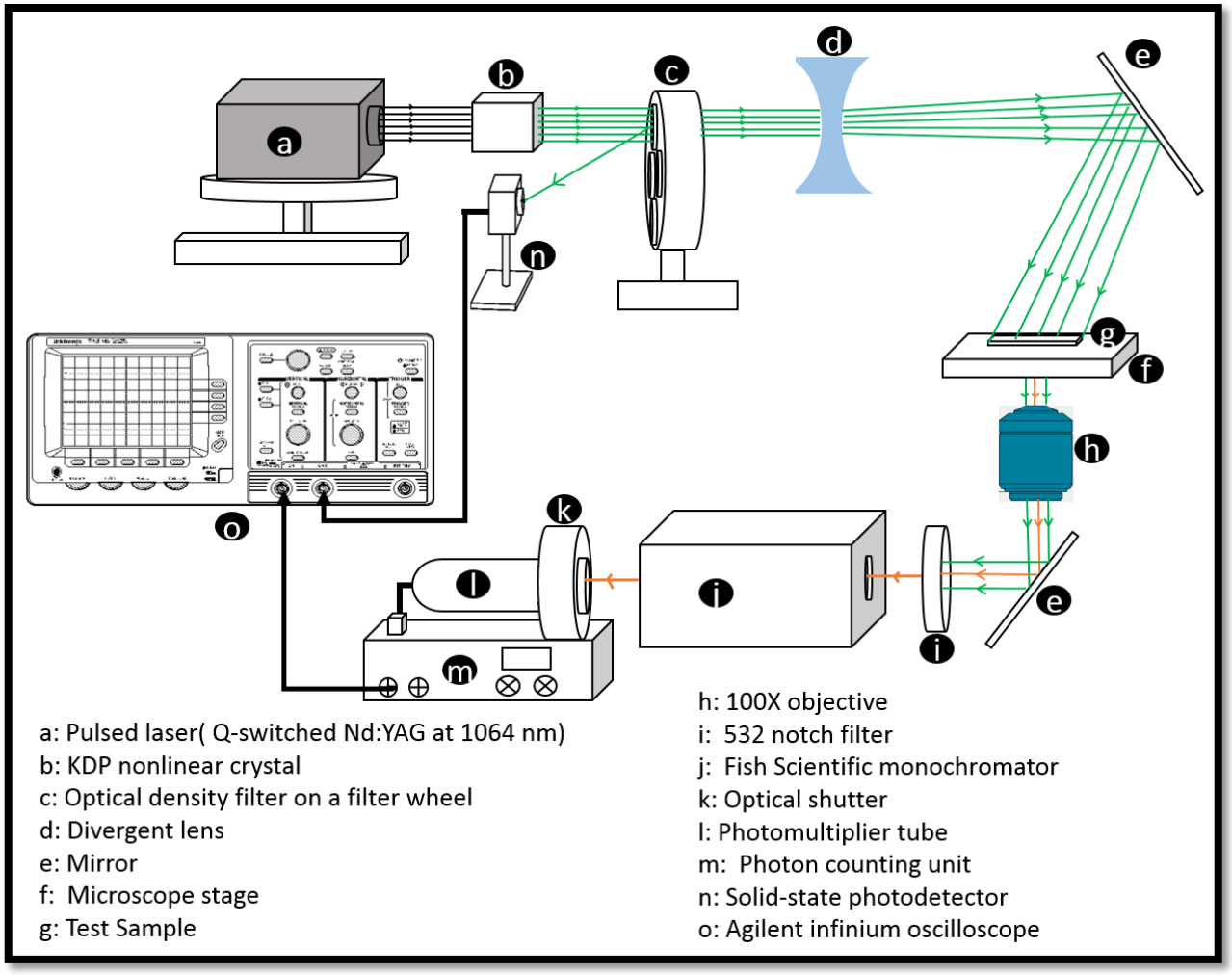

Figure 4.5: Fluorescence lifetime measurement setup.

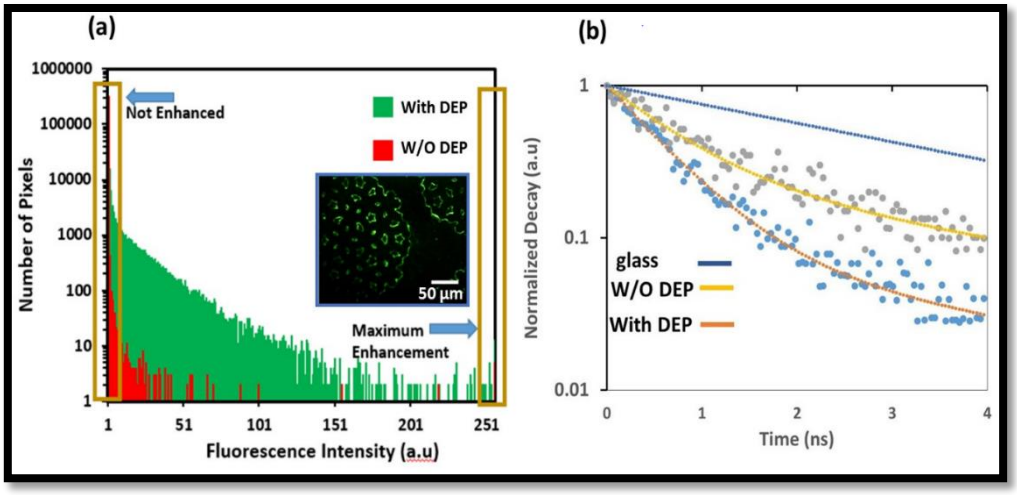

Figure 4.6: The comparison and contrast of the effects of DEP in quantifying molecules using surface plasmonic effects. **(a)** Comparison of the fluorescence measured from a sample with and without DEP. Note that sample with DEP concentrate the Avidin molecules near the electrode edges and increase the fluorescence. Similarly, sample that has no DEP, randomly scatter the molecules. Inset shows the picture of the sample with DEP used to generate the above plot. Further, we indicate the pixels where there are no plasmonic effects as well as there are significant plasmonic effects. **(b)** Fluorescence decay curves for the TRITC labeled biotin molecules in glass coverslip, on electrodes with DEP and on electrodes without DEP. These decay curves were used to calculate the lifetimes of the molecules in each case.

The selection of TRIC labeled streptavidin molecules is based on the optical capabilities that we had in the lab. We measured the fluorescence lifetime of streptavidin TRITC using TCSPC system that we designed and assembled in the lab. The detailed illustration of the experimental set-up is included in the Figure 4.5. Briefly, our TCSPC system consists of following parts: A Teem Photonics Microchip NanoPulse NP-10820-100 Nd:YAG laser at 1064 nm with 590 ps of pulse duration, 10 µJ of energy per pulse, and 6.9 kHz of pulse-repetition rate, a KDP nonlinear crystalto convert the laser output to 532 nm through second harmonic generation, a Zeiss Axiovert 40 C microscope with an 100× objective, an Ocean Optics 532 nm notch filter, a Fisher Scientific monochromator tuned at 572 nm with an full-width at half maximum bandwidth of 8 nm, a Hamamatsu photomultiplier tube R7207-01 powered by an 800 V source, a Hamamatsu photon counting unit C6465, an Agilent infinium54853A DSO

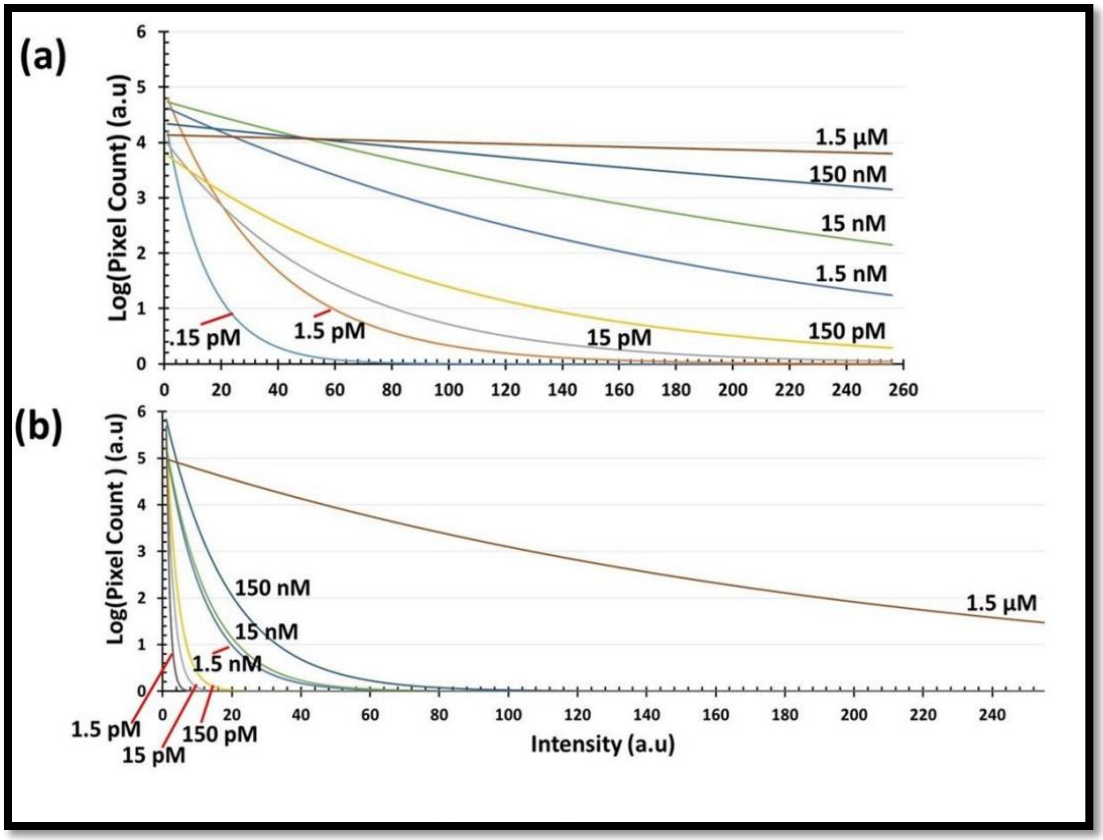

Figure 4.7: **Comparison of integrated dielectrophoretic and plasmonic based detection with standard fluorescence based detection**. Variation of fluorescence versus molarity of the Avidin molecules (a) integrated DEP and plasmonic based detection (b) standard fluorescence based detection.

oscilloscope with 20 Gsa/s, and a photodiode Electro-Optics ET-2040.In experiments, we have suspended the TRITC labeled streptavidin molecules in 0.01X phosphate buffered saline (PBS) buffer and pipetted about 100 µL of streptavidin over the electrodes and applied an external electric field (using electric potential of 10Vpp and 400 kHz) and placed the molecules on the hotspots. As before, we applied the electric field and left it on for 5 minutes for fluorescent molecules to experience DEP and move to hotspots. The selection of frequency (400 kHz) and voltage (10 Vpp) was chosen to generate the highest DEP force on TRITC molecules. To find the frequency and voltage, we started with 120 kHz and 10Vpp and gradually increase the frequency and voltage and observed the motion of TRITC molecules. At 400 kHz and 10 Vpp,

these molecules experience the largest positive DEP force. We then turned off the DEP and measured the photons that emits from the sample with time. These values are represented as points in the Figure 4.6(b). Finally, using the photon vs. time, we calculated the fluorescence decay of TRITC labeled streptavidin with time. Finally, we used the least squares algorithm to calculate the amplitude and the decay coefficient of the two exponential components of the fluorescence decay of TRITC that best fit the data obtained with our TCSPC system in samples that have the metal-glass interface without DEP, and the metal-glass interface with DEP. The only difference between these two samples was the DEP and all other experimental parameters kept unchanged. The goodness of each fit was calculated using R-square and values were 0.976 and .979 for the sample with DEP and without DEP respectively. The equations with the respective coefficients in the metal-glass interface are:

$$I_{wDEP}(t) = 0.92e^{-1.67t} + 0.08e^{-0.25t},\ I_{w/oDEP}(t) = 0.75e^{-1.38t} + 0.25e^{-0.24t}. \quad (4.3)$$

The Equations ($I_{w/oDEP}$ and I_{wDEP} the denote fluorescence intensity without and with DEP respectively) in (4) are plotted in Figure 4.6(b). The second exponential component in both equations has a decay coefficient (0.25 and .24) whose inverse is consistent with the reported fluorescence lifetime of conjugated TRITC [158]. The first exponential component in both equations had decay coefficients (1.67 and 1.38) whose inverse is close to the duration of the pulses from the Q-switched laser. Previous studies indicated that the fast exponential decay, which is due to the surface plasmonic effect [158]. The lifetime of the sample that underwent positive DEP is $\left(\frac{1}{1.67} = 0.6\right)$ is 0.6 nanoseconds and the lifetime of the sample without positive DEP is $\left(\frac{1}{1.38} = 0.72\right)$ is 0.72 nanoseconds. This reduction in lifetime is due to the DEP concentrating streptavidin molecules in the hotspots. Furthermore, our laser that we used in the

lifetime studies were a pulsed laser with pulse duration of 0.56 nanoseconds of full-width at half-maximum. Therefore, we will not be able to record the lifetimes that are smaller than the 0.56 nanoseconds. The purpose of the lifetime experiments was to demonstrate that the sample that underwent positive DEP would have reduction in lifetime when it compares it to the sample that did not undergo DEP.

Finally, we have varied the molarity of Avidin molecules from 1.5µM to 150 fM and recorded an image for each molarity. We then plotted the variation of fluorescence intensity versus number of pixels. We have included the plot in the Figure 4.7(a). We then assumed that fluorescence intensities that are above 80 are significant and above the white noise level. According to this criteria, our integrated dielectrophoretic and plasmonics based technique is capable of detecting about 1.5pM of Avidin molecules.

To compare results and find the improvement in the detection, we have used standard fluorescence technique and repeated the experiments. Briefly, we have pipetted about 100 µL of Avidin molecules (we varied molarities from 1.5µM to 15 fM) and recorded a fluorescence image of the sample for each molarity. We then plotted the variation of fluorescence intensity versus number of pixels for each molarity. Results are included in the Figure 4.7(b). We then assumed that fluorescence intensity that are above 80 is valid intensity that are above the white noise level. According our assumption, 1.5µM is the smallest molarity that can be measured using the standard fluorescence. Therefore, by simple comparison (1.5µM/1.5pM=1,000,000–fold) our integrated dielectrophoretic and plasmonics based technique enhance the detection of Avidin molecules by about million fold.

4.4. Conclusions

In summary, we have demonstrated the successful integration of our PIDEs with plasmonic hotspots for the detection of biomarker molecules. We have then experimentally showed that the positive DEP is, indeed, efficiently bringing biomarker molecules and placing them in plasmonic hotspots. Finally, we experimentally measured a reduction of the fluorescence lifetime of the molecules that are placed in the electrodes. The observed reduction in lifetime of molecules is a direct result of the molecular interaction with enhanced electric fields in the hotspots and/or surface plasmon polaritons (SPPs). However, SPPs decay with the square of the electric field and therefore SPP effects will be limited the smaller quantify of molecules that are near the electrode-glass interface. In contrast, we believe that molecular interactions with enhanced electric fields in hotspots do not dependent on the proximity to the electrodes and therefore it will provide significant contribution to the measured reduction of fluorescence lifetime. These effects combined contributed to the observed million-fold improvement of the current detection limit. Further, in this work, we did not decouple these two effects to find out the contribution of each phenomenon. The main purpose it is to demonstrate the employment of DEP in placing molecules in strategic locations so that they will be subjected to plasmonic effects (SPPs or interacting with high electric fields in the hotspots). Finally, with few more modifications, this technology can be translated into equipment for detecting and quantifying disease related molecules in real biological samples at point-of-care settings.

After successful development of this technique, we performed some studies with miRNA biomarkers because studies have shown those miRNA biomarkers are available in the serum sample at low concentrations in early stage cancer patients. Successful use of miRNAs in early cancer diagnosis mainly relies on the ability of accurately quantifying the level of them in the

patient's sample. We have developed a new technique based on the DEP and plasmonic enhancement to quantify the disease related miRNA molecules with low cost, high sensitivity and high throughput. The developed technique was discussed in the chapter 5.

CHAPTER 5. ILLUMINATE-MIRNA: PARADIGM FOR MIRNA DETECTION IN SERUM SAMPLES AT POINT-OF-CARE SETTINGS

5.1. Introduction

Pancreatic cancer (PC) is one of the most lethal cancers and a major unsolved US health problem [159]. About 6% of PC patients in US live less than five years after initial diagnosis [159]. This is in part due to the lack of a standard diagnostic tool for early detection of PC [159]. However, if this cancer were detected early and treated with existing therapy, the five-year survival rate could be 60%-100% (that is, an over ten-fold improvement). Therefore, there is an urgent need for an early detection test [159]–[161]. Early detection of PC involves first-use clinical risk factors (e.g., family history, age, and smoking) for identifying at-risk individuals [159]. The next step is the screening to monitor the development of PC and to determine the starting point of diagnosis and treatments [159]. There are multiple diagnostic options available for PC, including CT, MRI, and endoscopic ultrasound [159]. These modalities do not have sufficient resolution or sensitivity to be useful in the screening stage as they produce very high false-positive rates (> 90%) in screening [27],[159]. They therefore, are not recommended for frequent use in screening [27],[159]. Due to the lack of sensitivity and specificity, usage of current biomarkers (e.g.: CA-19-9) is limited only to the prognosis analysis. A growing body of knowledge suggests that a potential microRNA (miRNA) biomarker panel in serum (miR-642b,

---

This chapter was extracted from a published article in Journal of Physics D (Velmanickam L., Bains M., Fondakowski M., Dorsam G.P. and Nawarathna D., "iLluminate-miRNA: Paradigm for high-throughput, low-cost, and sensitive miRNA detection in serum samples at point-of-care." Journal of Physics D: Applied Physics, 2018. Doi: 10.1088/1361-6463/aaed97). Velmanickam L. had primary responsibility for simulation, calculation, sample preparation and experiments. Bains M. had primary responsibility for isolation and qRTPCR experiments. Fondakowski M. had primary responsibility for analysis. Dorsam G.P. had primary responsibility for biological related experiments and calculation. Velmanickam L., Nawarathna D., Dorsam G.P. and Bains M. also drafted and revised all versions of this chapter. Nawarathna D. served as proofreader and checked the simulations, calculations, and results of the experiments conducted by Velmanickam L.

miR-885-5p, and miR-22) can differentiate healthy individuals, PC patients, and individuals in the early stage of PC development [27]. These biomarkers, in combination, represent a new avenue for the development of a clinically useful screening test.

Cellular responses to lifestyle, stress, drugs, physio pathological conditions and pharmacological interventions have an impact on the epigenetic code, often resulting in modulation in methylome, miRNA expression, and covalent histone modifications [162]–[166]. Since epigenetic changes are taking place first in the biochemical cascade, epigenetic biomarkers could provide reliable and clinically important information, earlier than, and superior to, the downstream proteomic biomarkers [167]. It has been shown that miRNA— small non-coding RNA molecules, involve in many major cellular functions such as development, differentiation, growth, and metabolism [168]. In addition, miRNA are stably expressed in circulating blood and therefore potential candidates for health monitoring and diagnostics/screening tests [168]. As stated above, recent studies have identified unique miRNA signatures produced during the early stages of PC and treatment of OUD, as well as in response to obesity interventions [27],[169],[170]. These signatures therefore could be utilized as potential biomarkers for combating those diseases/disorders. Despite great progress in miRNA research, miRNAs have not yet been translated or used in the clinical diagnosis of any disease.

This lack of progress is partially due to the differences among and limitations of various detection technologies, which produce inconsistent results [171]. The current methods available for miRNA detection, such as qRT-qPCR, next generation sequencing (NGS), microarray-, electrochemical-, plasmonic-, and hybridization-based miRNA sensors are not suitable for clinical screening applications. These methods do not provide absolute molarity of target miRNAs (e.g., RT-qPCR, LAMP, microarray), are inefficient for short miRNAs (e.g.: NGS, RT-

qPCR), have longer pre-processing times (e.g., microarray, electrochemical, hybridization methods), insufficient sensitivity (e.g., RT-qPCR, microarray), and low dynamic range (plasmonic, electrochemical), as well as being expensive (all) [171]–[174].

Fundamentally, nearly all-current detection methods rely on non-specific, time-dependent, and unsteady molecular diffusion for critical target-probe hybridization, causing significant variation in results [39]–[41]. Additionally, molecular crowding near detection electrodes or substrates produces steric hindrance [39]. These issues affect the sensitivity, limit of detection, and speed of detection, especially, in the detection of minute amounts (< 1%) of target miRNAs from a larger background [39]. To minimize molecular crowding, a significant dilution of serum is needed. However, a diluted serum sample (from μLs serum) is insufficient to identify miRNA signatures that are clinically important [39]–[45].

Another critical issue to overcome is the hemolysis—lysis of red blood cells during the long pre-processing time. Since some of the disease-related miRNAs are involved in the normal function of circulatory and immune systems, hemolysis could artificially increases the miRNA levels and produce inaccurate results. For example, according to reports in the literature, in tumor-associated circulating miRNAs, 58% are highly expressed in blood cells, and hemolysis alters circulating miRNA levels by about 50-fold. To minimize the hemolysis, it has been shown that a sample needs to be analyzed within 30 minutes after collection, but current pre-processing time > 4 h. Since screening or diagnosis generally depends on a single sample, this critical issue needs to be solved immediately. One way to address this issue is to introduce a rapid miRNA analysis, ideally, at point-of-care settings [175]–[177]. If these critical technical issues are solved miRNA, will be the newest pillar of medical diagnostics.

5.2. Integration of fluorescence enhancement with dielectrophoresis for miRNA detection

Studies have shown that energy transfer from fluorophores to metal quench the fluorescence (from the fluorescence theory section; mechanism (a), page: 21), which is effective for the fluorophores that are located within about 5 nm from the metal edges of hotspots [126],[178]. When DEP is used to concentrate molecules in hotspots, fluorophore-labeled miRNA molecules are fully stretched by the high-electric fields in the hotspots. Therefore, miRNA molecules will form rod-like shapes that are about 8 nm long (each base pair is about 4 Å long) and 2 nm in diameter. When the miRNA molecule experiences DEP, it rotates such that the dipole along the longest non-dispersed axis aligns with the field [178],[179]. Therefore, the long axis of the rod will be aligned with the field [178].

The dipole moment of miRNA molecules are about 10 times larger than typical fluorophores (e.g., fluorescein and cyanine 3 (Cy3)) we use in experiments [178],[180]. Therefore, miRNA molecules have about 10-times larger polarizability (α) than fluorophores [143]. Since the polarizability is directly proportional to the dielectrophoretic force, miRNA molecules experience larger dielectrophoretic force than fluorophore molecules. Therefore, the miRNA portion is attracted to the region with the largest electric field gradient ($\nabla(E^2)$). Since the largest electric field gradient is produced near the electrodes, miRNA molecules will be located closer to the metal edges of the hotspots [143]. As a result, fluorophore molecules will be located about 8 nm from the metal edges. As a result, the introduction of DEP aligns the fluorophore molecules outside the active region of fluorophore quenching. This ability is highly significant for detecting low miRNA concentrations.

The fluorescence enhancement expected from increasing the radiative decay rate (from the fluorescence theory section; mechanism (b), page: 22) is highly dependent on the ability to

orient the fluorophore dipole with the plasmonic axis of the hotspots and subsequently place the molecules in the area that has large amount of surface plasmons [124],[126]. When DEP is used to concentrate the fluorophore-labeled miRNA molecules, the electric field gradient and electric polarization produced by the external electric potential on the molecules is used [143]. In electrode mode, gold nanostructures is approximated as a dipole [181]. Therefore, the highest electric field and the field gradient will be produced along the dipole axis [182]. Typically, this dipole is formed in the sharp edges of the nanostructures [143]. As a result, fluorophore-labeled miRNA molecules will be aligned along the electric dipole axis. In plasmonic mode, even though the frequency values are different, a plasmonic dipole is also produced in the same locations as the electric dipole. Therefore, when DEP is used to concentrate fluorophore molecules, fluorophore dipole of each molecule is automatically aligned with the plasmonic dipole axis of the hotspots. This is a critically important in enhancing fluorescence because studies have shown that well-aligned fluorophores with the plasmonic axis could enhance the fluorescence by up to few thousand times. In addition, DEP can be used to vary the fluorophore-metal distance to concentrate the fluorophores in the high surface plasmonic region. Briefly, first, attractive DEP concentrate molecules near the metal edges of the electrodes and apply repulsive DEP to push the concentrated molecules away from the electrode-edges to the lowest field gradient region [54],[183]. One record fluorescence intensity of the sample as the molecules are being pushed from metals edges. Finally, the distance that produces the largest fluorescence intensity can be found. The two effects that are related to mechanism (b) combine to produce about 10^5 times enhancement of fluorescence.

The contribution from mechanism (c) (from the fluorescence theory section, page: 22) depends on the ability of concentrating the fluorophores in an area where there is a large electric

field produced by scattered light near the hotspots [122],[184]. Since sizes of the nano-structures are below 100 nm, significantly large electric field distribution is expected in the hotspots. Moreover, fluorescence enhancement is proportional to the square of the electric field enhancement. To enhance the fluorescence, fluorophore labeled miRNA molecules must be placed in the region that has the largest electric field enhancement [122]. The DEP of fluorophore labeled miRNA duplexes can be used to concentrate the duplex molecules in the high electric field regions. As stated above, the distance between the fluorophore-metal edges will be altered using a combination of attractive and repulsive DEP. This effect will have a maximum of 10^4 fold enhancement of fluorescence. For these reasons, the introduction of DEP could potentially approach the theoretical limit of about one billion-fold (10^{4+5}) enhancement. In theory, billion-fold enhancement translates to increasing fluorescence intensity of one fluorophore molecule to the fluorescence intensity of billion fluorophore molecules. Therefore, the detection of just a few fluorescently labeled molecules without complicated machinery, cost, or capital will be possible. This would be ideal for the detection of early-stage diseases in point-of-care settings. Next, we will discuss a simple method that could be used to detect miRNA in point-of-care settings.

5.3. Integrated metal enhanced fluorescence and dielectrophoresis based miRNA detection

The steps of the miRNA sensing are (Figure. 5.1):

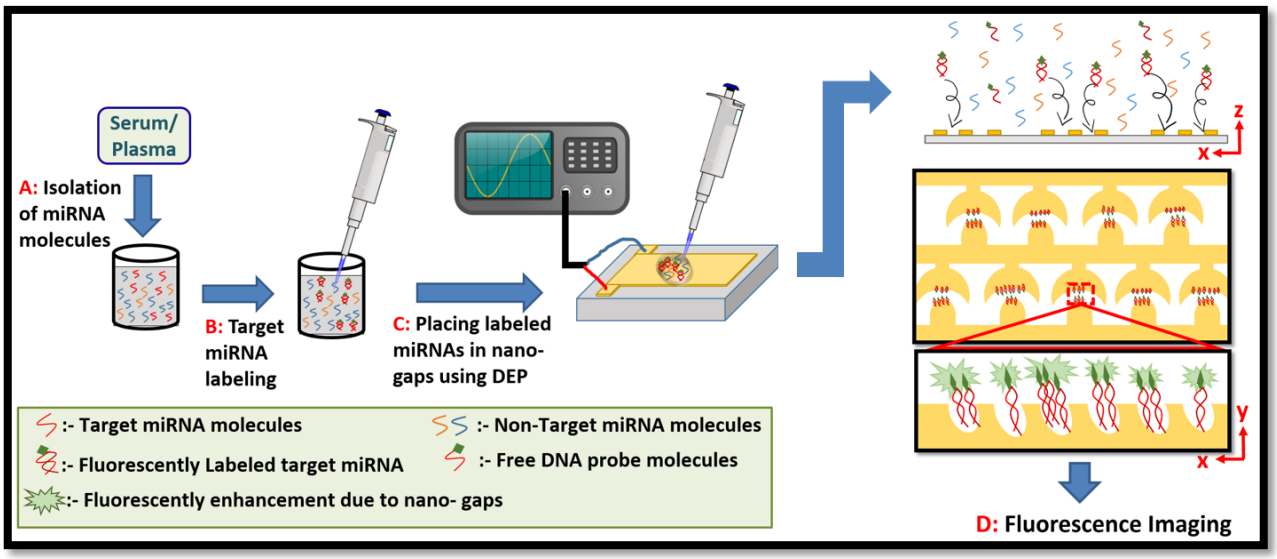

Figure 5.1: A simple miRNA sensing method that utilizes integrated dielectrophoresis and fluorescence enhancement.

Step A (miRNA isolation): Isolate miRNA (target and non-target) from the serum sample using a commercially available kit [185]. The typical isolation time is approximately 5-10 min per sample and involves using RNA-binding beads or a substrate to extract miRNA from the serum [185]. The isolated miRNA sample is suspended in TE buffer (conductivity: 5 µS/cm) for hybridization and detection. This low conductivity is needed to minimize the potentially harmful effects, such as Joule heating when apply external electric fields [186].

Step B (target miRNA labeling): Selectively hybridize target miRNA with fluorophore labeled complementary DNA molecules (95^0C for 5 minutes and cool it down in room temperature for 55 minutes) [39].

Step C (selective concentration of miRNA-DNA in hotspots for fluorescence enhancement): The sample from Step B, composed of non-target miRNA, hybridized miRNA-DNA duplexes, and free complementary DNA, will be transferred to interdigitated array of microelectrodes manufactured in gold [122]. DEP force can be used to selectively concentrate

miRNA-DNA molecules in hotspots. Then the corresponding fluorophore excitation wavelength will exposed to the concentrated miRNA-DNA molecules in hotspots for the plasmonic enhancement. Note that the hotspots are manufactured in the periphery of electrodes easy integration of dielectrophoretic concentration of miRNA-DNA duplex molecules on hotspots for the plasmonic enhancement. There are number of methods including traditional e-beam lithography and non-traditional methods to fabricate hotspots.

Step D (fluorescence imaging and detection): Finally, a simple fluorescence image of the sample will be recorded. Fluorescence intensity of the image can be calculated and molarity can be calculated using standard curve of known molarity vs. fluorescence intensity.

5.4. Materials and Methods

5.4.1. Fabrication of electrodes

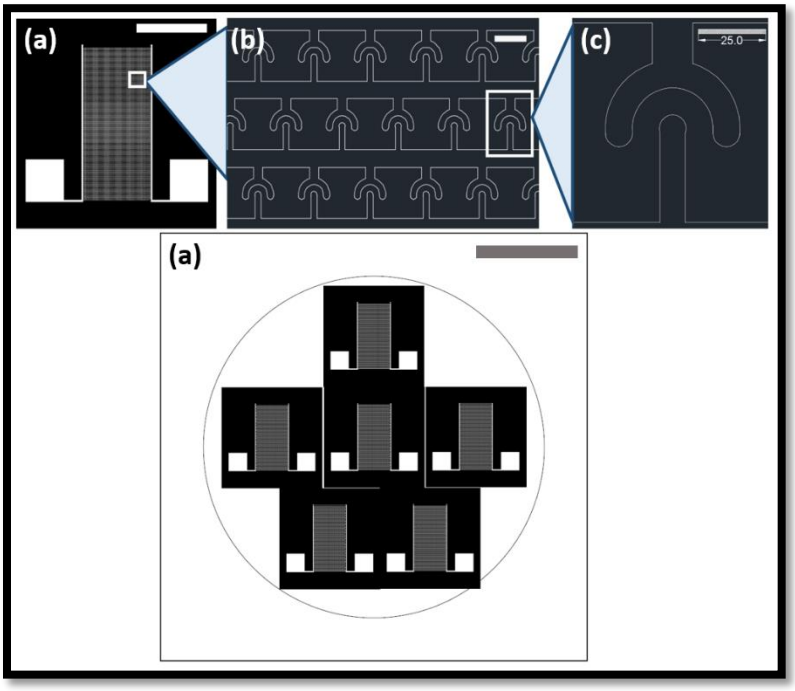

Figure 5.2: **Design and characterization of photomask**. **(a)** Designed Electrode in Auto-CAD Software ((scale bar represents 1 cm). **(b)** An enlarged section of the electrode (scale bar represents 50 µm). **(c)** Enlarged section of a T-structure (scale bar represents 25 µm), **(d)** Fabricated photomask which has six electrodes in one 4 inch glass wafer (scale bar represents 5 cm).

We have developed and utilized a T-shaped interdigitated array of microelectrodes (TIAMs) that have nano-scale plasmonic structures, called hotspots, in the periphery of TIAMs. Figure 5.3 shows the TIAMs fabricated on the glass substrate. The TIAMs were fabricated using a low-resolution photolithography mask (Figure 5.1(d)), and the photoresist film was overexposed to UV light during photolithography to produce metal structures with rough edges [54],[93]. These rough features are the nanoscale plasmonic structures (or hotspots) utilized in the miRNA detection (Figure 5.3(a-e)). To fabricate hotspots, we have developed a low-cost fabrication method that is comparable to traditional expensive E-beam lithography [93]. We have used a low-resolution photolithography (Figure 5.2(d)) mask (6200 dpc) that has intentionally

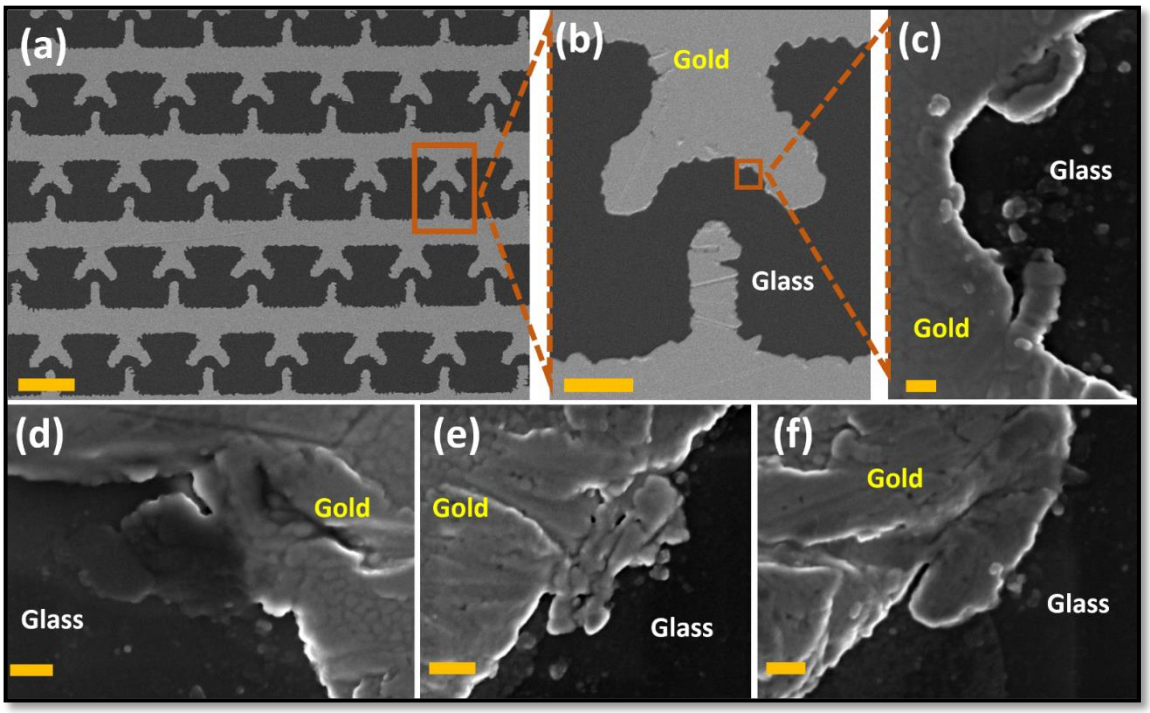

Figure 5.3: Fabrication and characterization of micro and nanostructures. **(a)** Scanning Electron Microscope (SEM) image of the fabricated electrode array (scale bar represents 50 µm). **(b)** An SEM image of a single electrode pair (scale bar represents 10 µm). **(c-f)** SEM images of nanostructures located at the periphery of the T-structure (scale bar represents 100 nm). These structures were used in integrated DEP and plasmonic enhancement studies. Scale bars are 100nm.

created rough boundaries and under-exposed photoresists films to UV light (5-s underexposure) to make structures smaller than in the photomask.

Photolithography is a process used in microfabrication to fabricate structures of a thin film of a substrate. It uses light to transfer a geometric pattern from a photomask to a light-sensitive chemical photoresist, on the substrate [187],[188]. A series of chemical treatments then etches the pattern of exposure in the material or allows the deposition of new material in the desired pattern on the material beneath the photoresist. This fabrication process contains seven major steps: Fabrication of the photomask with the design of the nano structures and the electrodes, cleaning the glass wafer (substrate) to remove the organic and in organic contaminations from it by wet chemical treatment, removal of moisture from the glass wafer by heating in an oven at 150 ^{o}C for 10 minutes, coating the photoresist by spin coating , exposure the glass wafer to light with the photomask on top of it and developing, coating of metal (gold) thin layer to the substrate and finally chemical etching to remove the uppermost layer of the substrate in the areas that are not protected by photoresist [187],[188]. To produce nanostructures, we have used a slightly modified version of the photolithography and lift off technique. Due to the photolithography fabrication process there were plenty of nano structures created at the periphery of the microelectrode array. The distribution of 100 hotspots from 8 different TIAMs we analyzed, had average size of the hotspot is about 110 nm and 99% of hotspots are between 40–150 nm.

5.4.2. Simulation

First, electrode array and the nanostructures were drawn to a scale using AutoCAD (Figure 5.2(b)) software and imported in to the COMSOL software. Then the design was extruded by 100 nm. Second the 0.01x TE buffer (5 µS/cm) was added over the electrode array and the nano

structures, which is the buffer used during the miRNA detection experiments. Third, the silica glass was placed under the electrode array and the nano structures. Then, geometry was meshed using swept mesh technique. In this swept mesh technique first we meshed the X-Y plane of the design using "Free Triangular Mesh". Then we swept the "Free Triangular Mesh" towards the Z direction of the electrode array and the nano structure. The swept mesh size was set as maximum 5nm and minimum 1nm. Since our electrode and nano structure thickness is 100 nm, this swept mesh size is more than enough to mesh the design successfully to obtain a better resolution and results.

5.4.2.1. DEP simulation

To calculate the electric field gradient $\nabla|E|^2$ inside the electrode array and the nano structures, we have used the AC/DC electric currents (ec) physics and frequency domain studies of the COMSOL software. A 10 Vp-p and 1MHz frequency sinusoidal signal was applied, the equation (5.1) was solved and the electric field strength was calculated.

$$E=-\nabla V \tag{5.1}$$

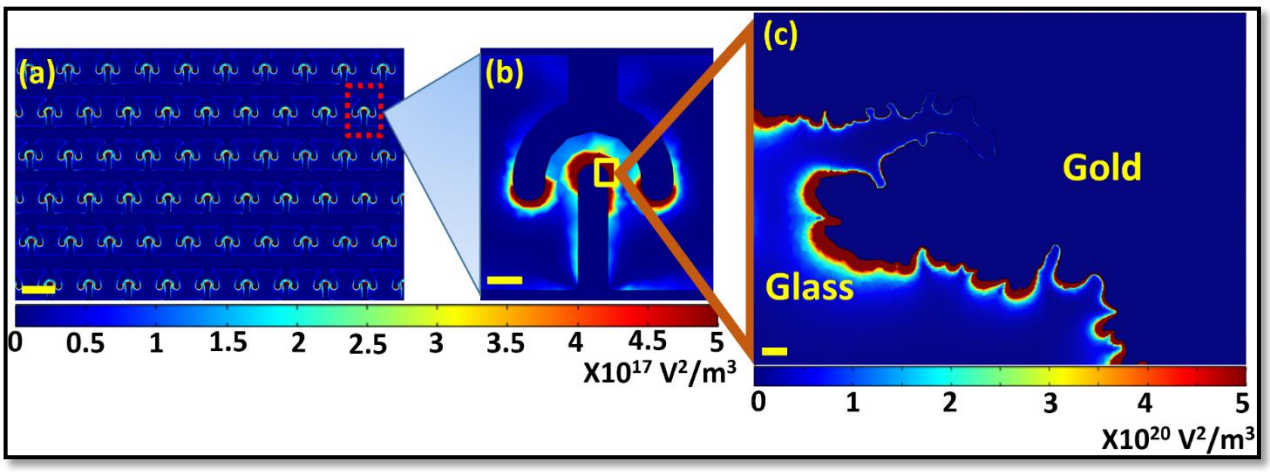

Figure 5.4: Calculated electric field gradient ($\nabla|E|^2$) in the electrode array and nano structure. **(a)** $\nabla|E|^2$ distribution in the electrode array. Scale bar is 50 µm **(b)** $\nabla|E|^2$ distribution inside a single electrode pair. Scale bar is 10 µm **(c)** $\nabla|E|^2$ distribution inside the nano structures. Scale bar is 100 nm.

where ∇ is the vector operator, E is the electric field strength in (V/m), and V is the voltage different between the electrodes. From the calculated electric field strength the electric field gradient was calculated at Z=100nm plane using the equation (5.1), because the electric field gradient is high at that plane [93].

$$G = \sqrt{\left(\frac{d(ec.normE^2)}{dx}\right)^2 + \left(\frac{d(ec.normE^2)}{dy}\right)^2} \tag{5.2}$$

5.4.2.2. Plasmonic simulation

In order to evaluate the $(\frac{E}{E_0})$, wave optics module, electromagnetic waves and frequency domain (ewfd) physics of the COMSOL software have been used to solve the traditional wave equation. If we assume the excited electric field as a planar traveling wave, the wave equation will

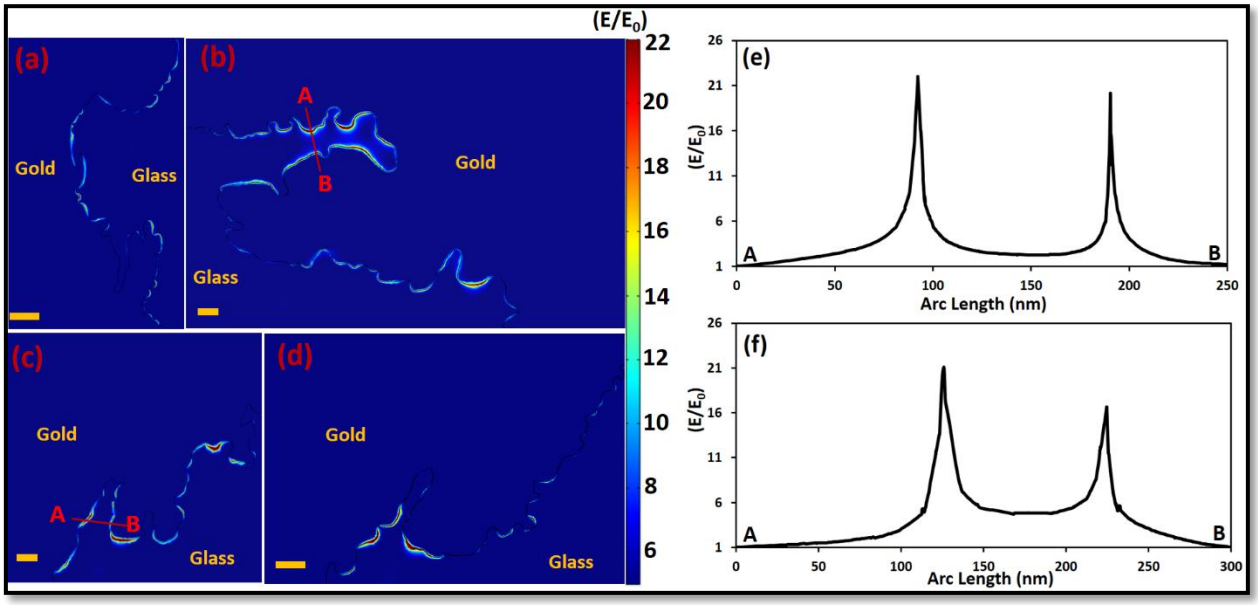

Figure 5.5: Calculated electric field enhancements due to the plasmonic effects. **(a)** Calculation of the expected electric fields enhancement $\left(\frac{E}{E_0}\right)$ of the nanostructure in Figure 5.3 (c). **(b)** Calculation of the $\left(\frac{E}{E_0}\right)$ of the nanostructure in Figure 5.3(d). **(c)** Calculation of the $\left(\frac{E}{E_0}\right)$ of the nanostructure in Figure 5.3(e). **(d)** Calculation of the $\left(\frac{E}{E_0}\right)$ of the nanostructure in Figure 5.3(f). The scale bars are 100 nm. **(e)** Calculated $\left(\frac{E}{E_0}\right)$ along the contour A-B of the Figure 5.3(b). **(f)** Calculated $\left(\frac{E}{E_0}\right)$ along the contour A-B of the Figure 5.3(c).

be converted as mentioned in equation (4.1). Then COMSOL software used to resolve equation (4.1) to evaluate the expected electric field distribution and electric field enhancement near nano structures.

The assumptions that have been taken during this simulation are hotspots were made out of Au (gold), the wavelength of transverse electric wave is 500nm and the power of the excited wave passing through the nano structures is 1mW. Since 500-nm (blue light) wavelength is close to the actual excitation wavelength that we have used in experiments, it has been selected. Finally, from the *simulation* results the incident field strength $(\frac{E}{E_0})$ was calculated at Z=100 nm plane because the electric field gradient is high at Z=100 nm plane, therefore the fluorophore labeled target bio molecules will be concentrated at that plane. We also calculated the variation of the $\left(\frac{E}{E_0}\right)$ values through the contour A-B to understand how the $\left(\frac{E}{E_0}\right)$ varies across the hotspots. The Figure 5.4 (a-c) shows the $\nabla|E|^2$ distribution inside the electrode array and the nano structures at Z=100nm plane. The Figure 5.5 (a-d) shows the calculated $(\frac{E}{E_0})$ of the different nano-structures in X-Y plane at Z=100 nm. From the simulation results, we obtained an overall distribution of $\left(\frac{E}{E_0}\right)$ value equal to 20 with maximum value of 22. Due to the shape of the nano structures and the size of the nano structures the $\left(\frac{E}{E_0}\right)$ value varies. We calculated the exact $\left(\frac{E}{E_0}\right)$ value through the cut line. The Figure 5.5 (e & f) shows the results through the cutline A-B indicates in the Figure 5.5 (b & c) respectively. Through the cutline A-B in the Figure 5.5(b & c), we have obtained the $\left(\frac{E}{E_0}\right)$ reaches the maximum value closer to the metal surface. The increase of local electric fields near hotspots helps to increase the fluorescence emission by a factor of 22^2 or nearly three folds. We also then developed a COMSOL simulation and calculated the electric

field enhancement of 40, 110 and 150 nm hotspots and obtained values of 36, 31 and 27 respectively. By comparing these values, it can be concluded that enhanced electric fields produced by these hotspots are not significantly different from each other

5.4.2.3. Joule heating simulation

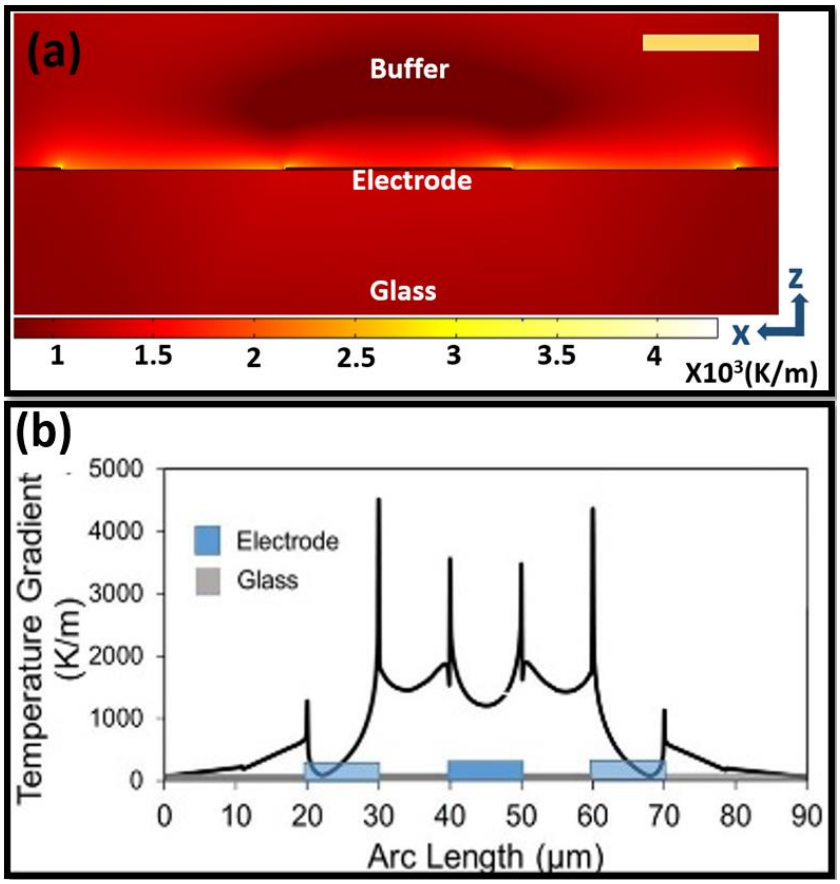

Figure 5.6: Joule heating simulation results (a) calculated temperature field gradient at 5 minutes. **(b)** Calculated temperature gradient values in the x-y plane of the TIAMs. According to our calculation, large temperature gradients (> 1000 K/m) are produced on the edges of the T-electrodes. The smallest temperature gradients (<1000 K/m) are produced on the tops of the electrodes.

To calculate the temperature and temperature gradient inside the electrode array, we have used the joule heating physics and frequency domain studies of the COMSOL software. An electric potential of 10 V_{p-p} and 1 MHz sinusoidal signal was applied to the electrode. The initial temperature was defined as 300K and the simulation was performed by varying the time (0 – 10

minutes). Lastly, the temperature and temperature gradient (∇T) were calculated from the simulation results (0 – 10 minutes). Figure 5.6 shows the temperature gradient distribution at 5 minutes and the figure shows the ∇T.

5.5. Initial experiments and results

miRNA detection with our technique is based to two hypotheses; our first hypothesis is that external alternating-current (AC) potentials produce temperatures and electric fields in biological buffers resulting in thermophoresis (or thermophoretic diffusion), diffusion and DEP (or dielectrophoretic force) on suspended macromolecules. The extent of the magnitude and direction of these interactions depends on the single versus double stranded nucleic acid structure. Therefore, specific miRNA species can be concentrated in hotspots by this technology when hybridized to a fluorescent DNA probe, due to its double-stranded nature. Our second hypothesis is that the fluorescence enhancement of oscillating dipole fluorophores will harness energy from localized electric fields from scattered light. DEP can be used to place fluorophore molecules in the areas with large localized electric fields of scattered light, resulting in a modulation of fluorescence intensity.

5.5.1. Variation of fluorescence with frequency for DNA probe and miRNA-DNA duplex

In support of our first hypothesis, we measured the fluorescence intensity variation with frequency of the electric field near a single T-electrode, between let-7b miRNA hybridized to a fluorescein-labeled DNA probe and a single-stranded let-7b DNA probe(SS-DNA). We have selected human-miR-let-7b miRNA molecules to proof the concept is working because which is highly expressed in blood/serum and has been used as a biomarker for cancer.

We purchased the fluorescein (excitation -492 nm, emission -515) nm labelled hybridized let-7b miRNA-DNA duplex molecules and the fluorescein labelled complimentary DNA molecules of let-7b miRNA (The Midland Certified Reagent Company, Midland Texas 79701, USA). First, 100nM of each miRNA-DNA and DNA sample was prepared in 0.01xTE (5µS/cm) buffer. We have selected 0.01xTE buffer because of the low conductivity and which is suitable for the DEP experiments. Second 10 µL of each sample was pipetted on the top of the TIAM electrode array and fluorescent measurements were recorded under the fluorescence microscope (XDY-1 Inverted Fluorescence Microscope, Wuzhou, Guangxi, China) varying the frequency form 0.1, 0.5, 1, 2, 3, 4 and 5 MHz with 10Vp-p. Histogram graphs and the corresponding excel files were determined from the MATLAB software. Then the total enhanced fluorescence intensity was calculated by multiplying the intensity by the corresponding pixel

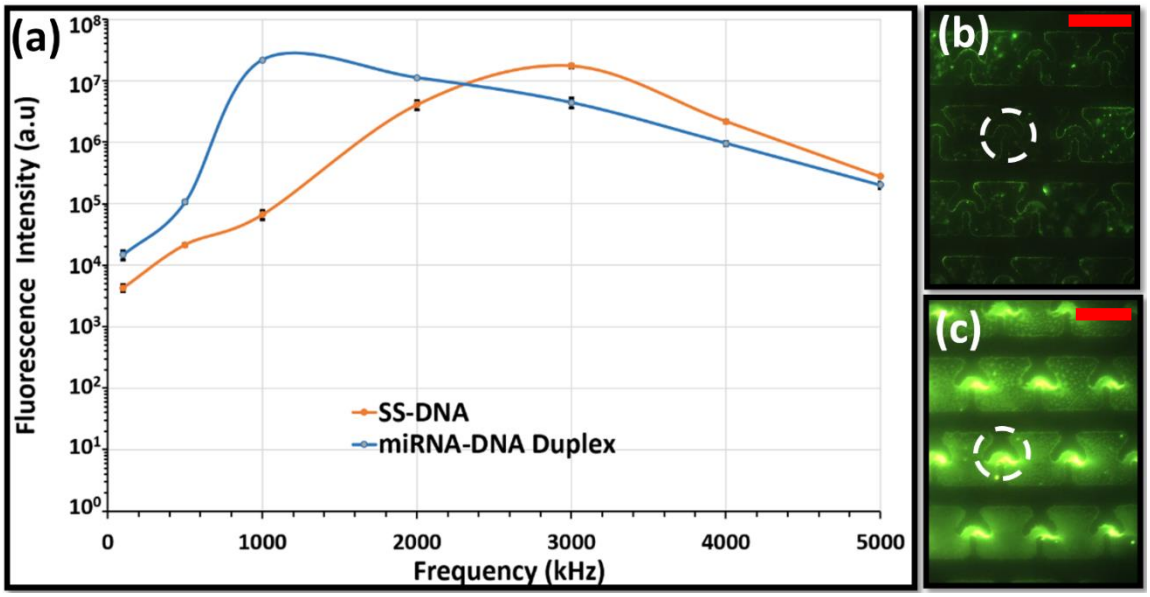

Figure 5.7: Variation of fluorescence intensity with the frequency of the applied external potential for miRNA-DNA and DNA molecules.(a) Difference in intensities between DNA probe and miRNA-DNA duplex with frequency. Note that at 1MHz miRNA-DNA can be concentrated on the hotspots without interference with probe DNA molecules. **(b)** fluorescence images of DNA probe experiment at 1MHz; **(c)** fluorescence images of miRNA-DNA duplexes experiment at 1MHz and circles with broken lines indicate the areas where combination thermophoresis, diffusion and DEP concentrate molecules. (scale bar indicates 50 µm).

values and took the sum of them. The intensities from 101 to 255 with background intensities below 100 eliminated. Total enhanced intensities were plotted with frequencies.

From the results, at 1 MHz, let-7b miRNA-DNA hybridized molecules were concentrated to a greater extent (~200x) in the T-electrodes with minimum contamination from complementary free DNA molecules (Figure 5.7). Moreover for comparison of fluorescence of miRNA-DNA at 1 MHz, we have included two fluorescence images, one of the complementary DNA probe (Figure 5.7 (b)) and one of the miRNA-DNA duplex (Figure 5.7(c)).

In addition, we have also studied the concentration of short (22 nt long) fluorescently labelled DNA molecules and DNA-DNA molecules. The experiment was conducted in the same way as mentioned above and our data indicate that DNA-DNA behave just like miRNA-DNA and concentrate at 1 MHz.

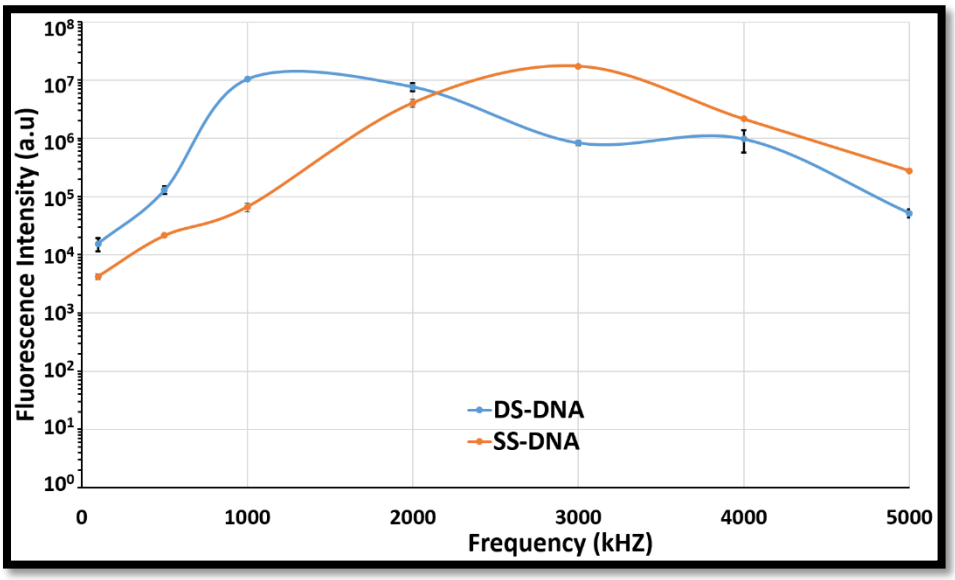

Figure 5.8: Variation of fluorescence intensity with the frequency of the applied external potential for DNA-DNA (22 nt) and DNA (22 nt) molecules. Note that at 1MHz DNA-DNA can be concentrated on the hotspots without interference with probe DNA molecules.

5.5.2. Selective concentration of miRNA-DNA duplexes in hotspots by thermophoresis, diffusion and dielectrophoresis

We then studied how the combination of thermophoresis, diffusion, and DEP produced a selective concentration of miRNA-DNA molecules in hotspots. Mathematically, thermophoretic diffusion (j), diffusion velocity (v) are represented as,

$$\vec{j} = -D_T c \nabla T - (5.3), \qquad \vec{v} = -D \nabla c \ - (5.4),$$

where D_T is the thermophoretic mobility, D is the diffusion coefficient, c is the concentration of molecules, ∇T is the temperature gradient, α is the electric polarizability of the molecule, E is the root-mean square of the electric field, and $\nabla(E^2)$ is the electric field gradient [143],[189]. Since the miRNA molecules are smaller in size the electric polarizability (α) of the molecule would be small. Therefore the only way to increase the DEP force on the smaller molecules is increase the electric field gradient ($\nabla(E^2)$). Therefore we have utilized half-circular-T-shaped TIAM electrodes because this design concentrates the electric field much better than traditional interdigitated electrodes [93]. Therefore, these T-shaped electrodes produce larger electric field gradients (10^{17} V^2/m^3 range) than other designs. Figure 5.4 shows the calculated variation of the electric field gradients in x-y plane. From this calculation, it can be concluded that the peripheries of TIAMs have nanostructures (or hotspots) with sharp nano-scale features generates electric field gradients in the range of 10^{17} V^2/m^3 range (Figure 5.4).

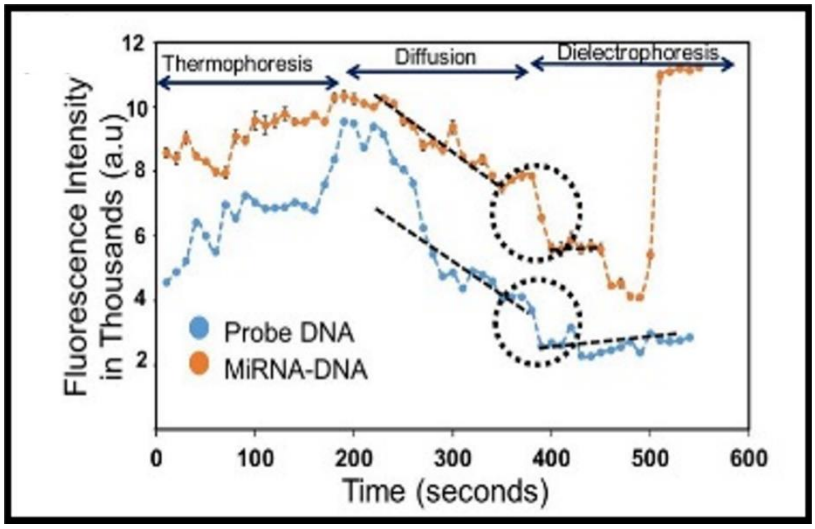

Figure 5.9: Selective concentration of miRNA-DNA duplexes in hotspots and subsequently enhancing the fluorescence. Variation of fluorescence intensity in a T-electrode with time for miRNA-DNA duplex and DNA probe molecules. Thermophoresis, diffusion and DEP were produced by applying an electric potential of 10Vpp, 1MHz. Note that at 1MHz, miRNA-DNA duplex molecules is selectively concentrated in T-electrodes.

To systematically study the concentration of miRNA-DNA molecules in hotspots, we have measured the variation of fluorescence with time for let-7b miRNA-DNA duplexes and single-stranded let-7b DNA probe, respectively (Figure 5.9). miRNA-DNA duplexes and single-stranded let-7b DNA probe were prepared in 0.01x TE buffer (5μS/cm) at 1 μM and fluorescent measurements were performed separately as indicated for each sample using a XDY-1 Inverted Fluorescence Microscope . Samples were pipetted over the TIAM electrode array and a 10 Vp-p, 1 MHz frequency sinusoidal signal was applied (t=0 second) using Tektronix AFG 3021B Single channel function generator (Beaverton, Oregon, USA). Fluorescent images were taken by a Motic 10MP camera every 10 seconds until the sample was dry (~9 minutes). Fluorescent images of TIAM electrode arrays were analyzed with Imagej software and the total fluorescence intensity (TFI) for each sample was calculated every 10 seconds. TFI was determined by multiplying the intensity (0-255) by corresponding pixel count in the histogram and taking the

sum. Finally the total intensity was plotted with time for each single stranded DNA and miRNA-DNA duplex separately.

The magnitude of the electric field (E) produced by the AC potential is in the range of 10^7 V/m, and the electric field produced an energy of ($\sigma|E^2|/2$) in the TE buffer, where σ is the conductivity of the buffer at 1 MHz [27]. This energy is partially converted to thermal energy and, as a result, the buffer solution temperature becomes slightly elevated. Studies have used very high to low conductivities (from few μS/cm to mS/cm) and DC potential or AC potentials with low frequencies (<400 Hz) in electric field mediated DNA/miRNA and DNA/DNA hybridization experiments [190]–[192]. These studies, in certain experimental conditions, have reported the generation of very high temperatures in the reaction chambers. High temperatures can potentially melt the DNA-miRNA molecules [190]–[192]. In comparison, we have used AC potential (in MHz) and low conductivity buffer (0.01xTE buffer: 5 μS/cm). Therefore, our system produces significantly lower heating and temperature increase than the published studies. We have experimentally measured a ~7°C increase in the buffer solution and in parallel, we have developed a finite element modeling simulation and calculated the spatial temperature distribution and temperature gradient (Figure 5.6) to be about 7°C and 3000 K/m (average) respectively. We do not expect a significant denaturation of miRNA-DNA duplex molecules at this temperature increase. DEP could concentrate miRNA-DNA molecules in hotspots from very beginning (t=0). However, dielectrophoretic force is a short-range force extends to about 15 μm

from electrode edges. The dielectrophoretic force is short range because electric field gradient is short range ($\nabla(E^2)$).

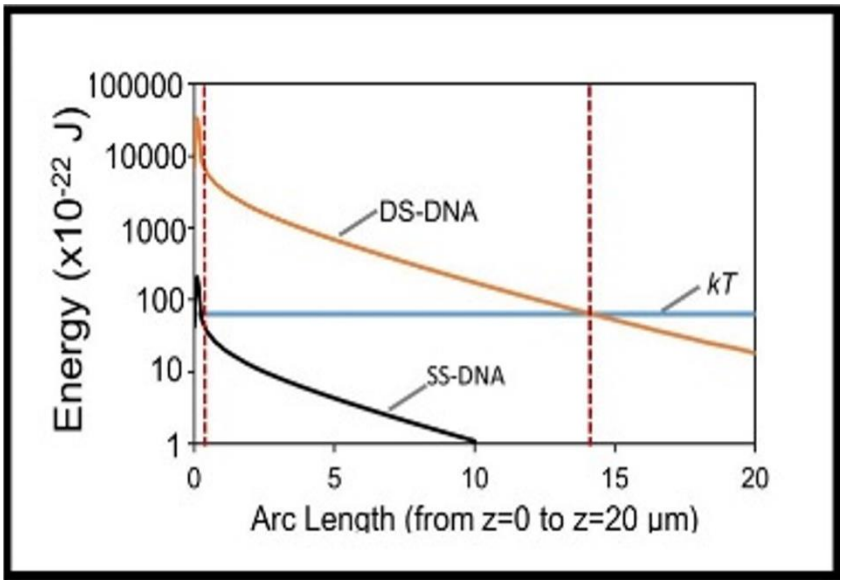

Figure 5.10: Variations of energies harnessed from electric fields and temperatures (at 1MHz) by miRNA-DNA (or double stranded DNA) and DNA with the distance from TIAM electrodes. Note that DEP produce strong and long-range dielectrophoretic force on miRNA-DNA (or double stranded DNA) molecules extending up to about 15 µm from the electrode edges. Similarly, dielectrophoretic forces produced on the DNA probe molecules are weak and short-range extending about 1 µm from the electrodes. kT represents the ground state energy of the molecule, where k is the Boltzmann constant and T is the temperature in kelvin (K).

Moreover miRNA-DNA molecules that are located within 15µm and complementary DNA molecules that are located within about 1µm from the gold electrode edges will experience the dielectrophoretic force (Figure 5.10). In comparison, thermophoresis or thermophoretic mobility and diffusion are considered as long range effects that affect molecules located up to few centimeters from the electrode edges; this is because diffusion and thermophoretic mobility are dependent $\nabla(c)$ and $\nabla(T)$ respectively.

As the buffer heats up, evaporation is increased, taking about 8 min for the buffer to evaporate. In parallel, the temperature gradient in the TE buffer results in thermophoresis (resulting in thermal diffusion) of the molecules. According to our calculations, an average

temperature gradient of ≈3000 K/m produced significant thermophoretic diffusion of the molecules (Figure 5.6). The various classes of molecules (single versus double stranded nucleic acid molecules) in the sample responded in a similar fashion by becoming concentrated near hotspots, during thermophoresis (0–200 s Figure 5.9) [193]. As molecules become concentrated in T-electrodes, molecular crowding occurs in the concentrated areas, resulting in an increase in the diffusion current that pushes molecules away from highly concentrated areas. As a result of diffusion, the fluorescence intensity near the T-electrodes gradually decreased (Figure 5.9, 200–400 s). We found that the diffusion current drives molecules to the top of the electrodes, where the thermal diffusion of molecules is relatively small. To confirm this observation, we have developed another calculation and determined the temperature gradient distribution in the x-z plane (Figure 5.6). Note that temperature gradients have minimum values over the electrodes.

These long-range forces are effective for about 300-400 seconds (after turning on the potential) and concentrate miRNA-DNA molecules very closer to electrode edges. Once miRNA-DNA molecules are closer to the electrodes, strong dielectrophoretic force (short-range force) on miRNA-DNA concentrate them in the hotspots. We have identified the time point when the DEP is activated by observing the change of slope of the fluorescence versus time curve (Figure 5.9, 300-400 seconds). Our data demonstrates that at 1MHz the increase of fluorescence of miRNA-DNA duplexes was significantly greater than the dielectrophoretic force experienced by the single-stranded DNA probe. As stated above, the single-stranded DNA probes move to the top of the electrodes by diffusion and is not detected or imaged by an inverted fluorescent microscope (see Figure 5.6).

Lastly, in support for hypothesis 1, we studied how the strength of dielectrophoretic force varies with the distance from the T-electrode. We calculated the variation of electric energy

absorbed from AC electric fields by let-7b miRNA-DNA duplexes and single-stranded let-7b DNA probes that were located along a contour in the z-direction and compared this to the thermal energy of the molecules (Figure 5.10) [143]. According to our calculation, electric energy of miRNA-DNA molecules was significantly larger than the thermal energy of the same molecules within about 10-15 μm from the electrodes. In comparison, single-stranded DNA molecules failed to be concentrated at the same distance from the electrode (10 μm). Therefore, at 1 MHz, DEP is not efficient for concentrating DNA molecules. Collectively, the above mechanism can be utilized to selectively distinguish target miRNA-DNA duplexes from free single-stranded DNA probes. We conclude that the interplay between thermophoresis and diffusion in concentrating molecules is critical to the success of our miRNA detection. In fact, diffusion is the mechanism that we used to exclude fluorophore-labeled DNA molecules from being detected.

To test hypothesis 2, we examined how hotspots scattered the excitation light and produced an enhanced electric field. The square of the electric field enhancement is the expected fluorescence enhancement [122]. According to our calculation, a maximum enhancement of about 22^2 $((E/E_o)^2)$-fold is expected from the miRNA-DNA duplexes at the top edge of the electrodes (z = 100 nm). The details of this calculation are included in the simulation results section (Figure 5.5).

5.5.3. Investigation of fluorophore quenching in our system (mechanism a: discussed in chapter 1 under fluorescence spectroscopy section)

We investigated the fluorophore quenching due to metal-fluorophore interaction. Fluorophore molecules are oscillating dipoles that can couple with surface plasmons of gold and transfer energy to gold [122]. The critical metal-fluorophore distance needed for coupling in gold

is about 5 nm or less [194]. When external electric fields or DEP are used, electric fields stretch miRNA-DNA molecules, align along the field lines, and produce electric polarizability (α) differently on miRNA-DNA and fluorophore molecules [179]. The dielectrophoretic forces on miRNA-DNA duplexes and fluorophore molecules are proportional to α values [179]. The largest positive α of miRNA-DNA molecules is about 100-times larger than that of fluorophore molecules, resulting in a stronger force (about 100×) on miRNA-DNA duplex molecules [143],[178]. Therefore, stronger dielectrophoretic force attracts miRNA-DNA duplex molecules closer to the gold edges of hotspots and keeps the fluorophore molecules about 1 length of miRNA-DNA (about 8 nm) from the metal, preventing fluorophore quenching.

To verify our speculation, we have performed two experiments and produced histogram plots for: (1) fluorophore (Fluorescein) labeled miRNA-DNA duplex molecules that are concentrated in the hotspots using dielectrophoretic force (10Vpp at 1MHz), and (2) fluorophore (Fluorescein) labeled miRNA-DNA near hotspots without dielectrophoretic concentration. If our speculation is correct, experiment (1) should produce a histogram with significantly brighter fluorescence pixels than experiment (2). This is because, in experiment (1), bright fluorophore molecules closer to gold (< 5 nm) will not be quenched. As expected, experiment (2) produced pixels that have fluorescence intensity of 50 (in a scale of 1 to 251 and 251 is the brightest pixel) or less and most number of pixels (25000) had an intensity of 11. In comparison, experiment (1) produced large number of bright pixels that are greater than 50. Moreover, largest number of pixels (7000) had an intensity of 251. These evidences show that introduction of DEP significantly minimizes or even eliminates the fluorophore quenching. At the same time, some fluorophore labeled free (not hybridized) complementary DNA may get absorbed into the gold

hotspots and quenched. We are not concerned about free complementary DNA quenching because it might indeed help in improving the purity of the miRNA-DNA sample.

5.5.4. Investigation of the ability of dielectrophoresis to concentrate fluorophores in regions where the local electric field is produced from light scattered by plasmonic structures (mechanism c: discussed in chapter 1 under fluorescence spectroscopy section)

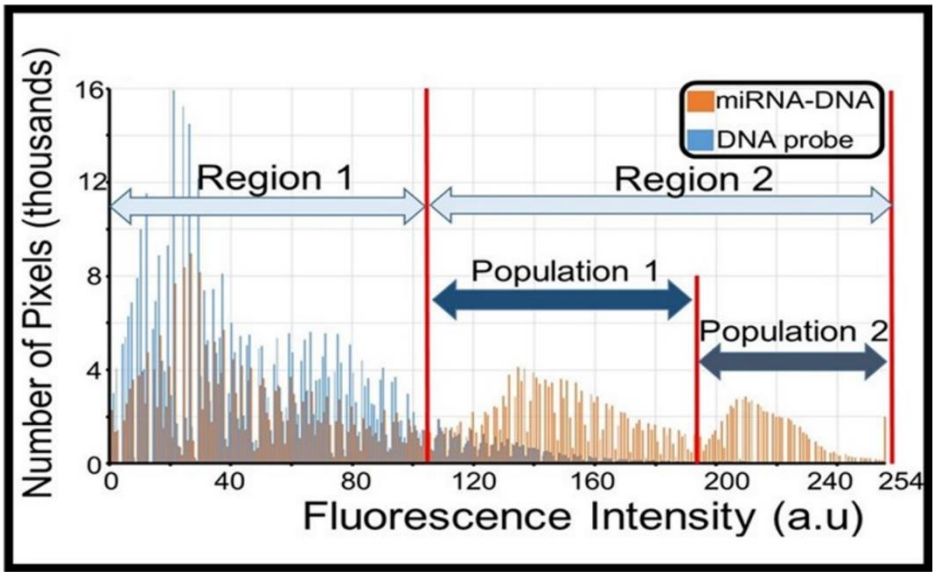

Figure 5.11: Fluorescence enhancement of miRNA-DNA duplex molecules. Comparison of fluorescence from miRNA-DNA and DNA probe molecules. These molecules were concentrated using an electric potential of $10V_{pp}$ at 1 MHz.

We tested the ability of DEP to place fluorophores in the region of a large electric field from the scattered incident light. We have used fluorescein (excitation: 490 nm, emission: 520 nm)-labeled miRNA-DNA duplexes in these experiments. Fluorescein was selected because it has a high quantum yield (~0.9) and therefore it is a stable fluorophore [122]. To produce DEP, we applied an AC electric field of 10 V_{p-p} with 1 MHz to the fluorescein-labeled miRNA-DNA duplexes, thereby concentrating the molecules to the hotspots, then recording an image. As a negative control experiment, single-stranded complementary DNA molecules (without miRNA) were concentrated with 10 V_{p-p} and 1 MHz AC potential. Exclusively using the miRNA-DNA

duplexes, we extracted the fluorescence of each pixel within each image and plotted these as histograms (number of pixels versus fluorescence intensity, Figure 5.11). By comparing the two histograms, we observed two distinct regions, named Region 1 and Region 2. Region 1 represented a low fluorescence area where DEP did not concentrate duplex molecules into hotspots. In contrast, Region 2 represented a high fluorescence area where DEP actively concentrated duplex molecules into hotspots. Within Region 2, there were two distinct fluorescence distributions. The broadly distributed population is from enhancement via larger population of hotspots (comparatively small electric field is produced by scattering light through it), and the narrowly distributed population is from enhancement via light scattering with small hotspots (large electric field is produced). Therefore, regardless of the nature of scattering, this demonstrates that DEP can be used to concentrate molecules in regions that have a large electric field from the scattered light.

5.5.5. Investigation of the ability of dielectrophoresis to aligning the fluorophore dipole with the plasmonic axis and placing the fluorophores in the high surface plasmonic region (mechanism b: discussed in chapter 1 under fluorescence spectroscopy section)

We investigated the ability of DEP to align the dipole of fluorophore molecules with the plasmonic axis and concentrate fluorophores in regions with the largest plasmonic effect. However, we did not decouple these two phenomenon.

We used low quantum yield fluorophore molecules (Cy3, Quantum yield: 0.04, lifetime: 2.3 ns excitation: 550 nm, emission: 570nm) to label the miRNA-DNA duplex molecules and investigated their lifetime (increase or decrease) when concentrated in hotspots using DEP [180]. We performed three experiments. The first measured the lifetime of molecules concentrated in hotspots using DEP. The second recorded the lifetime of molecules not concentrated with DEP.

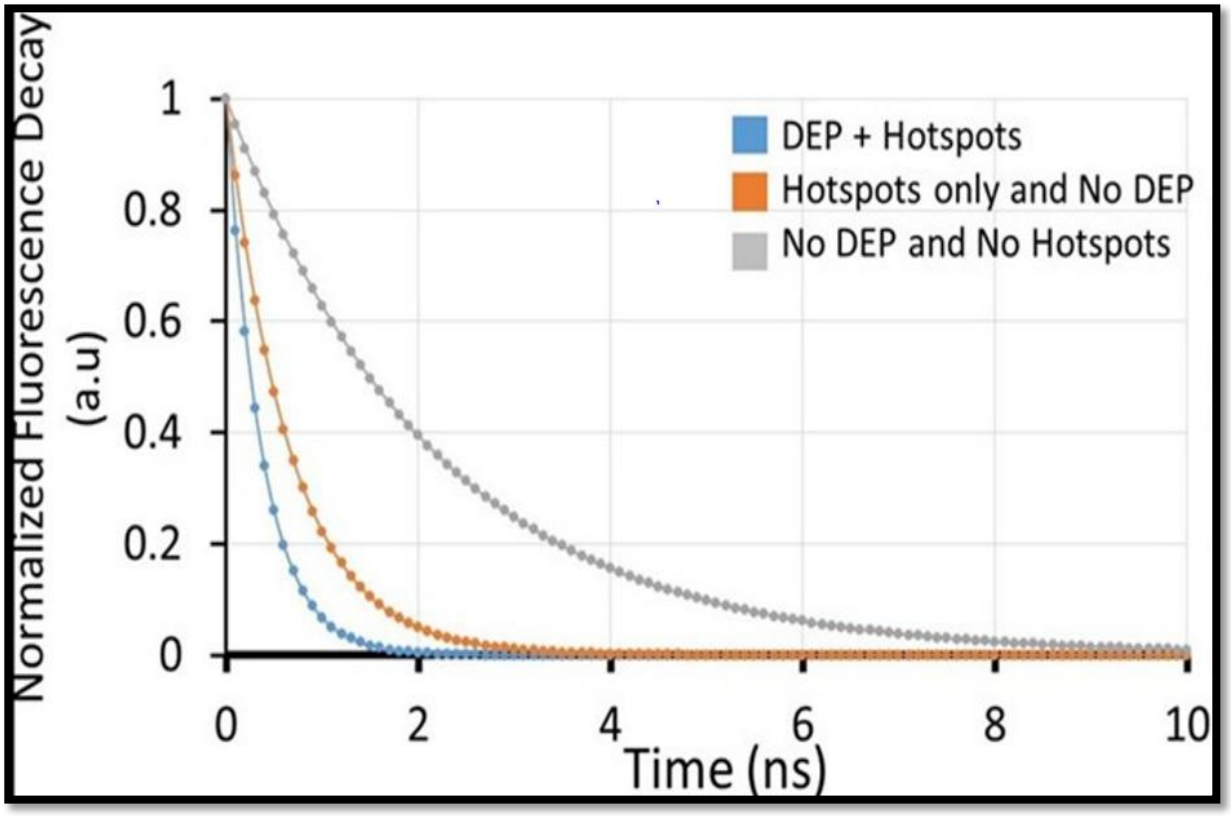

Figure 5.12: **Lifetime measurements**. Radiative decay rate increase: Fluorescence decay curves for calculating the lifetimes of *Let-7b* miRNA-DNA duplexes labeled with low quantum yield Cy3 (Q.Y.=0.04).

The third measured the lifetime of molecules deposited on glass slides (no DEP and no modulation of radiation decay rate). The experimental details and the procedure for lifetime measurements are included in the chapter 4. Figure 5.12 displays the exponential fluorescence decay curves used to calculate the lifetime of fluorophore molecules in each condition. The lifetimes were 0.3 ns, 0.7 ns, and 2.3 ns for hotspots with DEP, hotspots without DEP, and without hotspots and DEP, respectively. According to our lifetime data, the smallest lifetime (or the largest radiative decay) was measured from the molecules that was concentrated using DEP.

5.6. Proof of concept experiments and results

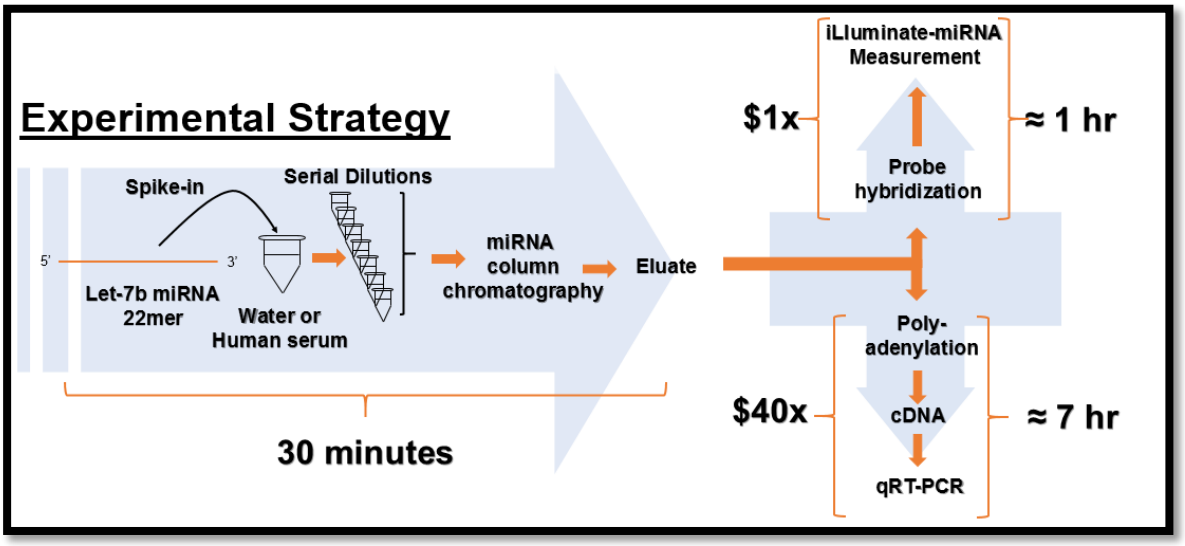

Figure 5.13: Experimental strategy for miRNA Let-7b spiked-in measurements

Next, we present proof-of-concept data showing that the iLluminate-miRNA method was able to detect Let-7b miRNA in a quantitative and specific manner. To this end, we used water and human serum solutions, which were spiked with known concentrations of Let-7b miRNA. Samples were divided equally after column chromatography, measured by the iLluminate-miRNA and compared to qRT-PCR measurements. It is worth noting the rapid measurement time and cost-effective nature of the iLluminate-miRNA method relative to qRT-PCR (Figure 5.13). In the iLluminate technique measurements, first, spiked in miRNAs were isolated using the standard protocol provided by the (SNC50 2017 Sigma-Aldrich, St. Louis, MO, USA). Then isolated Let-7b molecules were hybridized using 10 times the molar concentration of the fluorescence labelled complementary DNA probe. However, in real-world assays, the molarity of miRNA is not known, we have slightly changed this this approach. MiRNA-DNA duplexes were hybridized by heating to 95°C for 5 minutes and cooled at room temperature for one hour. Samples were pipetted over the TIAM electrode array and 10 Vp-p voltage 1 MHz frequency sinusoidal signal was applied. When samples

dried, fluorescent images were taken and effective fluorescence intensity (EFI) was calculated. The EFI was calculated by eliminating the background intensity. The background intensity was determined by repeating the experiments with the same concentration of single stranded DNA probe and the histogram was plotted from the recorded images. From the histogram, an intensity point was determined where the pixel value was zero. Then the total EFI due to the miRNA-DNA duplex was calculated by analyzing the intensity above the determined background zero intensity value. The corresponding total EFI were calculated similarly for each concentration. The qRT-PCR detection was performed by Dr. Glenn Dorsam and his student Dr. Manpreet Bains from the Department of Veterinary and Microbiological Sciences, NDSU by using Agilent kit as described by the manufacturer (600583 2017 Agilent, Santa Clara, CA, USA).

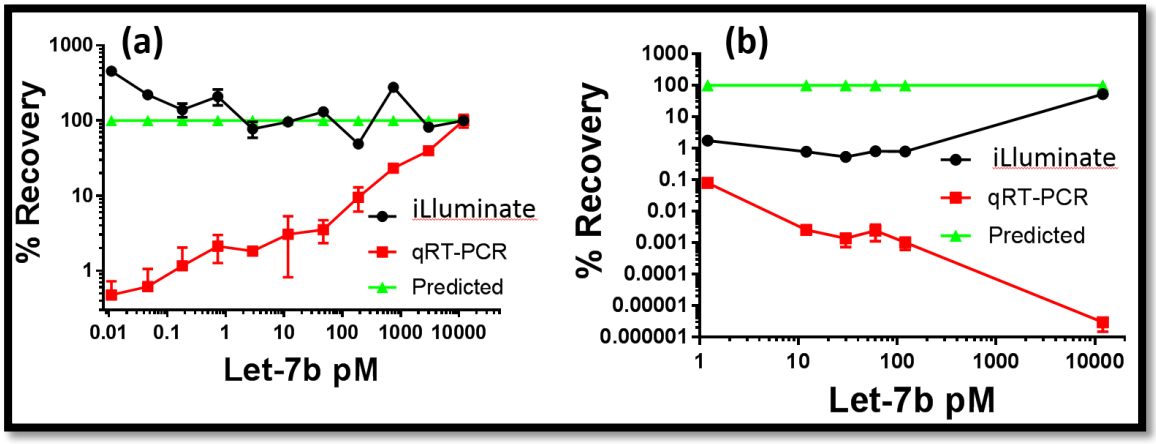

Figure 5.14: iLluminate-miRNA versus qRT-PCR comparison for miRNA Let-7b measurement. **(a)** Detection of spiked-in miRNA Let-7b in nuclease-free water **(b)** Detection of spiked-in miRNA Let-7b in human serum purified by column chromatography and measured by iLluminate-miRNA versus qRT-PCR from 3-4 independent experiments. Data is presented as line graphs with means of % recovery +/- SEM, and set arbitrarily to 100% based on the highest Let-7b concentration spiked into water (12 nM). All subsequent calculations were based on this maximum % recovery value.

From the experiment results from both the iLluminate and qRT-PCR we have determined the % recovery of each method. The method that we employed to graph data for Figure 5.14(a) is

based on the delta Ct method [195], with some modifications. Due to the fact that our proof-of-concept strategy for this study was using spiked-in amounts of known Let-7b concentrations in water or human serum, we did not have the luxury to measure a normalizing microRNA.

Table 5.1: Summary of iLluminate and qRT-PCR data from spiked-in Let-7b experiments.

Water												
	iLluminate-miRNA						***qRT-PCR***					
[Let-7b] pM	**EFI Means**	**+/- SEM**	**Predicted**	**% Recovery**	**+/- SEM**	**N**	**Ct Means**	**+/- SEM**	**Predicted**	**% Recovery**	**+/- SEM**	**N**
12000.0	75662143.0	2171322.0	100.0	100*	2.9	3	10.40	0.29	100.0	100*	43.31	3
3000.0	15425028.0	112101.7	25.0	81.55	0.15	3	13.69	0.15	25.0	10.24	59.05	3
750.0	13172686.0	124004.0	6.25	278.56	0.16	3	16.47	0.19	6.25	1.49	29.22	3
187.5	576083.7	23188.9	1.56	48.73	0.03	3	19.95	0.59	1.56	0.13	88.62	3
46.9	389066.3	4179.0	0.391	131.57	0.006	3	23.32	0.43	0.391	1.29E-02	78.11	3
11.7	70961.0	3272.0	0.098	96.19	0.004	3	26.12	0.99	0.098	1.85E-03	167.70	3
2.9	14164.0	3356.0	0.024	77.46	0.004	3	28.76	0.77	0.024	2.98E-04	139.73	3
0.73	9673.0	2290.0	0.0061	209.58	0.003	3	30.22	0.74	0.0061	1.08E-04	107.14	3
0.18	1609.0	334.0	0.0015	139.45	0.0004	3	33.71	1.14	0.0015	9.62E-06	186.21	3
0.046	638.0	78.0	0.00038	220.93	0.0001	3	36.47	1.04	0.00038	1.42E-06	150.00	3
0.011	328.0	35.0	0.00010	456.32	0.00005	3	38.75	1.17	0.00010	2.93E-07	186.21	3
0.000	0.0	0.0	0.00000	0	0	3	40.10	0.00	0.00000	1.15E-07	134.69	3

- - Arbitrarily set to 100%

Table 5.2: Summary of iLluminate and qRT-PCR data from spiked-in Let-7b experiments.

Serum												
	iLluminate-miRNA						***qRT-PCR***					
[Let-7b] pM	**EFI Means**	**+/- SEM**	**Predicted**	**% Recovery**	**+/- SEM**	**N**	**Ct Means**	**+/- SEM**	**Predicted**	**% Recovery**	**+/- SEM**	**N**
12000.0	40012795.0	954924.4	100.0	52.9	2.39	3	36.95	1.60	100.0	1.02E-06	53.97	3
120.0	5955.3	514.7	1.000	0.00787	0.09	3	38.03	2.60	1.000	4.82E-09	29.45	3
60.0	3027.0	744.0	0.500	0.00400	0.12	3	35.98	2.28	0.500	9.97E-09	5.81	3
30.0	1011.7	277.2	0.250	0.00134	0.07	3	36.98	1.99	0.250	2.49E-09	1.16	3
12.0	588.3	131.1	0.1000	0.00078	0.02	3	35.87	0.76	0.1000	2.15E-09	0.086	3
1.2	132.0	20.0	0.0100	0.00017	0.002	3	36.06	2.20	0.0100	1.89E-10	0.085	3
0.0	13.3	3.8	0.0000	0.00000	0.000	3	37.42	2.30	0.0000	0.00E+00	0.023	3

α and β – Compared to % recovery from 12 pM let-7b in water

Table 5.3: Comparison to predicted 100%% recovery. (P values calculated by One-Way A Nova)

Water			
Procedure	***% recovery mean***	***P Value***	***Significance***
qRT-PCR	15.45	0.2687	ns
iLluminate-miRNA	154.3	0.0001	****
Serum			
Procedure	***% recovery mean***	***P Value***	***Significance***
qRT-PCR	0.01052	0.0001	****
iLluminate-miRNA	8.218	0.0001	****

Therefore, we arbitrarily used the lowest cycle threshold (Ct) value for each set of data in water and serum. Each cycle in quantitative PCR represents a doubling when efficiencies are 100%, and therefore we calculated the difference in Ct for each Let-7b concentration by taking the Ct for each respective let-7b concentration and subtracted it from the lowest Ct value obtained for that solvent. This calculation generated relative Ct differences for all let-7b concentrations. Since each sample was a ¼ serial dilution starting from 12 nM, each subsequent dilution should yield a reduction of 2 Ct. To determine percent

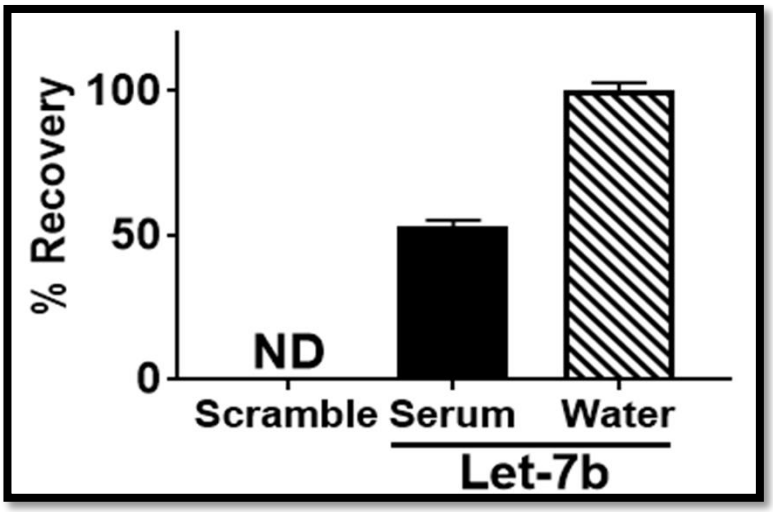

Figure 5.15: Scrambled miRNA (12 nM) or miRNA Let-7b (12 nM) were spiked into water or human serum. Samples were subsequently purified by column chromatography and measured by iLluminate-miRNA or qRT-PCR. Data is presented as a bar graph with % recovery means +/- SEM from 3 independent experiments.

recoveries, we divided the calculated change in Ct by the predicted 2 Ct change (e.g. 0.25) and multiplied by 100. For iLluminate-miRNA, % recoveries from water or serum were calculated by taking the ratio of enhanced fluorescence intensity (EFI) from each diluted sample (numerator) over the EFI for 12 nM from water (denominator) and normalized by multiplying with the dilution factor (Table 5.1). Therefore, the maximum % recovery in human serum was 52.88% (Table 5.2).

This study confirmed that both the iLluminate-miRNA method and qRT-PCR were effective at measuring purified Let-7b miRNA (range: 0.0114 pM–12 nM) spiked into water (Figure 5.14(a) and Table 5.1) or human serum (Figure 5.14(b) and Table 5.2). However, comparison of the percent recoveries of spiked-in Let-7b miRNA to a 100% predicted recovery (represented as a green line in Figures 5.14(a and b)), clearly showed that the iLluminate-miRNA method was more accurate and precise at all spiked-in Let-7b miRNA concentrations using both water and human serum as solvents. Compared to qRT-PCR, the iLluminate-miRNA method resulted in smaller standard errors of the mean (SEM) for Let-7b miRNA concentrations (Tables 5.1 and 5.2), especially in water. To ensure specificity,

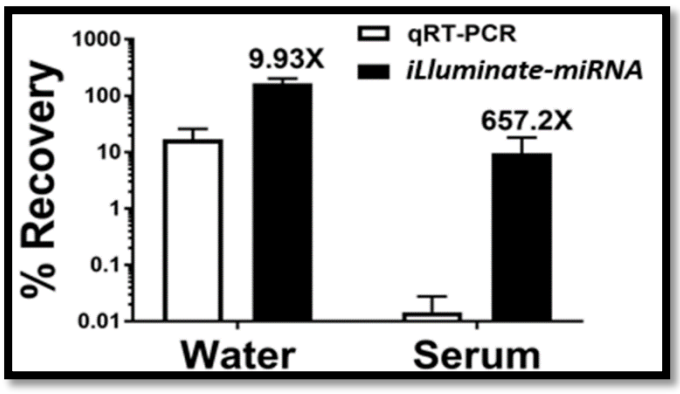

Figure 5.16: **Direct relative comparisons of % recovery calculations at 12 nM are presented in a bar graph +/- SEM from 3-4 independent experiments**. The fold-difference in % recovery value for iLluminate-miRNA versus qRT-PCR is placed above the appropriate bar for both water and human serum solvents

Figure 5.15 illustrates the detection of 12 nM of Let-7b miRNA, but not a randomly generated miRNA (22mer called scrambled – scr.), for the iLluminate-miRNA technique when spiked into water (set arbitrarily to 100%) or human serum (52%), respectively.

In this study, single base pair mismatches were attempted by using Let-7c, which differs by a single nucleotide to Let-7b. This effort yielded similar % recoveries for both Let-7b and Let-7c and could present certain drawbacks in measuring miRNA species with a high percentage of base pair similarity.

However, with respect to cancer miRNA biomarkers, such as miRNAs 642b, 885-5p and 22, do not have significant base pair similarity to other known miRNAs [27]. Therefore, we propose that our iLluminate-miRNA platform detection strategy would be effective at measuring unique miRNA species for early cancer detection. Moreover, in an effort to improve our ability to measure single base pair differences in miRNAs with our technology, we hypothesize that altering hybridization conditions will improve our technique's ability to discriminate miRNAs with a single base pair mismatch [39], The reduction in percent recovery in serum versus water for the same Let-7b miRNA (12 nM) might not be directly due to the iLluminate-miRNA detection method, but rather because of a reduction in Let-7b miRNA yield during column chromatography. Lastly, the iLluminate-miRNA method was nearly 10- and 660-fold more sensitive at detecting 12 nM spiked-in Let-7b miRNA compared to qRT-PCR in water or serum (Figure 5.16). Table 5.3 summarizes the overall means, +/- SEM and p values for the two methods. These results support our conclusion that our miRNA detection technique can successfully quantitate Let-7b miRNA molecules after purification from water or biological fluids in an inexpensive, rapid, accurate, and precise manner that outperforms the current gold-standard approach of qRT-PCR.

5.7. Discussion

In summary, we have demonstrated a proof-of-concept miRNA detection technique (iLluminate-miRNA), which could be implemented as a novel diagnostic platform in point-of-care settings. This iLluminate-miRNA detection methodology encompasses the following steps: 1. miRNA isolation from serum by column chromatography and suspension in a low conductivity Tris EDTA (TE) buffer (~5 minutes), 2. hybridization of target miRNAs with a complementary DNA probe tagged with a fluorophore to produce miRNA-DNA duplexes of target miRNA molecules (~5 minutes), and 3. the transfer of the sample (miRNA-DNA duplexes, free miRNA, and fluorophore-labeled DNA) to TIAMs for concentration, fluorescence enhancement, and molarity calculation (~8-10 minutes). Once all of these steps have been integrated into a single disposable diagnostic platform, a major future goal for our research team will be high-throughput miRNA detection with an estimated 20 min completion time at point of care facilities. For example, we expect the manufacturing cost for this disposable device, including the TIAM array and reagents will be ~$60. In parallel, Professor Nils Walter's group has reported a miRNA detection platform using kinetic fingerprinting to distinguish between nucleic acid polymorphisms [196]. At this time, the iLluminate-miRNA technique was unable to distinguish let-7c from let-7b, a difference of 1 nucleotide (data not shown). To improve the specificity of the iLluminate-miRNA technique, we intend to implement similar hybridization regiments in an attempt to optimize our miRNA detection technique as reported by Gao's group [39].

Regarding thermophoresis of miRNA-DNA duplexes and DNA molecules, a recent study by Braun's group reported that both miRNA-DNA and DNA molecules respond similarly to thermophoresis and are drawn toward the highest temperature gradient, which is near the T

electrodes (or hotspots). Indeed, increasing fluorescence from 0–200 s, our findings for both miRNA-DNA and DNA are consistent with those of Braun et al. (Figure. 5.9) [189]. Regarding reference genes for the iLluminate-miRNA detection platform, it is important to mention that we purposefully did not use an internal control, such as a different miRNA species spiked-in at a constant concentration. Inclusion of such a standard control can be implemented in the future, however, we would expect similar results as presented. A major future goal is to utilize the iLluminate-miRNA detection platform in measuring miRNA cancer biomarkers (miR-642b, miR-885-5p, and miR-22) in cancer patient serum as reported by Ganepola et al. [27]. These authors also identified a suitable internal miRNA control (miR-3196), which did not fluctuate between patients and will be utilized in future experiments [27].

CHAPTER 6. VALIDATION OF ILLUMINATE-MIRNA WITH PANCREATIC CANCER PATIENTS' PLASMA SAMPLES

6.1. Introduction

As discussed in the previous chapter 5, it have been proved that *miR-642b, miR-885-5p* and *miR-22* can be used as an effective biomarker for detecting PC at its very early stage[27]. Therefore to validate our iLluminate-miRNA technique, we conducted some clinical studies with the real cancer patient's plasma sample which were provided by the Cancer Research and Genomic Medicine, The Valley Hospital Ridgewood, NJ, USA through a collaboration. We received 12 PC patients sample and 10 healthy patients' samples for this study.

Table 6.1: Patient's sample details received from Valley Hospital. (colored boxes indicates the samples that used for the validation study)

Specimen types	Sample name	Date
PC Patient	1481	3/26/14
PC Patient	1477	3/19/14
PC Patient	1186	6/15/12
PC Patient	1227	10/26/12
PC Patient	1228	11/5/12
PC Patient	1444	12/23/13
PC Patient	1462	1/29/14
PC Patient	1783	2/4/16
PC Patient	1784	2/5/16
PC Patient	1704	7/28/15
PC Patient	1840	5/11/16
PC Patient	1857	6/29/16
Healthy Patient	C002-42m	6/11/14
Healthy Patient	HR001-36m	9/16/2014
Healthy Patient	C004-42m	6/13/2014
Healthy Patient	HR002-42m	9/12/14
Healthy Patient	HR006-42m	9/17/14
Healthy Patient	HR009-42m	9/29/14
Healthy Patient	HR007-42m	9/29/14
Healthy Patient	HR005-42m	10/1/14
Healthy Patient	HR008-42m	9/22/14
Healthy Patient	HR004-42m	9/17/14

6.2. Materials and methods

In this study we have used the TIAM electrode to do the detection the target miRNAs. We performed isolation and detection with three PC patients sample and three healthy patients sample to determine the fold change in the target miRNAs levels. The used samples were mentioned in dark color in Table 6.1. In addition to those three target miRNAs we also detected let-7i miRNAs as a control where i is equal to a, b, c, etc. Since we showed currently that our technique is incapable of differentiating single base pair mismatches we cannot detect the let-7 a,b,c separately. Therefore we performed the experiment to detect the let-7 miRNA family. We purchased the fluorophore attached complementary DNA probes from The Midland Certified Reagent Company. We used complementary DNA probe of let-7b to detect the let-7 family.

First the plasma sample was collected from the -80^{0}C freezer and thawed in the room temperature. Once it's thawed we performed the miRNA isolation using QIAGEN miRNeasy Serum/Plasma Advanced kit (Cat No: 217204) by following the standard procedure provided by the manufacturers. The isolated miRNAs were eluted in 0.01xTE buffer which is the buffer that we used during our miRNA detection experiments in chapter 5. Then the eluted miRNA sample was separated into 4 samples and 1ng of corresponding complementary DNA probes were added to each tubes for the hybridization labelling. Hybridization was performed by heating the sample to 95^{0}C for 5 minutes and left the sample in the room temperature for 55 minutes. Here we also performed the experiments with half diluted miRNA sample to quantify the capability of the technique.

Then the hybridized sample was added over the TIAM electrode and $10V_{p-p}$ and 1 MHz signal was applied to the TIAM electrode. Then the detection of target miRNAs were performed according to the steps mentioned in the chapter 5. Finally we plot the results to analyze the fold change of target miRNAs in healthy patients and PC patients.

The isolation of the miRNAs was performed with Dr. Glenn Dorsam and his student Dr. Manpreet Bains from the Department of Veterinary and Microbiological Sciences, NDSU.

6.3. Experiment results

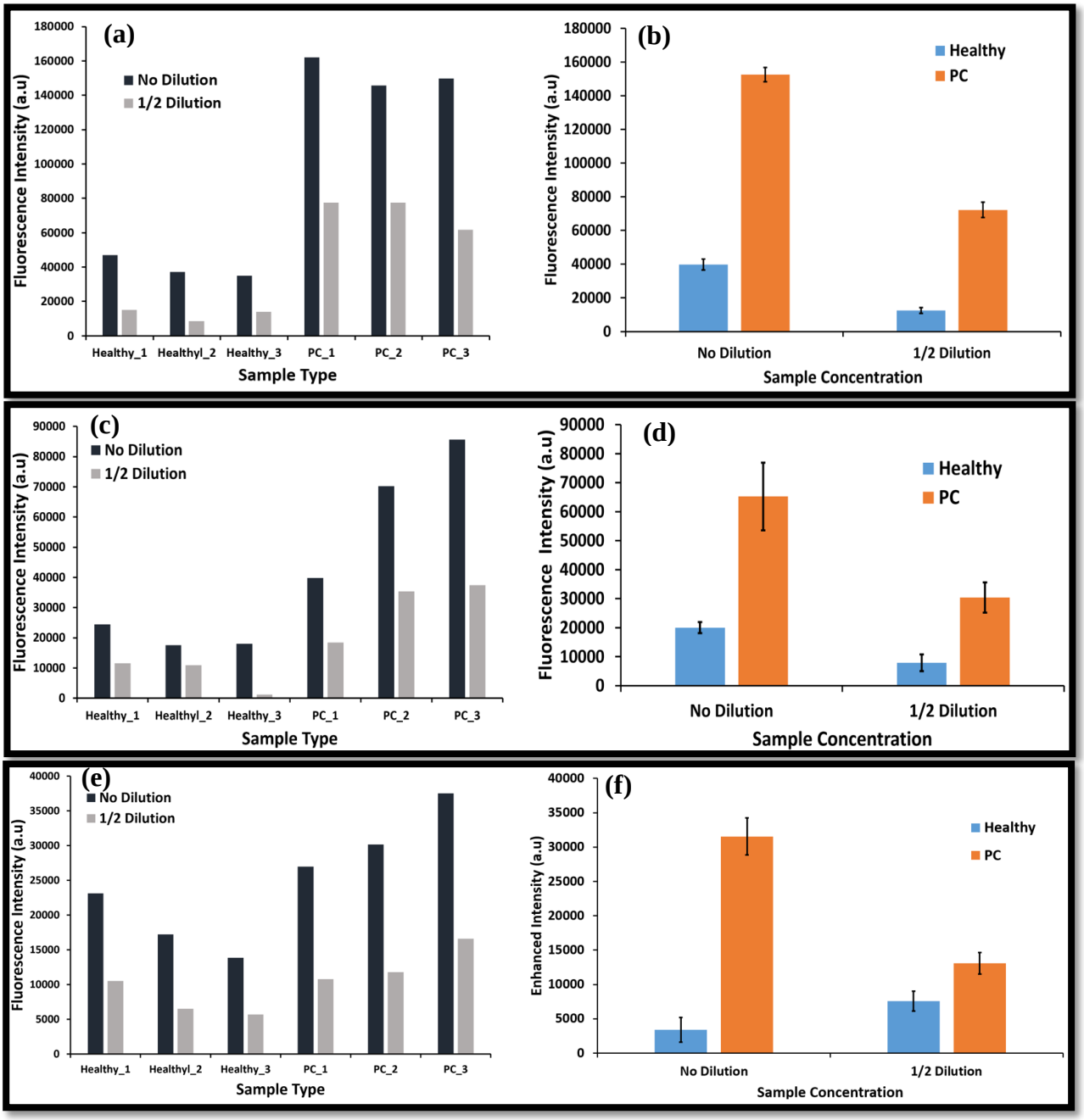

Figure 6.1: Experiment results of PC target miRNA detection. **(a)** obtained fluorescence intensities for miR-642b detection with no dilution and ½ dilution; **(b)** summary of the miR-642b detection experiment results of PC patients and Healthy Patients with No dilution and ½ Dilution. **(c)** obtained fluorescence intensities for miR-885-5p detection with no dilution and ½ dilution; **(d)** summary of the miR-885-5p detection experiment results of PC patients and Healthy Patients with No dilution and ½ Dilution. **(e)** obtained fluorescence intensities for miR-22 detection with no dilution and ½ dilution; **(f)** summary of the miR-22 detection experiment results of PC patients and Healthy Patients with No dilution and ½ Dilution.

From the experiments results (Figure 6.1) that we obtained it can be clearly concluded the level of target miRNAs was increased (up regulated) in PC patients compared to the healthy patients. The ½ dilution experiment also showing an agreement with the no dilution results which is almost equal to ½. Then we calculated the fold change in the intensities to compare the results with the published articles (Table 6.1). The obtained intensities were shown an agreement with the published articles [27]. Here the results vary from patients to patient. Therefore the fold changes were calculated from the average.

Table 6.2: PC target miRNAs fold change

Target miRNA	Fold Change (Intensity[PC/Healthy])
miR-642b	3.838665839
miR-885-5p	3.255919597
miR-22	2.245851442

Then we calculate the intensity and the fold change of let-7 family of miRNA. The results were shown in Figure 6.2.

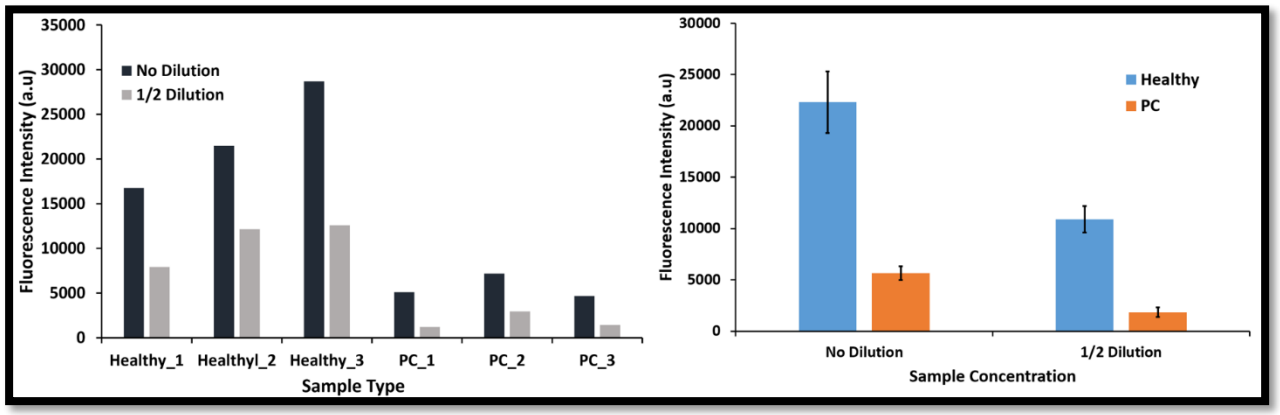

Figure 6.2: Experiment results of let-7i miRNA detection. **(a)** obtained fluorescence intensities for let-7i miRNA detection with no dilution and ½ dilution; **(b)** summary of the let-7i miRNA detection experiment results of PC patients and Healthy Patients with No dilution and ½ Dilution.

The let-7i miRNA detection experiment results (Figure 6.2) shows that the let-7i miRNA level got reduced (down regulated) in the cancer patients compare to the heathy patients. Here

also we obtain a variation on the level of let-7i miRNA from patient to patient, therefore we used the average to calculate the fold change in the let-7i miRNA. The fold change results was showed in Table6.2. The obtained fold change also shown an agreement with the published articles [27].

Table 6.3: Let-7i miRNA fold change

Target miRNA	Fold Change (Intensity [Healthy/PC])
Let-7i	3.950773

Then we developed a standard curve to determine the exact concentration of target miRNAs from the patient's sample. We performed sets of experiments by spiking in the known concentration (nm to fM) of miRNAs (let-7b) in NF water and isolated them and performed the experiments to detect them according to the steps discussed in the chapter 5. After that we calculated the fluorescence intensity and fit that intensities into a curve (Figure. 6.3).

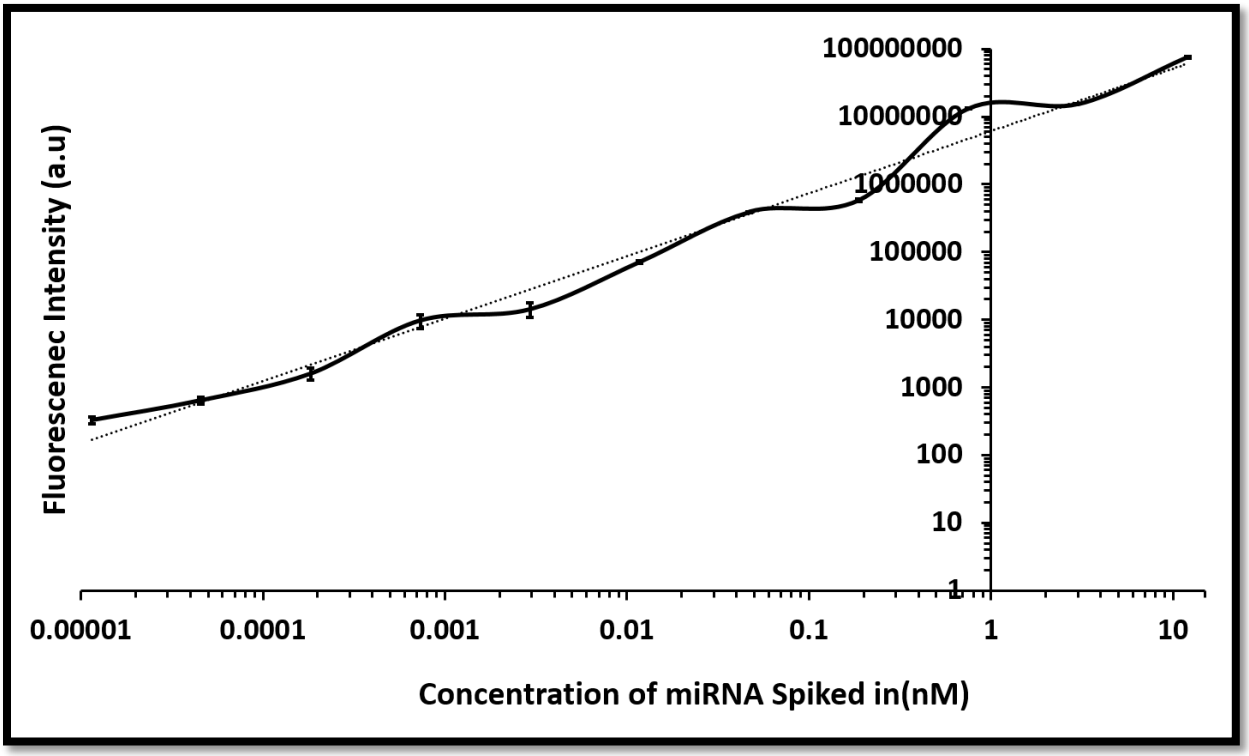

Figure 6.3: Developed standard curve for unknown molarity quantification. Dot line shows the fitted curve obtained through the least squares algorithm.

We used the least squares algorithm to obtain the best fitting curve and the equation is $y = 10^6 x^{0.745}$ where the R^2 value is equal to 0.9741. From this equation we found out the exact concentration of the target miRNAs (miR-885-5p and let-7i) in the sample. The calculated exact concentration was showed in the table 6.3.

Table 6.4: Calculated concentration of miRNAs

	miR-885-5p(pM)	**miR-let-7i (pM)**
Healthy_1	0.823527197	0.496040674
Healthy_2	0.52812741	0.692786687
Healthy_3	0.549963304	1.020845335
Average (Healthy)	***0.630414602***	***0.72851246***
PC_1	1.584966339	0.100695008
PC_2	3.394480412	0.158441836
PC_3	4.431452305	0.089381292
Average (PC)	***3.136966352***	***0.116172712***

6.4. Conclusions

In this study we have tested our iLluminate-miRNA technique in real healthy and cancer patient's sample. The results obtained were showing an agreement with the previous published results. The detection was performed within 1 hour and 30 minutes including isolation, hybridization, experiment and analysis. Here we performed the hybridization according to the standard procedure therefore it took nearly 1 hour. If we reduce the hybridization time then we should be able to detect the target miRNAs within 40 minutes of collecting them from the patients. Currently we are performing the experiments to reduce the time and increase the efficiency of hybridization.

CHAPTER 7. OVERALL CONCLUSION

In this study we have developed highly sensitive, low-cost and speedy biomarker detection techniques for potential clinical applications at point-of-care settings by utilizing DEP and different phenomenon of fluorescence based platforms. We have investigated different approaches during the biosensor development and at final, we have proved that the successful integration of DEP and plasmonic enhancement phenomenon of fluorescence based platform is superior to the current biomarker detection techniques available in the diagnosis field. Further study and improvement on the developed technique have the potential to detect a single target biomarker from the patient's plasma/serum sample. Single target biomarker detection from the patient's sample will greatly reduce the worldwide disease burden and results in zero disease related deaths in future. From this study, we have opened a new pathway for the researches who concentrates in biosensor development for early disease detection/monitoring.

Initially, we have started to develop a biosensor to detect the rare target biomarkers by utilizing the cross-over phenomenon of DEP. Here we have attached different concentration of avidin molecules to the surface of the biotinylated beads and measured the cross-over frequency for each sample in PIDE electrodes. From the results we obtained the detection limit of 416 avidin molecules per bead, further reduction of avidin molecules does not result in the crossover frequency change. In this study we have used 1000,000 of beads, reduction of beads number resulted in the observation of beads difficult during the experiments. Therefore we could not go beyond a certain limit of detection. To improve the limit of detection we have integrated the DEP with fluorescence based platform to quantify the target biomarker molecules in our next study.

During the second study discussed in chapter 3, the positive (pDEP) and negative (nDEP) phenomenon of DEP was utilized and integrated with the fluorescence based platform and the detection was performed. Here different concentration of fluorophore attached avidin molecules

were attached to biotinylated polystyrene beads surface. Then the sample was pipetted over the PIDE electrodes, then the pDEP was applied to attract all the avidin attached beads to the electrode surface and nDEP was applied to concentrate the beads inside the detection spots in the PIDE electrodes. After concentration of the avidin attached beads in the certain spots we measured the fluorescence intensity and the intensity was converted into molarity. In this study we have reported 1.5 pM of detection limit. Further reduction in avidin concentration reduces the florescence intensity to the background fluorescence. But the detection limit obtained through this system was not enough to detect early stage cancers. Therefore to further improve the fluorescence intensity we have utilized the plasmonic enhancement phenomenon of fluorescence based platform in our next study.

During the third study discussed in chapter 4, the DEP was integrated with the plasmonic enhancement phenomenon of fluorescence based platform to quantify the rare target biomarkers. Here we avoided the beads completely and used only the fluorophore attached avidin molecules. To achieve maximum plasmonic enhancement the fluorophore attached molecules should be placed inside the nano-structures at a certain distance. Therefore the pDEP was applied to place the fluorophore attached avidin molecules to concentrate them inside the nano-structures located at the edge of the PIDE electrodes, and the nDEP/zero force DEP was utilized to place the molecules at a certain distance from the nano structures, to achieve a maximum enhancement through plasmonic effects. From this study, we obtain million-fold improvement in the florescence enhancement compare to the free fluorescence without metal nano-structures. The results obtained from this studies showed us a promising way to do the detection of rare target biomarkers from biological sample in low concentrations. Therefore in the fourth study (chapter

5) we have utilized this technique to detect the target miRNA molecules from the human serum sample.

During the fourth study discussed in chapter 5, we have developed a new electrode pair (TIAM) which is capable of producing much more DEP force on the target miRNAs to concentrate them inside the nano-structures located at the edges of the electrodes. Here we used let-7b miRNA to proof the concept. First, we identified the suitable frequency to attract and place the target labelled miRNAs inside the nano-structures, and place the non-target and excess fluorophore attached complimentary labelling DNA probes away from the nano structures. During this study we found out with DEP there were thermophoresis and diffusion mechanisms also contributes in avoiding the placement of excess fluorophore attached complimentary DNA labelling probes inside the nono-structures. During this study we also have successfully integrated the three important parameters of plasmonic enhancements to achieve maximum intensity through fluorescence measurements. In this study we have performed experiments simultaneously with qRT-PCR to compare the efficiency. From the results, we have proved that our technique is ~10x times superior in target miRNA detection from water at the same time ~657x time superior in human serum samples. Meanwhile our technique was proved to be faster and cost effective than the current miRNA detection techniques. After successful development of the miRNA detection technique we have validated the technique with the real patients sample in our fifth study (chapter 6).

During the sixth study discussed in chapter 6, we have utilized our target miRNA detection technique to quantify the target disease related miRNA molecules from the PC patient's and healthy patient's plasma samples. In this study we have detected four different target miRNAs from the patient's sample. The observed results were compared with the

published literatures and found to be in agreement. Currently, no other miRNA detecting technique can quantify the target miRNAs concentration in the sample. Here we have developed a standard curve to determine the exact concentration of target miRNAs in the patient's sample. Currently the research group is performing the target miRNA detection from breast and brain cancer patient's plasma samples. At the same time the research group is focusing in reducing the detection time to 30 minutes from collecting the sample by optimizing the hybridization time and efficiency.

Finally, we have developed a novel approach to detect target biomarkers from the patient's sample. This technique is not only limited to detect the target miRNAs but also it can be applicable to detect DNA, RNA and antigens. Further improvement of this technique will lead to a single target biomarker detection from the patient's plasma/serum samples.

REFERENCES

(1) Siegel, R. L.; Miller, K. D. Cancer Statistics , 2019. **2019**, *69* (1), 7–34. https://doi.org/10.3322/caac.21551.

(2) Siegel, R. L.; Miller, K. D.; Jemal, A. Cancer Statistics, 2018. *CA. Cancer J. Clin.* **2018**, *68* (1), 7–30. https://doi.org/10.3322/caac.21442.

(3) Weir, H. K.; Thompson, T. D.; Soman, A.; Møller, B.; Leadbetter, S. The Past, Present, and Future of Cancer Incidence in the United States: 1975 through 2020. *Cancer* **2015**. https://doi.org/10.1002/cncr.29258.

(4) Schiffman, J. D.; Fisher, P. G.; Gibbs, P. Early Detection of Cancer: Past, Present, and Future. *Am. Soc. Clin. Oncol. Educ. book. Am. Soc. Clin. Oncol. Annu. Meet.* **2015**. https://doi.org/10.14694/EdBook_AM.2015.35.57.

(5) Etzioni, R.; Urban, N.; Ramsey, S.; McIntosh, M.; Schwartz, S.; Reid, B.; Radich, J.; Anderson, G.; Hartwell, L. Early Detection: The Case for Early Detection. *Nat. Rev. Cancer* **2003**, *3* (4), 243–252. https://doi.org/10.1038/nrc1041.

(6) Chan, A.; Prassas, I.; Dimitromanolakis, A.; Brand, R. E.; Serra, S.; Diamandis, E. P.; Blasutig, I. M. Validation of Biomarkers That Complement CA19.9 in Detecting Early Pancreatic Cancer. *Clin. Cancer Res.* **2014**. https://doi.org/10.1158/1078-0432.CCR-14-0289.

(7) Strimbu, K.; Tavel, J. A. What Are Biomarkers? *Current Opinion in HIV and AIDS*. 2010. https://doi.org/10.1097/COH.0b013e32833ed177.

(8) Henry, N. L.; Hayes, D. F. Cancer Biomarkers. *Molecular Oncology*. 2012. https://doi.org/10.1016/j.molonc.2012.01.010.

(9) Devasena, T. Biomarkers. In *SpringerBriefs in Applied Sciences and Technology*; 2017. https://doi.org/10.1007/978-981-10-0923-5_3.

(10) Mayeux, R. Biomarkers: Potential Uses and Limitations. *NeuroRx* **2004**. https://doi.org/10.1602/neurorx.1.2.182.

(11) Hales, C. N.; Randle, P. J. Immunoassay of insulin with insulin antibody precipitate. *Lancet* **1963**. https://doi.org/10.1016/S0140-6736(63)91215-7.

(12) Magdelenat, H.; Merle, S.; Zajdela, A. Enzyme Immunoassay of Estrogen Receptors in Fine Needle Aspirates of Breast Tumors. *Cancer Res.* **1986**.

(13) Yalow, R. S.; Berson, S. A. Immunoassay of Endogenous Plasma Insulin in Man. *Obes. Res.* **1996**. https://doi.org/10.1002/j.1550-8528.1996.tb00274.x.

(14) Wu, J.; Fu, Z.; Yan, F.; Ju, H. Biomedical and Clinical Applications of Immunoassays and Immunosensors for Tumor Markers. *TrAC - Trends Anal. Chem.* **2007**. https://doi.org/10.1016/j.trac.2007.05.007.

(15) Chen, H.; Jiang, C.; Yu, C.; Zhang, S.; Liu, B.; Kong, J. Protein Chips and Nanomaterials for Application in Tumor Marker Immunoassays. *Biosensors and Bioelectronics*. 2009. https://doi.org/10.1016/j.bios.2009.03.020.

(16) Chikkaveeraiah, B. V.; Bhirde, A. A.; Morgan, N. Y.; Eden, H. S.; Chen, X. Electrochemical Immunosensors for Detection of Cancer Protein Biomarkers. *ACS Nano* **2012**, *6* (8), 6546–6561. https://doi.org/10.1021/nn3023969.

(17) Rusling, J. F.; Kumar, C. V.; Gutkind, J. S.; Patel, V. Measurement of Biomarker Proteins for Point-of-Care Early Detection and Monitoring of Cancer. *Analyst* **2010**. https://doi.org/10.1039/c0an00204f.

(18) Daniels, J. S.; Pourmand, N. Label-Free Impedance Biosensors: Opportunities and Challenges. *Electroanalysis* **2007**. https://doi.org/10.1002/elan.200603855.
(19) Jayasooriya, V.; Nawarathna, D. Design of Micro-Interdigitated Electrodes and Detailed Impedance Data Analysis for Label-Free Biomarker Quantification. *Electroanalysis* **2017**. https://doi.org/10.1002/elan.201600364.
(20) Rodriguez, M. C.; Kawde, A. N.; Wang, J. Aptamer Biosensor for Label-Free Impedance Spectroscopy Detection of Proteins Based on Recognition-Induced Switching of the Surface Charge. *Chem. Commun.* **2005**. https://doi.org/10.1039/b506571b.
(21) Varshney, M.; Li, Y.; Srinivasan, B.; Tung, S. A Label-Free, Microfluidics and Interdigitated Array Microelectrode-Based Impedance Biosensor in Combination with Nanoparticles Immunoseparation for Detection of Escherichia Coli O157:H7 in Food Samples. *Sensors Actuators, B Chem.* **2007**. https://doi.org/10.1016/j.snb.2007.03.045.
(22) Cai, H.; Lee, T. M. H.; Hsing, I. M. Label-Free Protein Recognition Using an Aptamer-Based Impedance Measurement Assay. *Sensors Actuators, B Chem.* **2006**. https://doi.org/10.1016/j.snb.2005.06.017.
(23) Zou, Z.; Kai, J.; Rust, M. J.; Han, J.; Ahn, C. H. Functionalized Nano Interdigitated Electrodes Arrays on Polymer with Integrated Microfluidics for Direct Bio-Affinity Sensing Using Impedimetric Measurement. *Sensors Actuators, A Phys.* **2007**. https://doi.org/10.1016/j.sna.2006.12.006.
(24) Xu, D.; Xu, D.; Yu, X.; Liu, Z.; He, W.; Ma, Z. Label-Free Electrochemical Detection for Aptamer-Based Array Electrodes. *Anal. Chem.* **2005**. https://doi.org/10.1021/ac050192m.
(25) Berdat, D.; Martin Rodríguez, A. C.; Herrera, F.; Gijs, M. A. M. Label-Free Detection of DNA with Interdigitated Micro-Electrodes in a Fluidic Cell. *Lab Chip* **2008**. https://doi.org/10.1039/b712609c.
(26) Poghossian, A.; Cherstvy, A.; Ingebrandt, S.; Offenhäusser, A.; Schöning, M. J. Possibilities and Limitations of Label-Free Detection of DNA Hybridization with Field-Effect-Based Devices. In *Sensors and Actuators, B: Chemical*; 2005. https://doi.org/10.1016/j.snb.2005.03.083.
(27) Ganepola, G. A.; Rutledge, J. R.; Suman, P.; Yiengpruksawan, A.; Chang, D. H. Novel Blood-Based MicroRNA Biomarker Panel for Early Diagnosis of Pancreatic Cancer. *World J Gastrointest Oncol January* **2014**. https://doi.org/10.4251/wjgo.v6.i1.22.
(28) Ferracin, M.; Veronese, A.; Negrini, M. Micromarkers: MiRNAs in Cancer Diagnosis and Prognosis. *Expert Review of Molecular Diagnostics*. 2010. https://doi.org/10.1586/erm.10.11.
(29) Cissell, K. A.; Deo, S. K. Trends in MicroRNA Detection. *Anal. Bioanal. Chem.* **2009**. https://doi.org/10.1007/s00216-009-2744-6.
(30) Várallyay, É.; Burgyán, J.; Havelda, Z. MicroRNA Detection by Northern Blotting Using Locked Nucleic Acid Probes. *Nat. Protoc.* **2008**. https://doi.org/10.1038/nprot.2007.528.
(31) Jiang, J.; Lee, E. J.; Gusev, Y.; Schmittgen, T. D. Real-Time Expression Profiling of MicroRNA Precursors in Human Cancer Cell Lines. *Nucleic Acids Res.* **2005**. https://doi.org/10.1093/nar/gki863.
(32) Git, A.; Dvinge, H.; Salmon-Divon, M.; Osborne, M.; Kutter, C.; Hadfield, J.; Bertone, P.; Caldas, C. Systematic Comparison of Microarray Profiling, Real-Time PCR, and next-Generation Sequencing Technologies for Measuring Differential MicroRNA Expression. *RNA* **2010**. https://doi.org/10.1261/rna.1947110.

(33) Wen, Y.; Pei, H.; Shen, Y.; Xi, J.; Lin, M.; Lu, N.; Shen, X.; Li, J.; Fan, C. DNA Nanostructure-Based Interfacial Engineering for PCR-Free Ultrasensitive Electrochemical Analysis of MicroRNA. *Sci. Rep.* **2012**. https://doi.org/10.1038/srep00867.
(34) Wu, R.; Wood, M.; Thrush, A.; Walton, E. F.; Varkonyi-Gasic, E. Real-Time PCR Quantification of Plant MiRNAs Using Universal ProbeLibrary Technology. *Biochemica* **2007**.
(35) Chen, Y.; Gelfond, J. A. L.; McManus, L. M.; Shireman, P. K. Reproducibility of Quantitative RT-PCR Array in MiRNA Expression Profiling and Comparison with Microarray Analysis. *BMC Genomics* **2009**. https://doi.org/10.1186/1471-2164-10-407.
(36) Love, C.; Dave, S. MicroRNA Expression Profiling Using Microarrays. *Methods Mol. Biol.* **2013**. https://doi.org/10.1007/978-1-62703-357-2-21.
(37) Gao, Z.; Yu, Y. H. A MicroRNA Biosensor Based on Direct Chemical Ligation and Electrochemically Amplified Detection. *Sensors Actuators, B Chem.* **2007**. https://doi.org/10.1016/j.snb.2006.04.090.
(38) Smith, D. A.; Newbury, L. J.; Drago, G.; Bowen, T.; Redman, J. E. Electrochemical Detection of Urinary MicroRNAs via Sulfonamide-Bound Antisense Hybridisation. *Sensors Actuators, B Chem.* **2017**. https://doi.org/10.1016/j.snb.2017.06.069.
(39) Roy, S.; Soh, J. H.; Gao, Z. A Microfluidic-Assisted Microarray for Ultrasensitive Detection of MiRNA under an Optical Microscope. *Lab Chip* **2011**. https://doi.org/10.1039/c0lc00638f.
(40) S., K.; M.A., A.; P., A.; V.V., A.; R., J.; S., M. Microfluidic-Integrated Biosensors: Prospects for Point-of-Care Diagnostics. *Biotechnology Journal*. 2013.
(41) Degliangeli, F.; Pompa, P. P.; Fiammengo, R. Nanotechnology-Based Strategies for the Detection and Quantification of MicroRNA. *Chemistry - A European Journal*. 2014. https://doi.org/10.1002/chem.201402649.
(42) Cheng, L.; Quek, C. Y. J.; Sun, X.; Bellingham, S. A.; Hill, A. F. The Detection of MicroRNA Associated with Alzheimer's Disease in Biological Fluids Using next-Generation Sequencing Technologies. *Front. Genet.* **2013**. https://doi.org/10.3389/fgene.2013.00150.
(43) Pritchard, C. C.; Cheng, H. H.; Tewari, M.; Division, B.; Hutchinson, F.; Health, P.; Divisions, S.; Hutchinson, F. MicroRNA Profiling: Approaches and Considerations Colin. *Nat Rev Genet* **2015**, *13* (5), 358–369. https://doi.org/10.1038/nrg3198.MicroRNA.
(44) Zubakov, D.; Boersma, A. W. M.; Choi, Y.; Van Kuijk, P. F.; Wiemer, E. A. C.; Kayser, M. MicroRNA Markers for Forensic Body Fluid Identification Obtained from Microarray Screening and Quantitative RT-PCR Confirmation. *Int. J. Legal Med.* **2010**. https://doi.org/10.1007/s00414-009-0402-3.
(45) Dong, H.; Lei, J.; Ding, L.; Wen, Y.; Ju, H.; Zhang, X. MicroRNA: Function, Detection, and Bioanalysis. *Chemical Reviews*. 2013. https://doi.org/10.1021/cr300362f.
(46) Pohl, H. A. The Motion and Precipitation of Suspensoids in Divergent Electric Fields. *J. Appl. Phys.* **1951**, *22* (7), 869–871. https://doi.org/10.1063/1.1700065.
(47) Pethig, R. Publisher's Note: "Review Article-Dielectrophoresis: Status of the Theory, Technology, and Applications" [Biomicrofluidics 4, 022811 2010]. *Biomicrofluidics*. 2010. https://doi.org/10.1063/1.3474458.
(48) Gupta, T. Dielectric Materials. In *Copper Interconnect Technology*; 2009. https://doi.org/10.1007/978-1-4419-0076-0_2.

(49) Sihvola, A. Dielectric Polarization and Particle Shape Effects. *Journal of Nanomaterials*. 2007. https://doi.org/10.1155/2007/45090.
(50) Pethig, R. R.; Goethe, J. W. V; Pethig, R. R. *Dielectrophoresis*; 2017. https://doi.org/10.1007/978-1-4614-5491-5_319.
(51) Belkin, A.; Bezryadin, A.; Hendren, L.; Hubler, A. Recovery of Alumina Nanocapacitors after High Voltage Breakdown. *Sci. Rep.* **2017**, *7* (1), 1–8. https://doi.org/10.1038/s41598-017-01007-9.
(52) Thoms, E.; Sippel, P.; Reuter, D.; Weiß, M.; Loidl, A.; Krohns, S. Dielectric Study on Mixtures of Ionic Liquids. *Sci. Rep.* **2017**, *7* (1), 1–9. https://doi.org/10.1038/s41598-017-07982-3.
(53) Lee, D.; Hwang, B.; Kim, B. The Potential of a Dielectrophoresis Activated Cell Sorter (DACS) as a next Generation Cell Sorter. *Micro Nano Syst. Lett.* **2016**. https://doi.org/10.1186/s40486-016-0028-4.
(54) Velmanickam, L.; Laudenbach, D.; Nawarathna, D. Dielectrophoretic Label-Free Immunoassay for Rare-Analyte Quantification in Biological Samples. *Phys. Rev. E* **2016**. https://doi.org/10.1103/PhysRevE.94.042408.
(55) Hughes, M. P. Strategies for Dielectrophoretic Separation in Laboratory-on-a-Chip Systems. *Electrophoresis*. 2002. https://doi.org/10.1002/1522-2683(200208)23:16<2569::AID-ELPS2569>3.0.CO;2-M.
(56) Dimaki, M.; Bøggild, P. Dielectrophoresis of Carbon Nanotubes Using Microelectrodes: A Numerical Study. *Nanotechnology* **2004**. https://doi.org/10.1088/0957-4484/15/8/039.
(57) Chou, C. F.; Tegenfeldt, J. O.; Bakajin, O.; Chan, S. S.; Cox, E. C.; Darnton, N.; Duke, T.; Austin, R. H. Electrodeless Dielectrophoresis of Single- and Double-Stranded DNA. *Biophys. J.* **2002**. https://doi.org/10.1016/S0006-3495(02)73977-5.
(58) Goater, A. D.; Pethig, R. Electrorotation and Dielectrophoresis. *Parasitology* **1998**. https://doi.org/10.1017/S0031182099004114.
(59) Kadaksham, A. T. J.; Singh, P.; Aubry, N. Dielectrophoresis of Nanoparticles. *Electrophoresis* **2004**. https://doi.org/10.1002/elps.200406092.
(60) Zhang, C.; Khoshmanesh, K.; Mitchell, A.; Kalantar-Zadeh, K. Dielectrophoresis for Manipulation of Micro/Nano Particles in Microfluidic Systems. *Analytical and Bioanalytical Chemistry*. 2010. https://doi.org/10.1007/s00216-009-2922-6.
(61) Gascoyne, P. R. C.; Vykoukal, J. Particle Separation by Dielectrophoresis. *Electrophoresis*. 2002. https://doi.org/10.1002/1522-2683(200207)23:13<1973::AID-ELPS1973>3.0.CO;2-1.
(62) Pethig, R. Review—Where Is Dielectrophoresis (DEP) Going? *J. Electrochem. Soc.* **2017**, *164* (5), B3049–B3055. https://doi.org/10.1149/2.0071705jes.
(63) Çetin, B.; Li, D. Dielectrophoresis in Microfluidics Technology. *Electrophoresis*. 2011. https://doi.org/10.1002/elps.201100167.
(64) Jones, T. B. Basic Theory of Dielectrophoresis and Electrorotation. *IEEE Eng. Med. Biol. Mag.* **2003**. https://doi.org/10.1109/MEMB.2003.1304999.
(65) Pethig, R. Dielectrophoresis: Status of the Theory, Technology, and Applications. *Biomicrofluidics* **2010**. https://doi.org/10.1063/1.3456626.
(66) Pohl, H. A.; Crane, J. S. Dielectrophoresis of Cells. *Biophys. J.* **1971**. https://doi.org/10.1016/S0006-3495(71)86249-5.
(67) Kuzyk, A. Dielectrophoresis at the Nanoscale. *Electrophoresis*. 2011. https://doi.org/10.1002/elps.201100038.

(68) Qian, C.; Huang, H.; Chen, L.; Li, X.; Ge, Z.; Chen, T.; Yang, Z.; Sun, L. Dielectrophoresis for Bioparticle Manipulation. *International Journal of Molecular Sciences*. 2014. https://doi.org/10.3390/ijms151018281.
(69) Urdaneta, M.; Smela, E. Multiple Frequency Dielectrophoresis. *Electrophoresis* **2007**. https://doi.org/10.1002/elps.200600786.
(70) Gonga, G.; Li, B. Dielectric Properties of Bionanocomposites. In *Polymer Nanocomposites for Dielectrics*; 2017. https://doi.org/10.1201/9781315364490.
(71) Lo, Y. J.; Lin, Y. Y.; Lei, U.; Wu, M. S.; Yang, P. C. Measurement of the Clausius-Mossotti Factor of Generalized Dielectrophoresis. *Appl. Phys. Lett.* **2014**. https://doi.org/10.1063/1.4866344.
(72) Gierhart, B. C.; Howitt, D. G.; Chen, S. J.; Smith, R. L.; Collins, S. D. Frequency Dependence of Gold Nanoparticle Superassembly by Dielectrophoresis. *Langmuir* **2007**. https://doi.org/10.1021/la701472y.
(73) Ehrlich, P. Dielectric Properties of Teflon from Room Temperature to 314-Degrees-C and from Frequencies of 10_2 to 10_5 c/S. *J. Res. Natl. Bur. Stand. (1934).* **1953**. https://doi.org/10.6028/jres.051.024.
(74) Hwang, Y.; Sohn, H.; Phan, A.; Yaghi, O. M.; Candler, R. N. Dielectrophoresis-Assembled Zeolitic Imidazolate Framework Nanoparticle-Coupled Resonators for Highly Sensitive and Selective Gas Detection. *Nano Lett.* **2013**. https://doi.org/10.1021/nl4027692.
(75) Salimi, E.; Braasch, K.; Butler, M.; Thomson, D. J.; Bridges, G. E. Dielectric Model for Chinese Hamster Ovary Cells Obtained by Dielectrophoresis Cytometry. *Biomicrofluidics* **2016**. https://doi.org/10.1063/1.4940432.
(76) Mortadi, A.; El Melouky, A.; Chahid, E. G.; El Moznine, R.; Cherkaoui, O. Studies of the Clausius–Mossotti Factor. *J. Phys. Stud.* **2016**.
(77) Honegger, T.; Berton, K.; Picard, E.; Peyrade, D. Determination of Clausius-Mossotti Factors and Surface Capacitances for Colloidal Particles. *Appl. Phys. Lett.* **2011**. https://doi.org/10.1063/1.3583441.
(78) Cui, L.; Holmes, D.; Morgan, H. The Dielectrophoretic Levitation and Separation of Latex Beads in Microchips. *Electrophoresis* **2001**. https://doi.org/10.1002/1522-2683(200110)22:18<3893::AID-ELPS3893>3.0.CO;2-2.
(79) Pethig, R. Publisher's Note: "Review Article—Dielectrophoresis: Status of the Theory, Technology, and Applications" [Biomicrofluidics 4, 022811 (2010)]. *Biomicrofluidics* **2010**. https://doi.org/10.1063/1.3474458.
(80) Gossett, D. R.; Weaver, W. M.; Mach, A. J.; Hur, S. C.; Tat, H.; Tse, K.; Lee, W.; Amini, H.; Carlo, D. Di. Label-Free Cell Separation and Sorting in Microfluidic Systems. **2010**, 3249–3267. https://doi.org/10.1007/s00216-010-3721-9.
(81) Pethig, R.; Markx, G. H. Applications of Dielectrophoresis in Biotechnology. *Trends Biotechnol.* **1997**, *15* (10), 426–432. https://doi.org/10.1016/S0167-7799(97)01096-2.
(82) Kim, U.; Qian, J.; Kenrick, S. A.; Daugherty, P. S.; Soh, H. T. Multitarget Dielectrophoresis Activated Cell Sorter. *Anal. Chem.* **2008**. https://doi.org/10.1021/ac8015938.
(83) Mulhall, H. J.; Labeed, F. H.; Kazmi, B.; Costea, D. E.; Hughes, M. P.; Lewis, M. P. Cancer, Pre-Cancer and Normal Oral Cells Distinguished by Dielectrophoresis. *Anal. Bioanal. Chem.* **2011**. https://doi.org/10.1007/s00216-011-5337-0.

(84) Patel, S.; Showers, D.; Vedantam, P.; Tzeng, T. R.; Qian, S.; Xuan, X. Microfluidic Separation of Live and Dead Yeast Cells Using Reservoir-Based Dielectrophoresis. *Biomicrofluidics* **2012**. https://doi.org/10.1063/1.4732800.
(85) Markx, G. H.; Talary, M. S.; Pethig, R. Separation of Viable and Non-Viable Yeast Using Dielectrophoresis. *J. Biotechnol.* **1994**. https://doi.org/10.1016/0168-1656(94)90117-1.
(86) Velmanickam, L.; Nawarathna, D. Design and Fabrication of a Dielectrophoretic Cell Trap Array. *Adv. Sci. Technol. Eng. Syst. J.* **2017**, *2* (1), 84–89. https://doi.org/10.1109/HICSS.2013.399.
(87) Velmanickam, L.; Nawarathna, K. Dielectrophoretic Cell Isolation in Microfluidics Channels for High-Throughput Biomedical Applications. *IEEE Int. Conf. Electro Inf. Technol.* **2016**, *2016–Augus*, 302–306. https://doi.org/10.1109/EIT.2016.7535256.
(88) Asbury, C. L.; Diercks, A. H.; Van Den Engh, G. Trapping of DNA by Dielectrophoresis. *Electrophoresis* **2002**. https://doi.org/10.1002/1522-2683(200208)23:16<2658::AID-ELPS2658>3.0.CO;2-O.
(89) Velmanickam, L.; Bains, M.; Fondakowski, M. ILluminate-MiRNA : Paradigm for High-Throughput , Low-Cost , and Sensitive MiRNA Detection in Serum Samples at Point-of-Care. **2019**.
(90) Swami, N.; Chou, C. F.; Ramamurthy, V.; Chaurey, V. Enhancing DNA Hybridization Kinetics through Constriction-Based Dielectrophoresis. *Lab Chip* **2009**. https://doi.org/10.1039/b910598k.
(91) Gagnon, Z.; Senapati, S.; Chang, H. C. Optimized DNA Hybridization Detection on Nanocolloidal Particles by Dielectrophoresis. *Electrophoresis* **2010**. https://doi.org/10.1002/elps.200900473.
(92) Demircan, Y.; Özgür, E.; Külah, H. Dielectrophoresis: Applications and Future Outlook in Point of Care. *Electrophoresis*. 2013. https://doi.org/10.1002/elps.201200446.
(93) Velmanickam, L.; Fondakowski, M.; Lima, I. T.; Nawarathna, D. Integrated Dielectrophoretic and Surface Plasmonic Platform for Million-Fold Improvement in the Detection of Fluorescent Events. *Biomicrofluidics* **2017**. https://doi.org/10.1063/1.5000008.
(94) Ballantyne, G. R.; Holtham, P. N. Evaluation of the Potential for Using Dielectrophoresis to Separate Minerals. *Miner. Eng.* **2014**. https://doi.org/10.1016/j.mineng.2013.09.009.
(95) Ballantyne, G. R.; Holtham, P. N. Application of Dielectrophoresis for the Separation of Minerals. *Miner. Eng.* **2010**. https://doi.org/http://dx.doi.org/10.1016/j.mineng.2009.09.001.
(96) Olariu, M.; Arcire, A.; Plonska-Brzezinska, M. E. Controlled Trapping of Onion-Like Carbon (OLC) via Dielectrophoresis. *J. Electron. Mater.* **2017**. https://doi.org/10.1007/s11664-016-4870-1.
(97) Ohtsuka, S.; Suetomi, H.; Hikita, M. Fundamental Properties of OFF-ON Resistance of a New Type Self-Recovering Fuse Operated by Dielectrophoresis. In *Conference Record of the International Power Modulator Symposium and High Voltage Workshop*; 2006. https://doi.org/10.1109/MODSYM.2006.365287.
(98) Froude, V. E.; Zhu, Y. Dielectrophoresis of Functionalized Lipid Unilamellar Vesicles (Liposomes) with Contrasting Surface Constructs. *J. Phys. Chem. B* **2009**. https://doi.org/10.1021/jp808454w.

(99) Allahrabbi, N.; Chia, Y. S. M.; Saifullah, M. S. M.; Lim, K. M.; Lanry Yung, L. Y. A Hybrid Dielectrophoretic System for Trapping of Microorganisms from Water. *Biomicrofluidics* **2015**. https://doi.org/10.1063/1.4922276.
(100) Kim, W. B.; Park, S. J.; Min, B. K.; Lee, S. J. Surface Finishing Technique for Small Parts Using Dielectrophoretic Effects of Abrasive Particles. *J. Mater. Process. Technol.* **2004**. https://doi.org/10.1016/j.jmatprotec.2004.01.010.
(101) Luo, Q.; Zhang, X.; Wang, H.; Qian, Y. The Use of Non-Uniform Electrokinetics to Enhance in Situ Bioremediation of Phenol-Contaminated Soil. *J. Hazard. Mater.* **2005**. https://doi.org/10.1016/j.jhazmat.2005.02.007.
(102) Abbasi Monfared, M.; Sheikhi, M.; Kasiri, N.; Mohammadi, T. Experimental Investigation of Oil-in-Water Microfiltration Assisted by Dielectrophoresis: Operational Condition Optimization. *Chem. Eng. Res. Des.* **2018**. https://doi.org/10.1016/j.cherd.2018.08.002.
(103) Thwar, P. K.; Linderman, J. J.; Burns, M. A. Electrodeless Direct Current Dielectrophoresis Using Reconfigurable Field-Shaping Oil Barriers. *Electrophoresis* **2007**. https://doi.org/10.1002/elps.200700373.
(104) Chou, C. F.; Zenhausern, F. Electrodeless Dielectrophoresis for Micro Total Analysis Systems. *IEEE Eng. Med. Biol. Mag.* **2003**. https://doi.org/10.1109/MEMB.2003.1266048.
(105) Regtmeier, J.; Eichhorn, R.; Viefhues, M.; Bogunovic, L.; Anselmetti, D. Electrodeless Dielectrophoresis for Bioanalysis: Theory, Devices and Applications. *Electrophoresis*. 2011. https://doi.org/10.1002/elps.201100055.
(106) Lakowicz, J. R. *Principles of Fluorescence Spectroscopy*; 2006. https://doi.org/10.1007/978-0-387-46312-4.
(107) Sinkeldam, R. W.; Wilhelmsson, L. M.; Tor, Y. Fluorescence Spectroscopy. In *Fluorescent Analogs of Biomolecular Building Blocks: Design and Applications*; 2016. https://doi.org/10.1002/9781119179320.ch1.
(108) Weiss, S. Fluorescence Spectroscopy of Single Biomolecules. *Science*. 1999. https://doi.org/10.1126/science.283.5408.1676.
(109) Lakowicz, J. R.; Malicka, J.; D'Auria, S.; Gryczynski, I. Release of the Self-Quenching of Fluorescence near Silver Metallic Surfaces. *Anal. Biochem.* **2003**. https://doi.org/10.1016/S0003-2697(03)00351-8.
(110) Aslan, K.; Gryczynski, I.; Malicka, J.; Matveeva, E.; Lakowicz, J. R.; Geddes, C. D. Metal-Enhanced Fluorescence: An Emerging Tool in Biotechnology. *Current Opinion in Biotechnology*. 2005. https://doi.org/10.1016/j.copbio.2005.01.001.
(111) Borisov, S. M.; Wolfbeis, O. S. Optical Biosensors. *Chem. Rev.* **2008**. https://doi.org/10.1021/cr068105t.
(112) Morales-Narváez, E.; Golmohammadi, H.; Naghdi, T.; Yousefi, H.; Kostiv, U.; Horák, D.; Pourreza, N.; Merkoçi, A. Nanopaper as an Optical Sensing Platform. *ACS Nano* **2015**. https://doi.org/10.1021/acsnano.5b03097.
(113) Shtenberg, G.; Segal, E. Porous Silicon Optical Biosensors. In *Handbook of Porous Silicon: Second Edition*; 2018; Vol. 2–2, pp 1263–1273. https://doi.org/10.1007/978-3-319-71381-6_87.
(114) Damborský, P.; Švitel, J.; Katrlík, J.; Dey, D.; Goswami, T.; Liedberg, B.; Nylander, C.; Lunström, I.; Schasfoort, R. B. M.; Tudos, A. J.; et al. Optical Biosensors. *Essays Biochem.* **2016**, *60* (1), 91–100. https://doi.org/10.1042/EBC20150010.

(115) Patel, P. N.; Mishra, V.; Mandloi, A. S. Optical Biosensors : Fundamentals \& Trends. *J. Eng. Res. Stud.* **2010**, *I* (I), 15–34.
(116) Carrara, S. *Nano-Bio-Sensing*; 2011. https://doi.org/10.1007/978-1-4419-6169-3.
(117) Geddes, C. D. *Metal-Enhanced Fluorescence*; 2010. https://doi.org/10.1002/9780470642795.
(118) Kim, D.; Daniel, W. L.; Mirkin, C. A. Microarray-Based Multiplexed Scanometric Immunoassay for Protein Cancer Markers Using Gold Nanoparticle Probes. *Anal. Chem.* **2009**. https://doi.org/10.1021/ac9018389.
(119) Fu, C. C.; Ossato, G.; Long, M.; Digman, M. A.; Gopinathan, A.; Lee, L. P.; Gratton, E.; Khine, M. Bimetallic Nanopetals for Thousand-Fold Fluorescence Enhancements. *Appl. Phys. Lett.* **2010**, *97* (20), 1–4. https://doi.org/10.1063/1.3495773.
(120) White, I. M.; Yazdi, S. H.; Yu, W. W. Optofluidic SERS: Synergizing Photonics and Microfluidics for Chemical and Biological Analysis. *Microfluidics and Nanofluidics*. 2012. https://doi.org/10.1007/s10404-012-0962-2.
(121) Dutta Choudhury, S.; Badugu, R.; Ray, K.; Lakowicz, J. R. Silver-Gold Nanocomposite Substrates for Metal-Enhanced Fluorescence: Ensemble and Single-Molecule Spectroscopic Studies. *J. Phys. Chem. C* **2012**. https://doi.org/10.1021/jp212242x.
(122) Lakowicz, J. R. Radiative Decay Engineering: Biophysical and Biomedical Applications. *Anal. Biochem.* **2001**, *298* (1), 1–24. https://doi.org/10.1006/abio.2001.5377.
(123) Geddes, C. D.; Lakowicz, J. R. Editorial: Metal-Enhanced Fluorescence. *J. Fluoresc.* **2002**, *12* (2), 121–129. https://doi.org/10.1023/A:1016875709579.
(124) Lakowicz, J. R. Radiative Decay Engineering 5: Metal-Enhanced Fluorescence and Plasmon Emission. *Anal. Biochem.* **2005**, *337* (2), 171–194. https://doi.org/10.1016/j.ab.2004.11.026.
(125) Lakowicz, J. R.; Masters, B. R. Principles of Fluorescence Spectroscopy, Third Edition. *J. Biomed. Opt.* **2008**. https://doi.org/10.1117/1.2904580.
(126) Geddes, C. D.; Lakowicz, J. R. Metal-Enhanced Fluorescence. In *Journal of Fluorescence*; 2002. https://doi.org/10.1023/A:1016875709579.
(127) Albani, J. R. Fluorescence Quenching. In *Structure and Dynamics of Macromolecules: Absorption and Fluorescence Studies*; 2004. https://doi.org/10.1016/B978-044451449-3/50004-6.
(128) Dulkeith, E.; Morteani, A. C.; Niedereichholz, T.; Klar, T. A.; Feldmann, J.; Levi, S. A.; van Veggel, F. C. J. M.; Reinhoudt, D. N.; Möller, M.; Gittins, D. I. Fluorescence Quenching of Dye Molecules near Gold Nanoparticles: Radiative and Nonradiative Effects. *Phys. Rev. Lett.* **2002**. https://doi.org/10.1103/PhysRevLett.89.203002.
(129) Lakowicz, J. R. Quenching of Fluorescence. In *Principles of Fluorescence Spectroscopy*; 1983. https://doi.org/10.1007/978-1-4615-7658-7_9.
(130) Gryczynski, I.; Malicka, J.; Gryczynski, Z.; Lakowicz, J. R. Radiative Decay Engineering 4. Experimental Studies of Surface Plasmon-Coupled Directional Emission. *Anal. Biochem.* **2004**, *324* (2), 170–182. https://doi.org/10.1016/j.ab.2003.09.036.
(131) Gagnon, Z.; Senapati, S.; Gordon, J.; Chang, H. C. Dielectrophoretic Detection and Quantification of Hybridized DNA Molecules on Nano-Genetic Particles. *Electrophoresis* **2008**. https://doi.org/10.1002/elps.200800528.
(132) Martin, R. S.; Gawron, A. J.; Lunte, S. M.; Henry, C. S. Dual-Electrode Electrochemical Detection for Poly(Dimethylsiloxane)-Fabricated Capillary Electrophoresis Microchips. *Anal. Chem.* **2000**. https://doi.org/10.1021/ac000160t.

(133) Green, N. G.; Morgan, H. Dielectrophoresis of Submicrometer Latex Spheres. 1. Experimental Results. *J. Phys. Chem. B* **2002**. https://doi.org/10.1021/jp9829849.
(134) Castellanos, A.; Ramos, A.; González, A.; Green, N. G.; Morgan, H. Electrohydrodynamics and Dielectrophoresis in Microsystems: Scaling Laws. *J. Phys. D. Appl. Phys.* **2003**. https://doi.org/10.1088/0022-3727/36/20/023.
(135) Tuukkanen, S.; Kuzyk, A.; Jussi Toppari, J.; Häkkinen, H.; Hytönen, V. P.; Niskanen, E.; Rinkiö, M.; Törmä, P. Trapping of 27 Bp-8 Kbp DNA and Immobilization of Thiol-Modified DNA Using Dielectrophoresis. *Nanotechnology* **2007**. https://doi.org/10.1088/0957-4484/18/29/295204.
(136) Nakano, A.; Ros, A. Protein Dielectrophoresis: Advances, Challenges, and Applications. *Electrophoresis*. 2013. https://doi.org/10.1002/elps.201200482.
(137) Zhou, R.; Wang, P.; Chang, H. C. Bacteria Capture, Concentration and Detection by Alternating Current Dielectrophoresis and Self-Assembly of Dispersed Single-Wall Carbon Nanotubes. *Electrophoresis* **2006**. https://doi.org/10.1002/elps.200500329.
(138) Benkert, A.; Scheller, F.; Schössler, W.; Hentschel, C.; Micheel, B.; Behrsing, O.; Scharte, G.; Stöcklein, W.; Warsinke, A. Development of a Creatinine ELISA and an Amperometric Antibody-Based Creatinine Sensor with a Detection Limit in the Nanomolar Range. *Anal. Chem.* **2000**. https://doi.org/10.1021/ac9909047.
(139) Epstein, J. R.; Walt, D. R. Fluorescence-Based Fibre Optic Arrays: A Universal Platform for Sensing. *Chem. Soc. Rev.* **2003**. https://doi.org/10.1039/b300617d.
(140) Patterson, G. H.; Knobel, S. M.; Sharif, W. D.; Kain, S. R.; Piston, D. W. Use of the Green Fluorescent Protein and Its Mutants in Quantitative Fluorescence Microscopy. *Biophys. J.* **1997**. https://doi.org/10.1016/S0006-3495(97)78307-3.
(141) Mendes, P. M.; Jacke, S.; Critchley, K.; Plaza, J.; Chen, Y.; Nikitin, K.; Palmer, R. E.; Preece, J. A.; Evans, S. D.; Fitzmaurice, D. Gold Nanoparticle Patterning of Silicon Wafers Using Chemical E-Beam Lithography. *Langmuir* **2004**. https://doi.org/10.1021/la049803g.
(142) Barik, A.; Otto, L. M.; Yoo, D.; Jose, J.; Johnson, T. W.; Oh, S. H. Dielectrophoresis-Enhanced Plasmonic Sensing with Gold Nanohole Arrays. *Nano Lett.* **2014**, *14* (4), 2006–2012. https://doi.org/10.1021/nl500149h.
(143) Nawarathna, D.; Turan, T.; Wickramasinghe, H. K. Selective Probing of MRNA Expression Levels within a Living Cell. *Appl. Phys. Lett.* **2009**. https://doi.org/10.1063/1.3213343.
(144) Wolcott, M. J. Advances in Nucleic Acid-Based Detection Methods. *Clin. Microbiol. Rev.* **1992**. https://doi.org/10.1128/CMR.5.4.370.
(145) Cheng, I. F.; Senapati, S.; Cheng, X.; Basuray, S.; Chang, H. C.; Chang, H. C. A Rapid Field-Use Assay for Mismatch Number and Location of Hybridized DNAs. *Lab Chip* **2010**. https://doi.org/10.1039/b925854j.
(146) Zheng, L.; Brody, J. P.; Burke, P. J. Electronic Manipulation of DNA, Proteins, and Nanoparticles for Potential Circuit Assembly. In *Biosensors and Bioelectronics*; 2004. https://doi.org/10.1016/j.bios.2004.03.029.
(147) Clarke, R. W.; White, S. S.; Zhou, D.; Ying, L.; Klenerman, D. Trapping of Proteins under Physiological Conditions in a Nanopipette. *Angew. Chemie - Int. Ed.* **2005**. https://doi.org/10.1002/anie.200500196.

(148) Cuervo, A.; Dans, P. D.; Carrascosa, J. L.; Orozco, M.; Gomila, G.; Fumagalli, L. Direct Measurement of the Dielectric Polarization Properties of DNA. *Proc. Natl. Acad. Sci.* **2014**. https://doi.org/10.1073/pnas.1405702111.
(149) Lu, G.; Li, W.; Zhang, T.; Yue, S.; Liu, J.; Hou, L.; Li, Z.; Gong, Q. Plasmonic-Enhanced Molecular Fluorescence within Isolated Bowtie Nano-Apertures. *ACS Nano* **2012**, *6* (2), 1438–1448. https://doi.org/10.1021/nn2042412.
(150) Mulvihill, M. J.; Ling, X. Y.; Henzie, J.; Yang, P. Anisotropic Etching of Silver Nanoparticles for Plasmonic Structures Capable of Single-Particle SERS. *J. Am. Chem. Soc.* **2010**. https://doi.org/10.1021/ja906954f.
(151) Maier, S. A.; Atwater, H. A. Plasmonics: Localization and Guiding of Electromagnetic Energy in Metal/Dielectric Structures. *J. Appl. Phys.* **2005**, *98* (1). https://doi.org/10.1063/1.1951057.
(152) Li, H.; Bashir, R. Dielectrophoretic Separation and Manipulation of Live and Heat-Treated Cells of Listeria on Microfabricated Devices with Interdigitated Electrodes. *Sensors Actuators, B Chem.* **2002**. https://doi.org/10.1016/S0925-4005(02)00172-7.
(153) Nawarathna, D.; Norouzi, N.; McLane, J.; Sharma, H.; Sharac, N.; Grant, T.; Chen, A.; Strayer, S.; Ragan, R.; Khine, M. Shrink-Induced Sorting Using Integrated Nanoscale Magnetic Traps. *Appl. Phys. Lett.* **2013**. https://doi.org/10.1063/1.4790191.
(154) Iandolo, B.; Antosiewicz, T. J.; Hellman, A.; Zorić, I. On the Mechanism for Nanoplasmonic Enhancement of Photon to Electron Conversion in Nanoparticle Sensitized Hematite Films. *Phys. Chem. Chem. Phys.* **2013**. https://doi.org/10.1039/c3cp44483j.
(155) Nakano, A.; Luo, J.; Ros, A. Temporal and Spatial Temperature Measurement in Insulator-Based Dielectrophoretic Devices. *Anal. Chem.* **2014**. https://doi.org/10.1021/ac501083h.
(156) Chaurey, V.; Rohani, A.; Su, Y. H.; Liao, K. T.; Chou, C. F.; Swami, N. S. Scaling down Constriction-Based (Electrodeless) Dielectrophoresis Devices for Trapping Nanoscale Bioparticles in Physiological Media of High-Conductivity. *Electrophoresis* **2013**. https://doi.org/10.1002/elps.201200456.
(157) Lu, Y.; Liu, T.; Lamanda, A. C.; Sin, M. L. Y.; Gau, V.; Liao, J. C.; Wong, P. K. AC Electrokinetics of Physiological Fluids for Biomedical Applications. *Journal of Laboratory Automation*. 2015. https://doi.org/10.1177/2211068214560904.
(158) Brismar, H.; Trepte, O.; Ulfhake, B. Spectra and Fluorescence Lifetimes of Lissamine Rhodamine, Tetramethylrhodamine Isothiocyanate, Texas Red, and Cyanine 3.18 Fluorophores: Influences of Some Environmental Factors Recorded with a Confocal Laser Scanning Microscope. *J. Histochem. Cytochem.* **1995**. https://doi.org/10.1177/43.7.7608524.
(159) Poruk, K. E.; Firpo, M. a; Adler, D. G.; Mulvihill, S. J. Screening for Pancreatic Cancer: Why, How, and Who? *Ann Surg* **2013**, *257* (1), 17–26. https://doi.org/10.1097/SLA.0b013e31825ffbfb.Screening.
(160) Ji, D. L.; Li, C. L.; Cui, Y. F. Early Diagnosis of Pancreatic Cancer. *World Chinese J. Dig.* **2014**, *22* (17), 2406–2413. https://doi.org/10.11569/wcjd.v22.i17.2406.
(161) Goonetilleke, K. S.; Siriwardena, A. K. Systematic Review of Carbohydrate Antigen (CA 19-9) as a Biochemical Marker in the Diagnosis of Pancreatic Cancer. *European Journal of Surgical Oncology*. 2007. https://doi.org/10.1016/j.ejso.2006.10.004.

(162) K.M., G.; K.A., L.; G.C., B.; P.D., G.; M.A., H. Epigenetic Mechanisms and the Mismatch Concept of the Developmental Origins of Health and Disease. *Pediatr. Res.* **2007**. https://doi.org/10.1203/pdr.0b013e318045bedb LK - http://sfx.library.uu.nl/utrecht?sid=EMBASE&issn=00313998&id=doi:10.1203%2Fpdr.0b013e318045bedb&atitle=Epigenetic+mechanisms+and+the+mismatch+concept+of+the+developmental+origins+of+health+and+disease&stitle=Pediatr.+Res.&title=Pediatric+Research&volume=61&issue=5+PART+2+SUPPL.&spage=&epage=&aulast=Godfrey&aufirst=Keith+M.&auinit=K.M.&aufull=Godfrey+K.M.&coden=PEREB&isbn=&pages=-&date=2007&auinit1=K&auinitm=M.

(163) Hanson, M.; Godfrey, K. M.; Lillycrop, K. A.; Burdge, G. C.; Gluckman, P. D. Developmental Plasticity and Developmental Origins of Non-Communicable Disease: Theoretical Considerations and Epigenetic Mechanisms. *Progress in Biophysics and Molecular Biology*. 2011. https://doi.org/10.1016/j.pbiomolbio.2010.12.008.

(164) Reinhard, S. The Thrifty Epigenotype: An Acquired and Heritable Predisposition for Obesity and Diabetes? *BioEssays* **2008**.

(165) T., M.; J.M., C. DNA Methylation Biomarkers: Cancer and Beyond. *Genes (Basel).* **2014**. https://doi.org/10.3390/genes5030821.

(166) Tang, W. Y.; Ho, S. M. Epigenetic Reprogramming and Imprinting in Origins of Disease. *Reviews in Endocrine and Metabolic Disorders*. 2007. https://doi.org/10.1007/s11154-007-9042-4.

(167) Mercer, T. R.; Mattick, J. S. Structure and Function of Long Noncoding RNAs in Epigenetic Regulation. *Nature Structural and Molecular Biology*. 2013. https://doi.org/10.1038/nsmb.2480.

(168) Arroyo, J. D.; Chevillet, J. R.; Kroh, E. M.; Ruf, I. K.; Pritchard, C. C.; Gibson, D. F.; Mitchell, P. S.; Bennett, C. F.; Pogosova-Agadjanyan, E. L.; Stirewalt, D. L.; et al. Argonaute2 Complexes Carry a Population of Circulating MicroRNAs Independent of Vesicles in Human Plasma. *Proc. Natl. Acad. Sci.* **2011**, *108* (12), 5003–5008. https://doi.org/10.1073/pnas.1019055108.

(169) E.B., P.; D.M., C.; L.M., B.; S.M., P.; V.G., C.; Hawley, J. A. Circulating Microrna Responses between "high" and "Low" Responders to a 16-Wk Diet and Exercise Weight Loss Intervention. *PLoS One* **2016**.

(170) Toyama, K.; Kiyosawa, N.; Watanabe, K.; Ishizuka, H. Identification of Circulating MiRNAs Differentially Regulated by Opioid Treatment. *Int. J. Mol. Sci.* **2017**. https://doi.org/10.3390/ijms18091991.

(171) Moldovan, L.; Batte, K. E.; Trgovcich, J.; Wisler, J.; Marsh, C. B.; Piper, M. Methodological Challenges in Utilizing MiRNAs as Circulating Biomarkers. *J. Cell. Mol. Med.* **2014**, *18* (3), 371–390. https://doi.org/10.1111/jcmm.12236.

(172) Sohel, M. H. Extracellular/Circulating MicroRNAs: Release Mechanisms, Functions and Challenges. *Achiev. Life Sci.* **2016**, *10* (2), 175–186. https://doi.org/10.1016/j.als.2016.11.007.

(173) S.L., M.; B.P., T.; A.L., P.; O., G.; Y., M.; S.F., N.; Mumford, S. L.; Towler, B. P.; Pashler, A. L.; Gilleard, O.; et al. Circulating MicroRNA Biomarkers in Melanoma: Tools and Challenges in Personalised Medicine. *Biomolecules* **2018**. https://doi.org/10.3390/biom8020021.

(174) El-Khoury, V.; Pierson, S.; Kaoma, T.; Bernardin, F.; Berchem, G. Assessing Cellular and Circulating MiRNA Recovery: The Impact of the RNA Isolation Method and the Quantity of Input Material. *Sci. Rep.* **2016**, *6* (December 2015), 1–14. https://doi.org/10.1038/srep19529.
(175) Tiberio, P.; Callari, M.; Angeloni, V.; Daidone, M. G.; Appierto, V. Challenges in Using Circulating MiRNAs as Cancer Biomarkers. *Biomed Res. Int.* **2015**, *2015*. https://doi.org/10.1155/2015/731479.
(176) Tuck, M. K.; Chan, D. W.; Chia, D.; Godwin, A. K.; Grizzle, W. E.; Krueger, K. E.; Rom, W.; Sanda, M.; Sorbara, L.; Stass, S.; et al. Standard Operating Procedures for Serum and Plasma Collection: Early Detection Research Network Consensus Statement Standard Operating Procedure Integration Working Group. *J. Proteome Res.* **2009**. https://doi.org/10.1021/pr800545q.
(177) Teunissen, C. E.; Petzold, A.; Bennett, J. L.; Berven, F. S.; Brundin, L.; Comabella, M.; Franciotta, D.; Frederiksen, J. L.; Fleming, J. O.; Furlan, R.; et al. A Consensus Protocol for the Standardization of Cerebrospinal Fluid Collection and Biobanking. *Neurology*. 2009. https://doi.org/10.1212/WNL.0b013e3181c47cc2.
(178) Ladik, L. S. G. B. J. The Effect of Electric Field on the Electronic Structure of DNA. I. Calculation of the Polarizability and of the Permanent Dipole Moment for the Nucleotide Bases and Base Pairs. *Quantum Chem.* **1969**, *3* (5), 621–634.
(179) Morgan, H.; Hughes, M. P.; Green, N. G. Separation of Submicron Bioparticles by Dielectrophoresis. *Biophys. J.* **1999**. https://doi.org/10.1016/S0006-3495(99)76908-0.
(180) Iqbal, A.; Arslan, S.; Okumus, B.; Wilson, T. J.; Giraud, G.; Norman, D. G.; Ha, T.; Lilley, D. M. J. Orientation Dependence in Fluorescent Energy Transfer between Cy3 and Cy5 Terminally Attached to Double-Stranded Nucleic Acids. *Proc. Natl. Acad. Sci.* **2008**. https://doi.org/10.1073/pnas.0801707105.
(181) Jain, P. K.; El-Sayed, M. A. Plasmonic Coupling in Noble Metal Nanostructures. *Chem. Phys. Lett.* **2010**. https://doi.org/10.1016/j.cplett.2010.01.062.
(182) Pethig, R. Dielectrophoresis: Using Inhomogeneous AC Electrical Fields to Separate and Manipulate Cells. *Crit. Rev. Biotechnol.* **1996**. https://doi.org/10.3109/07388559609147425.
(183) Pethig, R.; Huang, Y.; Wang, X. B.; Burt, J. P. H. Positive and Negative Dielectrophoretic Collection of Coiloidal Particles Using Interdigitated Castellated Microelectrodes. *J. Phys. D. Appl. Phys.* **1992**. https://doi.org/10.1088/0022-3727/25/5/022.
(184) Sharma, H.; Wood, J. B.; Lin, S.; Corn, R. M.; Khine, M. Shrink-Induced Silica Multiscale Structures for Enhanced Fluorescence from DNA Microarrays. *Langmuir* **2014**. https://doi.org/10.1021/la501123b.
(185) Kroh, E. M.; Parkin, R. K.; Mitchell, P. S.; Tewari, M. Analysis of Circulating MicroRNA Biomarkers in Plasma and Serum Using Quantitative Reverse Transcription-PCR (QRT-PCR). *Methods* **2010**. https://doi.org/10.1016/j.ymeth.2010.01.032.
(186) Jackson, J. . Classical Electromagnetics. **1999**, 330–335.
(187) Madou, M.; Wang, C. Photolithography. In *Encyclopedia of Nanotechnology*; 2015. https://doi.org/10.1007/978-94-007-6178-0_342-2.
(188) Mitra, S.; Chakraborty, S.; Martinez-Duarte, R.; Madou, M. SU-8 Photolithography and Its Impact on Microfluidics. In *Microfluidics and Nanofluidics Handbook*; 2012. https://doi.org/10.1201/b11188-11.

(189) Duhr, S.; Braun, D. Optothermal Molecule Trapping by Opposing Fluid Flow with Thermophoretic Drift. *Phys. Rev. Lett.* **2006**. https://doi.org/10.1103/PhysRevLett.97.038103.
(190) Wong, I. Y.; Melosh, N. A. An Electrostatic Model for DNA Surface Hybridization. *Biophys. J.* **2010**. https://doi.org/10.1016/j.bpj.2010.03.017.
(191) Tymoczko, J.; Schuhmann, W.; Gebala, M. Electrical Potential-Assisted DNA Hybridization. How to Mitigate Electrostatics for Surface DNA Hybridization. *ACS Applied Materials and Interfaces*. 2014. https://doi.org/10.1021/am5027902.
(192) Capaldo, P.; Alfarano, S. R.; Ianeselli, L.; Zilio, S. D.; Bosco, A.; Parisse, P.; Casalis, L. Circulating Disease Biomarker Detection in Complex Matrices: Real-Time, in Situ Measurements of DNA/MiRNA Hybridization via Electrochemical Impedance Spectroscopy. *ACS Sensors* **2016**. https://doi.org/10.1021/acssensors.6b00262.
(193) Reichl, M.; Herzog, M.; Greiss, F.; Wolff, M.; Braun, D. Understanding the Similarity in Thermophoresis between Single- and Double-Stranded DNA or RNA. *Phys. Rev. E - Stat. Nonlinear, Soft Matter Phys.* **2015**. https://doi.org/10.1103/PhysRevE.91.062709.
(194) Acuna, G. P.; Bucher, M.; Stein, I. H.; Steinhauer, C.; Kuzyk, A.; Holzmeister, P.; Schreiber, R.; Moroz, A.; Stefani, F. D.; Liedl, T.; et al. Distance Dependence of Single-Fluorophore Quenching by Gold Nanoparticles Studied on DNA Origami. *ACS Nano* **2012**. https://doi.org/10.1021/nn2050483.
(195) Schefe, J. H.; Lehmann, K. E.; Buschmann, I. R.; Unger, T.; Funke-Kaiser, H. Quantitative Real-Time RT-PCR Data Analysis: Current Concepts and the Novel "Gene Expression's C T Difference" Formula. *Journal of Molecular Medicine*. 2006. https://doi.org/10.1007/s00109-006-0097-6.
(196) Johnson-Buck, A.; Su, X.; Giraldez, M. D.; Zhao, M.; Tewari, M.; Walter, N. G. Kinetic Fingerprinting to Identify and Count Single Nucleic Acids. *Nat. Biotechnol.* **2015**. https://doi.org/10.1038/nbt.3246.